Electronic Thesis and Dissertation Repository

6-18-2020 11:00 AM

Kinetic Analysis of Dynamic PET for Molecular, Functional and Physiological Characterization of Diseases

Fiona Li, *The University of Western Ontario*

Follow this and additional works at: https://ir.lib.uwo.ca/etd

Part of the Medical Biophysics Commons

Abstract

PET with targeted probes may better elucidate the molecular and functional basis of diseases. The widely used standardized uptake value from static imaging, however, cannot quantify the probe uptake processes like perfusion, permeability, binding to and disassociation (k_4) from target. The overarching thesis goal is to develop a model to enable kinetic analysis of dynamic imaging to separate these processes.

As perfusion delivery is not modelled in the current standard two tissue compartment (S2TC) model, I developed a flow modified two tissue compartment (F2TC) model that incorporates the blood flow effect. The model's performances were investigated with simulation. It was applied to derive kinetic parameters of [^{18}F]FAZA binding to highly hypoxic pancreatic cancer. As a validation, the distribution volume (DV) of [^{18}F]FAZA determined with the F2TC and S2TC model were compared with graphical analysis (GA). Kinetic analysis requires arterial concentration of the native probe to model the observed tissue uptake over time, therefore, a method was developed to correct for the metabolite contamination of arterial plasma.

Based on fractional Euclidean distance of estimated and simulated parameters, F2TC model performed better than S2TC model, particularly with longer mean transit time due to the neglect of perfusion effect in the latter model. Also, dynamic acquisition longer than 45 minutes did not improve the accuracy of estimated F2TC model parameters. In the pancreatic cancer study: (a) GA showed that [^{18}F]FAZA was reversibly bound to hypoxic cells; (b) DV estimated by the F2TC and S2TC model was not and was significantly different from GA respectively; (c) k_4 and DV estimated by F2TC model could distinguish normal and cancerous tissue with 95% sensitivity. TLC-autoradiography identified metabolites in 2µL of arterial plasma with radioactivity as low as 17Bq. This high sensitivity and the ability to measure multiple (8-12) samples simultaneously could allow metabolite correction of arterial plasma to be performed in individual studies.

Finally, the reversible binding of [^{18}F]FAZA in hypoxic pancreatic tumor cells could be due to efflux of reduced products by the multidrug resistance protein. Therefore, kinetic

analysis of dynamic [^{18}F]FAZA PET could monitor both hypoxia and drug resistance for individualized treatment.

Keywords

Dynamic PET, kinetic modelling, flow modified two tissue compartment model, hypoxia, [^{18}F]FAZA, [^{18}F]FEPPA, radio-metabolite correction, thin layer chromatography, autoradiography, and pancreatic ductal adenocarcinoma

Summary for Lay Audience

PET is an imaging technique that uses targeted molecules (tracers) to monitor disease processes in the body. Currently, static "snapshot" imaging is used to image the tracer uptake at a single time following injection. Static imaging cannot differentiate the different dynamic processes involved in tracer uptake over time. Dynamic imaging acquired at multiple times post injection are required for the analysis of these dynamic processes, elucidation of which can improve our mechanistic understanding of disease. The overarching goal of my PhD research is to develop a mathematical model for the analysis of dynamic images. This analysis, also called kinetic analysis, requires measurement of the fraction of native (unmodified) tracer in blood plasma, therefore, I also developed a technique to measure such fraction in blood plasma.

The current mathematical model, standard two tissue compartment model (S2TCM), neglects the delivery of tracer by blood flow. I developed a flow modified two tissue compartment model (F2TCM) to explicitly take into account of this delivery effect. Computer simulation showed the F2TCM is better than S2TCM in more accurately measuring the processes involved in the uptake of the targeted tracer, therefore may be better in characterizing disease mechanisms. Furthermore, this improved analysis was achieved with 45 min of dynamic image acquisition.

The developed F2TCM was applied to pancreatic cancer to investigate the uptake of [^{18}F]FAZA, a targeted tracer that binds to tumor cells deprived of oxygen (hypoxic), making them resistant to treatment. It was found that the tracer is not trapped in hypoxic cells as commonly believed and it could be pumped out of hypoxic tumor cells via the multidrug resistance protein on cell surface. Furthermore two parameters estimated with the F2TCM can identify pancreatic cancer with 95% sensitivity.

The developed technique can measured the fraction of native tracer in blood plasma using very small volume of very low radioactivity. Metabolite contamination of blood plasma has been plaguing the accuracy of kinetic analysis and calls for measurement of this

contamination in individual patients. The high sensitivity and convenience of my technique opens up the possibility of measuring the plasma metabolite fraction for individual patients.

Co-Authorship Statement

The thesis consist of manuscripts will be submitted to peer-reviewed journals.

Chapter two was adapted from simulation manuscript titled: "Estimation of kinetic parameters for dynamic PET imaging: A simulation study" which was submitted to *Physics in Medicine and Biology* by F Li, D-M Yang and T-Y Lee. The study was designed by T-Y Lee and myself with contribution from D-M Yang. I was responsible for implementing the simulation design on MATLAB, analyzing and interpreting the data, and I wrote the whole manuscript with assistance from T-Y Lee. All the authors reviewed the manuscript.

Chapter three was adapted from manuscript titled: "Pharmacokinetic analysis of dynamic ^{18}F-FAZA PET imaging in pancreatic cancer patient" which was submitted to *European Journal of Nuclear Medicine and Molecular Imaging* by F Li, E Taylor, I Yeung, D Jaffray, DW Hedley and T-Y Lee. The study was designed by T-Y Lee and myself. The images were provided by I Yeung, D Jaffray and DW Hedley while the processed images and curves were obtained from E Taylor. I performed detailed kinetic analysis on the provided curves as well data processing, analysis and data interpretation. In addition, I also wrote the manuscript with assistance from T-Y Lee. All the authors reviewed the manuscript.

Chapter four was adapted from manuscript titled: "Radio-metabolite analysis of PET tracers in plasma for dynamic PET imaging: TLC and autoradiography" which was submitted to *European Journal of Nuclear Medicine and Molecular Imaging Research* by F Li, J Hicks, L Desjardin, L Morrison, J Hadway and T-Y Lee. The study was designed by T-Y Lee and myself with contribution from J Hicks. L Desjardin, L Morrison and J Hadway assisted with blood draws and animal care. I was responsible for carrying out the experiment, processed, analyzed and interpreted the data. The manuscript was written by me under the supervision of T-Y Lee. All the authors reviewed the manuscript.

Acknowledgments

First and foremost, I would like give my heart felt appreciation to my supervisors, Drs. Ting-Yim Lee and James Koropatnick. I am incredibly honored to work with two scientists who worked tirelessly towards cancer research. Ting's relentless guidance, enthusiasm and his insightful debate on research topics contributed to my drive towards research throughout my PhD. I am confident that the lesson he provided in problem solving, the optimistic thinking and the leadership qualities will help me in my future endeavors. Lastly, thank you for believing in me and putting up with my shenanigans. Thank you James for bridging my missing knowledge in cancer biology that is required for completing my thesis and extending your helping hands whenever needed. I also want to thank my advisor, Dr. Paula Foster, for the scientific advice and support.

The animal experiments would not be possible without the help of all the animal technicians. To Lise Desjardins, thank you for helping me with my experiments, no matter how late it was. I will never forget the friendship and the humors during stressful time and for putting up with my frustrations. To Jennifer Hadway who always made sure my experiment was going well, making sure my protocol is up to date so I can graduate on time. Laura Morrison, thank you for filling in when either Jennifer, Lise or I cannot make it for my experiment. Thank you Lynn Keenliside for making last minute adjustment to my instrumentations.

To all the present and past Lee lab members, I owe great appreciation for making my PhD experience a fun and enjoyable one. My study would not be possible without the help of Dr. Xiaogang Chen. His expertise in programming and his contribution to software development played a major role in my thesis completion. To Dr. Feng Su who assisted me with image registrations. To Dr. Errol Stewart who provided valuable and insightful debates, and for helping me with transitioning into new school and new environment at the start of my graduate school, and his continual guidance even after leaving for Calgary.

Thank you to my collaborators, Dr Ivan Yeung for providing me with the images required for completing chapter 3 of the thesis. To Dr. Edward Taylor, Brandon Driscoll and Tina

Shek for assisting me with remote access, transferring images and guiding me with image analysis.

My sincere thanks to Anne Leaist for holding the lab together with our late afternoon nourishments, maintaining inviting environment in the lab with the laughter and enlightening conversations, and the administrative assistance, particularly the conference expenses and departmental issues.

Lastly, I would like to express my heartfelt thank you my family for the constant support and unconditional love essential for my studies.

Table of Contents

List of Tables

List of Figures

Chapter 1

1 Introduction

Positron Emission Tomography (PET) is a non-invasive nuclear imaging technique for monitoring cellular and metabolic function of tissues or organs in vivo. The principle of PET is that targeted substrates or ligands specific for particular enzymes or receptors respectively, called tracers, are labelled with radioactive element like ^{18}F, ^{11}C and ^{13}N. The uptake of the tracer in the targeted tissue as imaged by PET following injection provide pharmacokinetic information that can guide drug development and/or shed light on the pathogenic mechanisms of diseases.

1.1 The working principle of PET imaging

The radioactive element in the tracer decays by emitting positrons. The positrons generally travels for a short distance before it interacts or collide with electrons from neighboring atoms during annihilation process. The interaction produces two 511 keV photons at 180º angle which is captured as coincidence photons by two opposite detectors encircling the patient. The detectors are usually scintillation detectors that converts high energy photons to low energy visible photons which are amplified by photon multiplier tubes. As the emitted photons travel through the patient's body, the photons gets attenuated due to scattering and absorption, which needs to be corrected and it depends on the linear attenuation correction and the path length. Due to coincidence detection in PET, the attenuation path length is the same along the line of response (LOR) while in single photon emission computerized tomography (SPECT) the path length depends on the location of the emission. Therefore, correcting for attenuation is more difficult in SPECT[1]. This allows for accurate measurement of tracer activity concentration in the subject with PET.

Tracer concentrations in PET are detected as counts. The major advantage of PET is the ability to convert the detected counts into activity concentration necessary for quantification of metabolic rates. This requires calibration of the system which is done by

scanning a 20 cm cylinder phantom with known activity in Bq/mL. The counts in the center of the phantom can be measured and since the activity in the center of the phantom is known, the conversion factor can be estimated[2].

PET signals are generated by coincidence events which is limited by counting statistics. To improve the signal to noise (SNR) of the images in the initial phase of PET acquisition, the counts are averaged over certain time interval of 5-10s called frame averaging. However, due to the fast wash in and washout of tracer immediately after the tracer injection, dynamic images at short time bins are required to capture rapid changes in tracer concentration in initial phase, particularly when obtaining the image derived arterial input function curve[3]. This is prone to image noise and low counts. In order to achieve higher counting statistics, the sensitivity of the system needs to be improved. The sensitivity is measured in terms of noise equivalent count rate (NECR)[4], which is a measure of true coincidence counts accounting for unwanted random and scatter coincidence. It has a direct square root relationship with SNR.

The most prevalent example of a PET tracer is [^{18}F]fluorodeoxyglucose ([^{18}F]FDG), a glucose analog that enters the cell via membrane glucose transporters and is phosphorylated by the glycolysis enzyme hexokinase into ^{18}F-fluorodeoxyglucose-6-phosphate ([^{18}F]FDG-6-P). Because [^{18}F]FDG-6-P is hydrophilic and with the absence of phosphatase to dephosphorylate back to [^{18}F]FDG, it becomes trapped in the cell. Therefore, accumulation of [^{18}F]FDG-6-P in tissue is a surrogate marker of its metabolic (glycolytic) activity. In cancer, because of the Warburg effect[5], anaerobic metabolism is enhanced, this would lead to upregulated hexokinase activity and more accumulation of [^{18}F]FDG-6-P in-situ. PET [^{18}F]FDG imaging can access the metabolic changes in cancer following treatment as well as in detecting and staging cancers[6,7]. Uptake of [^{18}F]FDG is highly correlated with tumor malignancy in lung, breast, colorectal cancer and other types of cancer[7].

1.2 Quantitative analysis of PET

Besides being sensitive, PET is a very a specific imaging modality because of the targeted tracers developed. Furthermore, it is highly quantitative, meaning that PET image

intensities can be calibrated relatively easily to give concentration of the targeted tracer both in tissue and arterial blood. As such, PET imaging data, unlike those from other imaging modalities, can be used in kinetics modelling to derive information concerning the mechanisms of diseases. By kinetics modeling we mean to model transport processes, e.g. blood flow, that govern the distribution of the injected targeted tracer to body organs and tissues and molecular (biochemical) processes that either convert the native targeted tracer into its products, e.g. the phosphorylation of [18F]FDG into [18F]FDG-6-P and possibly dephosphorylation or bind the 'free' targeted tracer either reversibly or irreversibly to its receptor. Through kinetics modeling, quantitative measures of these different processes, e.g. blood flow and volume, enzyme activity, receptor concentration and binding potential, useful on elucidating the mechanisms of diseases and their response to treatment can be obtained in-vivo without resorting to tissue sampling and subsequent histopathology or immunohistochemistry. Despite these potential advantages, kinetics modeling in quantitative PET analysis is not commonly used either in research or clinical setting possibly due to its complexity compared to the more frequently used semi-quantitative standardized uptake value (SUV) analysis. In the following subsections, the salient differences between SUV and kinetics modeling will be discussed.

1.2.1 Standardized Uptake Value

Typically, PET images are quantified from a static (single) image acquired at some time after the tracer has been injected, after the tracer has reached a distribution equilibrium between blood and the target organ/tissue (not necessarily in all cases). It is quantified with a simple metric called standardized uptake value which is the uptake (concentration) of the tracer in the target tissue normalized by injected dose and body weight to account for distribution of tracer throughout the body[8]. It is widely used in monitoring cancer treatment responses[9] and differentiating malignant from benign tissue[10]. The major reason why this method is preferred over kinetic modeling is the short acquisition time and that measurement of arterial tracer concentration is not required which can be cumbersome clinically. However, the method has a number of problems including large variability[11–14]. SUV is usually taken at 60 minute or longer post tracer injection (p.i) when the tracer is assumed to have reached distribution equilibrium or when the target tissue uptake plateaus.

Figure 1-1: Dependency of SUV values on time acquisition
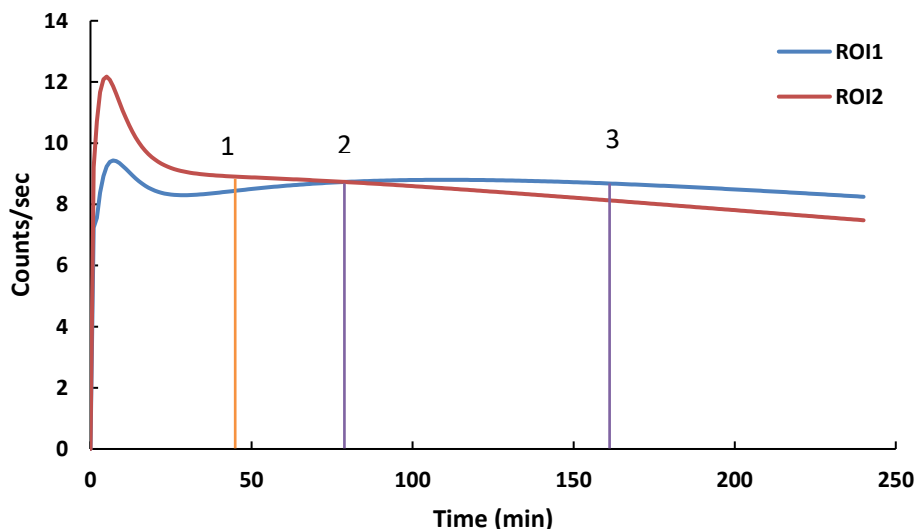
The graph demonstrates the dependency of SUVs on time acquisition. The two lines are simulated SUV with respective to time at two different regions of interest (ROI). ROI1 shows steady uptake of tracer followed by slow washout at later time points while ROI2 shows high influx of tracer in the beginning followed by continuous washout. At time point 1, the SUV for ROI2 will be higher than ROI1 and vice versa for time point 3 while the SUVs will be the same at time point 2. Furthermore, SUV will only provide information on the uptake of tracer but not the processes involved like the perfusion delivery.

It is impossible to determine the time when the tracer reaches equilibrium from a single time acquisition since it is dependent on tracer properties, for instance, slow vs. fast clearance, the disease of interest and the research question under investigation[15–17]. Hamberg et al. showed that for lung cancer patient imaged with ^{18}F-FDG, the tracer reached distribution equilibrium at 90 min but not at 60 min p.i.. This time difference introduced a 46% difference in the SUV which could lead to wrong diagnoses.[18]. Additionally, static images at different time points following tracer injection can lead to different interpretation of images. Figure 1.1 shows simulated tissue time activity curve (TAC) from two different regions of interest (ROIs). ROI2 showed high influx of the tracer followed by continuous washout while ROI1 showed steady accumulation of tracer beyond 30 minute p.i. (time point 1). The SUV for both ROIs coincides at 80 min p.i. (time point 2), before and after that time ROI2 SUV was higher than ROI1 and vice versa respectively.

Hence, SUV measured at a single time can lead to erroneous interpretation of the processes involved in the uptake of tracer.

SUV is usually calculated from ROI and there are several different calculated SUVs. SUV_{mean} is the average SUV within the region encircled by the iso-contour at a certain threshold percentage of the maximum pixel value within the region. It is dependent on the threshold chosen and is subject to inter-observer threshold variability. On the other hand, SUV_{max} is the maximum SUV value, representing highest metabolic pixel for ^{18}F-FDG. It is prone to noise variations due to absence of noise averaging when several pixels are averaged together[12,19,20]. SUV_{total} is the total uptake of the tracer in the ROI. These measures are usually used to classify patients into different response groups - complete response, partial response and stable disease. The different SUV measures can vary by as much as 90% in individual tumors and there was conflicting categorization of tumor response in 80% of the cases[9]. Furthermore, different institutes use different SUV measures making comparison of results based on SUV problematic without standardizing on the particular measure used[8].

Another problem is the use of a ^{18}F-FDG SUV threshold of 2.5[21,22] to classify tumor as benign or malignant. In cases of inflammation, the increased uptake of ^{18}F-FDG by inflammatory cells could be misinterpreted as tumor. On the other hand, some malignancies can have a slow uptake of the tracer, it will exhibit lower SUV values leading to a wrong diagnosis if imaging is not delayed beyond the norm. Blood glucose level also can affect SUV[11,12]. Hyperglycemic patients have oversaturated transmembrane glucose transporter (GLUT), preventing FDG uptake as both glucose and FDG competes for the same GLUT[13]. Therefore SUV values should not be taken at face value and the patient's underlining physiology should be taken into consideration while interpreting the value.

Finally, SUV is a 'snapshot' of tracer uptake at one time point. Tissue uptake of tracer is governed by three processes – perfusion, bidirectional permeability of blood-tissue barrier and binding and disassociation from the tissue target. SUV is the combination of all these processes. As these processes require more than one parameter to describe, a single image acquired at any time is not able to characterize these processes necessary for diagnosis and for guiding drug development[23].

1.2.2 Kinetic modelling

Tissue uptake of targeted tracer is complex and involves at least the following processes - perfusion, bidirectional permeability of blood-tissue barrier and binding and disassociation from the tissue target. Sequential PET images taken at multiple time points following tracer injection (i.e. dynamic PET) is required to generate data for deciphering these processes via kinetics modelling. There are several fundamental assumptions in kinetics modeling. First, a minute amount of the tracer compared to its endogenous compound needs to be injected in dynamic PET, such that it does not interfere with the native process(es) targeted by the tracer. Second, the targeted process(es) remains stable over the duration of dynamic PET when images are acquired. Third, the labelling of the tracer with radioactive element does not significantly alter its chemical and molecular properties[24]. A fundamental prerequisite for kinetics modeling, arising from the fact that the tracer is injected systematically, is an accurate measure of arterial tracer concentration over time – the arterial input function (AIF). One way to measure AIF is by manual blood sampling from a peripheral artery. For studies with long acquisition time, long blood sampling can have a small risk of complications like hand ischemia and it also exposes the staff to additional unnecessary radiation exposure while collecting blood[25]. A non-invasive approach is to measure AIF from left ventricle or arteries in the field of view (FOV) of the PET images – image derived AIF [26]. The imaging approach affords the opportunity to measure AIF that preserves fast wash-in and wash-out of tracer immediately after the tracer injection if fine temporal resolution in image acquisition is prescribed in this initial phase. However, due to catabolism of the parent tracer with the surrounding chemical component in the blood, it can produce radio - metabolites which is the limitation for both imaged derived AIF and blood draws.

One general class of kinetic models is the compartmental model where different physiological/molecular states of the tracer are categorized into compartments with the conversion rates between compartments describe by rate constants. Over the past 50 years, various compartment models have been developed to quantify blood flow, cerebral metabolic rate of glucose, and receptor bindings of importance in cancer[27]. In compartment models, the blood vessels are treated as a compartment which carries with it the implicit

assumption that 'fresh' tracer delivered to the tissue by blood flow is instantaneously and uniformly mixed with tracer already in the blood vessels and furthermore the washout of tracer from blood vessels is also instantaneous rather than over a period, equal to the blood vessel transit time resulting in a tracer concentration gradient from the arterial to venous end. This consideration is important because, in dynamic PET imaging, the tracer is injected intravenously (systematically) and continues to recirculate throughout the whole body. During each transit of tracer through the vessels, there is continuous influx and efflux of tracer into the tissue over the transit time rather than instantaneously, failure to properly model the transit time but can, therefore, result in erroneous estimates of rate constants. The mean transit time effect is investigated in detail in Chapter 2.

In general, compartments models can be either *a priori* knowledge or data driven[28]. In the first approach, the prior knowledge is use to define the number of compartments as well as their interconnection to describe the kinetic behavior of the tracer. This approach allows for the estimation of rate constants that govern the transfer of tracer from one compartment to another. One such example, and is commonly used, is the standard two tissue compartment model to describe the kinetics of targeted tracers. On the other hand, data driven method does not require the number and interconnection of the compartments to be explicitly specified. Commonly used data driven approaches include graphical and spectral analysis. With graphical analysis, only summary kinetic parameters that are combinations of the compartment rate constants are estimated, e.g., unidirectional influx rate of irreversibly bound tracer from blood vessels into tissue and distribution volume. Spectral analysis gives spectrum of rate constants which are not interpretable as specific compartment rate constants, e.g. the binding or dissociation rate constant of targeted tracers.

1.2.3 Compartment models

1.2.3.1 Standard two tissue compartment (S2TC) model

The most commonly used compartment model for targeted tracer is the standard two tissue compartment (S2TC) model. As the name implies, the model is comprised of two tissue

Figure 1-2: Standard two tissue compartment (S2TC) model
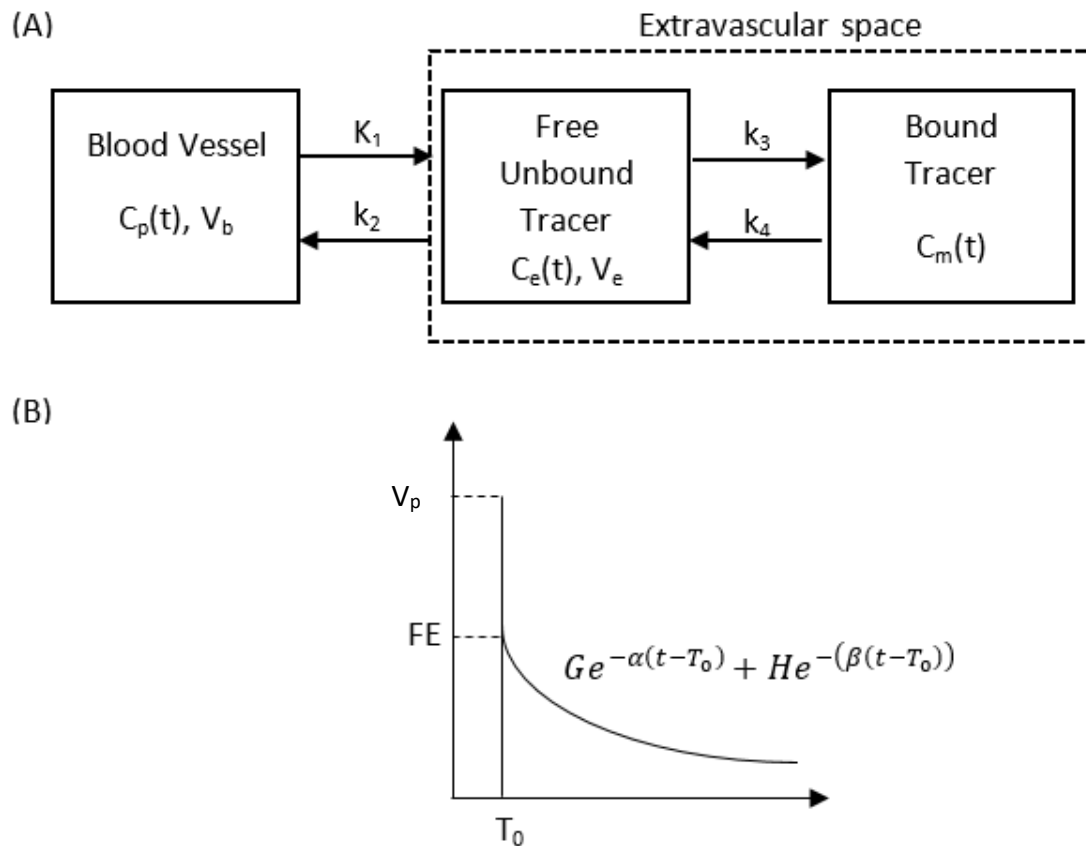
(A) Schematic of standard two tissue compartment model. Besides the blood vessel compartment, the two tissue compartments are one for free unbound tracer and one for bound tracer. The extravascular space (compartment) includes both tissue compartments. Rate constants describing the tracer transfer between compartments are defined in the text. (B) Corresponding impulse residue function for the model

compartments – one for free or unbound with concentration of $C_e(t)$ and one for tracer bound to the target with concentration $C_m(t)$ (Fig 1.2). Note that $C_e(t)$ and $C_m(t)$ are 'mass' concentration in units like mMole per gram of tissue. Tracer in blood vessels is also represented as a compartment with caveats discussed in §1.1.2.

The tracer kinetics as encapsulated by S2TC model can be concisely expressed by the following system of first order linear differential equations:

$$\frac{dC_e}{dt} = K_1 C_p + k_4 C_m - (k_2 + k_3)C_e \dots\dots\dots (1)$$

$$\frac{dC_m}{dt} = k_3 C_e - k_4 C_m \dots\dots\dots (2)$$

The rate constants are - K_1 is influx rate constant from blood vessel into the free tracer compartment in tissue, k_2 is the efflux rate constant back to the vessel, k_3 is binding rate constant to the target and k_4 is the disassociation rate constant from the target. The 'mass' concentration of tracer in the tissue, Q(t) including blood vessels and the two tissue compartments can be expressed as:

$$Q(t) = V_p C_p(t) + C_e + C_m \dots.. (3)$$

where V_P is the tissue blood volume in units of mL per gram of tissue and $C_p(t)$ is the arterial concentration in units of mMole per mL of blood or the AIF. E is the extraction efficiency and product of blood flow (F) with E is K_1.

Eqs. (1) and (2) can be solved algebraically using Laplace transform and the solution for Q(t) can be expressed as:

$$Q(t) = C_p(t) \otimes IRF_F(t) \dots\dots\dots (4)$$

$$IRF_F(t) = \begin{cases} 0 & 0 < t < T_0 \\ V_p \delta(t) & t = T_0 \\ Ge^{-\alpha(t-T_0)} + He^{-\beta(t-T_0)} & t > T_0 \end{cases} \dots\dots\dots (5)$$

$IRF_F(t)$ is the flow scaled impulse residue function. It is the idealized tissue tracer concentration in response to the tracer being injected as a tight bolus into the vessels supplying the tissue and $\otimes$ is the convolution operator, T_0 is the delay in tracer arrival at the tissue relative to that in the vessel where $C_p(t)$ or AIF is measured. This vessel could be the radial artery with manual blood sampling or a major vessel, like the aorta, with image derived AIF. The rest of the (model) parameters in Eq (5) are functions of the rate constants shown in Fig. 1.2:

$$\alpha = \frac{k_2 + k_3 + k_4 + \sqrt{(k_2 + k_3 + k_4)^2 - 4k_2k_4}}{2} \ldots \ldots \ldots (6)$$

$$\beta = \frac{k_2 + k_3 + k_4 - \sqrt{(k_2 + k_3 + k_4)^2 - 4k_2k_4}}{2} \ldots \ldots \ldots (7)$$

$$G = \frac{K_1(\alpha - k_3 - k_4)}{\alpha - \beta} \ldots \ldots \ldots (8)$$

$$H = \frac{K_1(k_3 + k_4 - \beta)}{\alpha - \beta} \ldots \ldots \ldots (9)$$

For ease of explanation (application of principle of conservation of mass), $Q(t)$, $C_e(t)$, $C_m(t)$ and $C_p(t)$ in Eqs (1-3) are expressed in natural units of mMole per g of tissue or per mL of blood. However, through calibration with a water phantom filled with uniform activity and assuming a tissue density of 1.0, all these variables can be expressed in consistent units of kBq per mL as measured by PET [29].

Due to the compartmental assumption of blood vessels, delivery of the tracer by blood flow (F) is not 'explicitly' modeled, 'fresh' tracer from the supplying blood vessels is assumed to instantaneously mix uniformly with tracer already present and also instantaneously washout from the blood vessels. This assumed tracer transport in blood vessels leads to the incorporation of a Dirac delta function of amplitude V_p at $t=T_0$ for the impulse residue function, $IRF_F(t)$ (Fig. 1.2).

1.2.3.2 Flow Modified Two Tissue Compartment (F2TC) Model

To address the shortcomings of assuming blood vessels as a compartment, we developed a model where all blood vessels are represented as a 'pipe' through which the tracer flows from arterial end to venous end with mean transit time W. To more realistically represent the delivery and transport of tracer starting at the blood vessels through to the bound compartment in tissue, we combine the Johnson-Wilson-Lee model (JWLM)[30] and the S2TC model. As in the JWLM, the perfusion delivery of tracer to the blood vessels as well as the influx and efflux of tracer to and from the free tracer compartment in the tissue

Figure 1-3: Flow modified two tissue compartment (F2TC) model
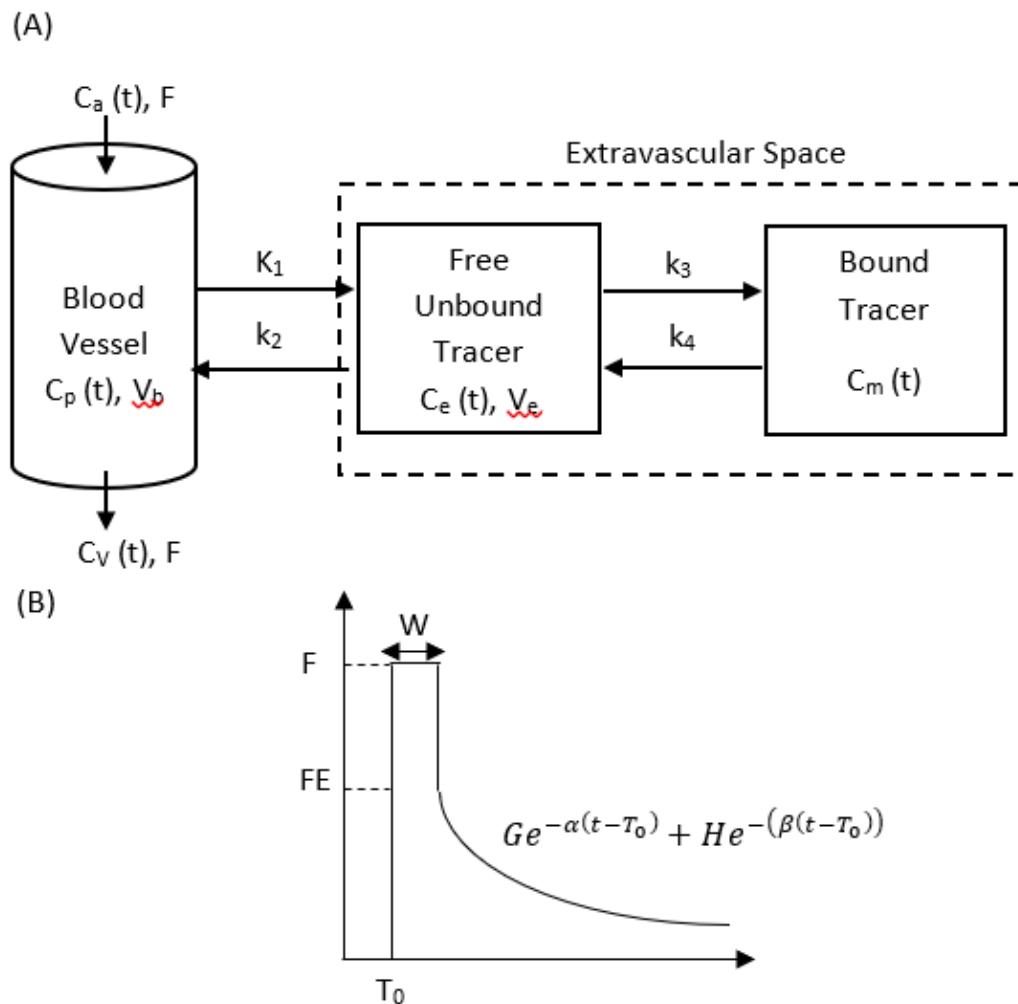
Schematic of flow modified two tissue compartment model. The tissue compartments, as in the S2TC model, are the free and bound pool. Blood vessels are a pipe with concentration gradient from the arterial ($C_a(t)$) to venous ($C_v(t)$) end with mean transit time W. Corresponding IRF is below the model. During the transit time of the tracer, the concentration of tracer in the tissue is constant, as indicated by the rectangular function in the IRF. The area under the rectangular function is the blood volume (V_p).

during the transit time were explicitly modelled; this approach results in a tracer concentration gradient in the vessel from the arterial to venous end as opposed to the instantaneous mixing and washout in S2TC model (Fig. 1.3).

In F2TC model, tracer transport between the two tissue compartments would lead to the bi-exponential decay in the impulse residue function as in the S2TC model. Combining the impulse residue function for the JWLM and S2TC model we arrive at that for the F2TC model as shown in Eq (10):

$$IRF_F(t) = \begin{cases} 0 & 0 \leq t < T_0 \\ F & T_0 \leq t < T_0 + W \\ Ge^{-\alpha(t-T_0-W)} + He^{-\beta(t-T_0-W)} & t \geq T_0 + W \end{cases} \text{ ... ... } (10)$$

where W is the mean transit time and G, H, α and β are described in equations (6-9).

The difference between the $IRF_F(t)$ of S2TC and F2TC model is that instead of a delta function (see Eq(5)), the vascular component of F2TC model $IRF_F(t)$ is described by a rectangular function of constant tracer concentration in the tissue, during the mean transit time as the tracer flows from arterial end to venous end. By necessity of conservation of mass, the constant tracer concentration here refers to the total tracer 'mass' in blood vessels as well as the two tissue compartments. Because of the dynamic distribution of tracer, the concentration in blood vessels, and individual tissue compartment would not be constant during the transit time of blood vessels. Because of its limited spatial resolution, PET is not able to differentiate among blood vessels and the tissue compartments, instead it measures the aggregate mass, Q(t) as expressed in Eq(3) and as in the S2TC model,

$$Q(t) = C_p(t) \otimes IRF_F(t) \text{ ... ... } (11)$$

where $IRF_F(t)$ is given by Eq(10) instead of Eq (5).

1.2.4 Estimation of S2TC and F2TC model parameters

Both the S2TC and F2TC model are nonlinear because there are exponential terms in the corresponding $IRF_F(t)$. To estimate kinetic parameters, these parameters are iteratively adjusted from given starting values to fit the measured tissue TAC, Q(t) as closely as possible using non-linear least squares optimization method. The goodness of fit is

measured by the root mean squared deviations (RMSD) between the measured and model fitted curve.

$$RMSD = \sqrt{\frac{1}{N}\sum_{i=0}^{N}(x_i - y_i)^2} \ldots\ldots\ldots (12)$$

where x_i and y_i are the data points of the measured and fitted curve respectively, i is the index of time points and N is the number of time points in the dynamic PET acquisition.

The fitted curve with the least RMSD provides the optimal kinetic parameters for the measured tissue TAC. For analyzing tracers that are irreversibly bound, the k_4 values can be set to 0. According to central volume theorem[31], blood volume, V_p can estimated as:

$$V_p = F \times W \ldots\ldots\ldots (13)$$

1.2.5 Graphical Analysis

Graphical Analysis is based on compartmental model but does not require *a priori* knowledge of the model structure – number of compartments and their specific interconnections. It derives summary parameters rather than the rate constants of the model by linear regression of transformed AIF and tissue TAC. There are two kinds of graphical analysis: Logan plot is used for analysis of reversibly bound tracer and Patlak for analysis of irreversibly bound tracer. The major advantage of the method is that it can be used to validate the reversibility or irreversibility of tracer binding without requiring prior detailed knowledge of tracer binding mechanism. However, graphical analysis requires the transformed data to reach linearity which could be affected by noise[32].

1.2.5.1 Patlak Graphical Analysis

Patlak plot was initially developed for analysis of influx rate across the blood brain barrier for irreversibly bound tracer in the brain. The plot is based on non-linear transformation of the tissue TAC and AIF as shown in the following equation:

$$\frac{Q(t)}{C_p(t)} = K_i \frac{\int_0^T C_p(t)dt}{C_p(t)} + (V_e + V_p) \dots\dots\dots (14)$$

where $Q(t)$ and $C_p(t)$ are the tissue TAC and AIF respectively. The slope of the linear regression of the transformed data is the unidirectional influx rate constant (K_i) which is the ratio of the mass of tracer diffused out of vessel to that of the tracer plasma concentration under equilibrium distribution condition[33].

The intercept of the Patlak plot is $V_e + V_p$, where V_e is the distribution volume of free and unbound tracer[33–35].

With the S2TC and F2TC model, the unidirectional influx rate constant of tracer can be expressed in terms of the model rate constants as:

$$K_i = \frac{k_1 k_3}{k_2 + k_3} \dots\dots\dots (15a)$$

For reversible binding tracer, besides the unidirectional influx rate constant from blood vessels to the bound compartment, NET influx rate constant is given as:

$$K_{net} = \frac{k_1 k_3}{k_2 + k_3 + k_4} \dots\dots\dots (15b)$$

1.2.5.2 Logan graphical analysis

Logan plot is used for analyzing tracers that are not irreversibly bound to the target, that is, k_4 is non-zero. The equation describing the plot is:

$$\frac{\int_0^t Q(t)dt}{Q(t)} = V_T \cdot \frac{\int_0^T C_p(t)dt}{Q(t)} + Int. \dots\dots\dots (16)$$

It plots the integral of tissue TAC against integral of arterial TAC, both normalized by Q(t). The slope of the curve is the total distribution volume (V_T). The plot is linear when the intercept (Int.) becomes constant[34].

$$Int. = \frac{C_e(t) + C_m(t)}{C_p(t)} \ \dots \dots \dots (17)$$

Here V_T is a theoretical volume defined as the ratio of tracer concentration in the tissue (free and bound compartment) to that in blood vessel at distribution equilibrium. Similar to Patlak plot, V_T can also be expressed in terms of rate constants of the S2TC or F2TC model as:

$$V_T = \frac{K_1}{k_2}\left(1 + \frac{k_3}{k_4}\right) + V_p \ \dots \dots \dots (18)$$

For a one tissue compartment model or for modelling inert tracers, distribution volume (DV) is equivalent to V_e which is DV for free and unbound tracer (excluding V_p)[35] and it is expressed as:

$$V_e = DV = \frac{K_1}{k_2} \ \dots \dots \dots (19)$$

1.2.6 Spectral Analysis

Like graphical analysis, spectral analysis is also data driven rather than based on a proposed model. If the distribution of tracer is linear and stationary in time as well as that the PET signal (image intensity) is linear with respect to tracer concentration, based on the principle of linear superimposition, the tissue TAC corresponding to an intravenous injection of the tracer is given by Eq (4). However, instead of two decaying exponentials as in the case of S2TC model, the IRF(t) is defined by a pre-defined number of exponents (usually 100-1000):

$$IRF(t) = \sum_{i=0}^{n} A_i e^{-\alpha_i t} \ \dots \dots \dots (20)$$

where i is the index of the n predefined exponentials and A_i is the coefficient of the ith exponential. The A_i's can be estimated with linear least square method, preferably with non-negative constraint[27]. The advantage of spectral analysis is that it does not presuppose

Figure 1-4: Tumor microenvironment
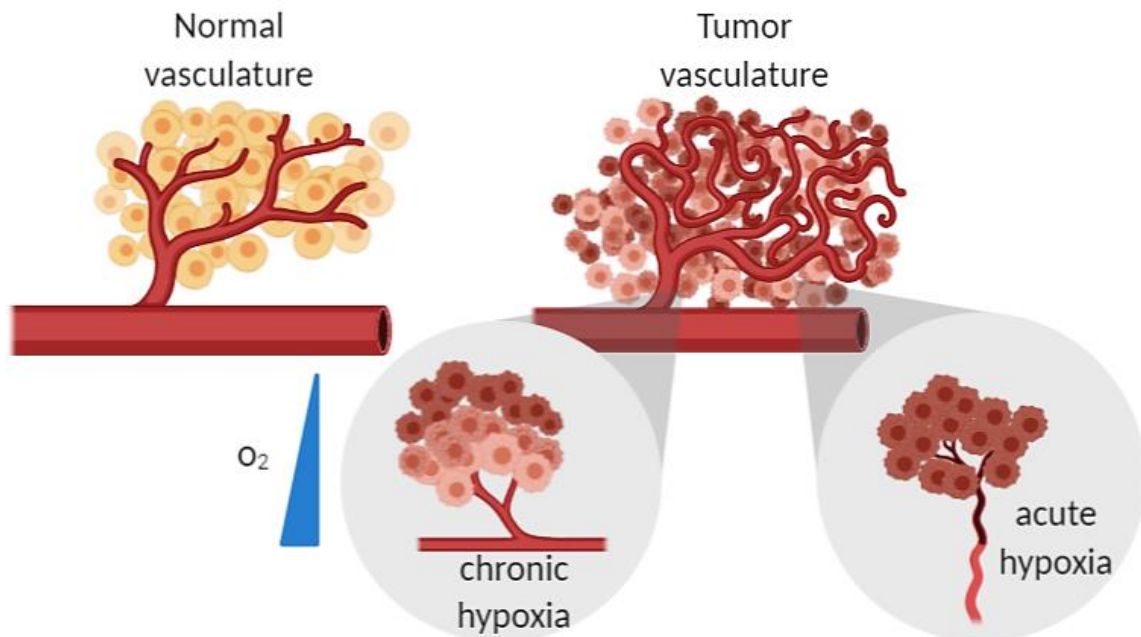
Schematic illustration of blood vessels in healthy and tumor tissue. In the streamlined healthy vascular network, capillaries and venules provide adequate supply of oxygen to meet demand, resulting in normoxia. On the contrary, tumor blood vessels are tortuous and irregular creating pockets of nutrient and oxygen deficient regions. In chronic hypoxic, because of diffusion limitation, cells that are far away from the blood vessels (~100μm), can experience insufficient supply of oxygen and nutrients to meet their metabolic demand, resulting in hypoxia. Acute hypoxia is caused by the collapse of blood vessels in different parts of the tumor for a brief period because tumor blood flow can occasionally fluctuate quite erratically, cutting off blood and oxygen supply to cells in those territories resulting in hypoxia .

the number of exponentials (compartments and their interconnection), that is, it is 'agnostic' to compartment structure. This 'agnostic' nature of the spectral analysis would have the shortcoming that it is difficult to relate exponentials with non-zero A_i's to rate constants of specific kinetic processes, for example, influx rate constant of tracer from blood vessels to tissue or binding rate constant of tracer to its target etc.

1.3 Cancer Imaging

Cancer cells are rapidly growing cells and glucose is the main source of energy for their metabolism. ^{18}F-FDG is an analog of glucose and like glucose, it is rapidly transported into cancer cells. Unlike glucose, ^{18}F-FDG does not partake in the subsequent glycolysis steps

after the initial phosphorylation by hexose due to the labelling of ^{18}F in the C-2 position. [^{18}F]FDG is trapped in the cells as ^{18}F-FDG-6-P once it is phosphorylated by glycolysis[36]. However, in rapidly growing tumors with heterogeneous distribution of blood vessels, the insufficient supply of oxygen can result in a hypovascular core leading to hypoxia because of the imbalance between supply and demand for oxygen from glycolysis as well as other metabolic and cellular processes. Since [^{18}F]FDG participates in the glycolysis pathway, it cannot be used for imaging the decreased level of oxygen (hypoxia) in solid tumor.

1.3.1 Hypoxia

Hypoxia is a common feature of solid tumors due to imbalance in the supply and utilization of oxygen in the uncontrolled tumor cell proliferation. Hypoxia can be classified into two types: chronic and acute hypoxia (Fig 1.4). Chronic hypoxia is caused by diffusion limited oxygen transport to the tumor cells. Oxygen and nutrient transport in tissues are dominated by diffusion. Cells that are in close proximity to blood vessels consume the available oxygen and nutrient while cells further from vessels are oxygen deprived and not capable of maintaining their regular cell metabolism. The cells will eventually adapt to the lack of oxygen which will affect their response to treatment or die resulting in necrotic regions[6,37–39]. Hypoxia is defined as a partial oxygen (pO2) pressure < 5mm Hg compared to normal tissues with pO2 > 40mm Hg[40,41].

In solid tumors, the vasculature is not streamlined like the normal tissue (Fig. 1.4). The tortuous structure of the vessels may be perfused only by the plasma or may not be perfused at all. Despite the presence of vessels, the regional tissues may not be supplied by oxygen. Hypoxia can also be caused by raised interstitial fluid pressure resulting in intermittent or cycling hypoxia condition. These perfusion limited and short term hypoxia is called acute hypoxia which is deemed more resistant to therapy[38,42,43].

1.3.2 Hypoxia and radiation resistance

In 1953, Grey et al.[41] identified the significance of oxygen in radiation treatment and hypoxia in treatment resistance. Breathing oxygen before irradiation showed instantaneous increase in radio-sensitivity with no significant increase beyond pO$_2$ of 20 mmHg. The

radio-sensitivity of high linear energy transfer (LET) radiation like neutrons is not significantly affected with increasing oxygen content. Normal cells can sustain ~3 times more radiation damage compared to hypoxic cells[42,44]. With single radiation dose fraction, hypoxia can limit radio-sensitivity. On the other hand, with fractionated radiotherapy, re-oxygenation may occur between radiation fractions. This depends on the dose delivered and on the type of cancer cell[45,46].

Radiation kill cells either directly by DNA damage, particularly for high LET radiation like electrons and neutrons or indirectly via intermediary products like free radicals. The more common cell death is through the indirect method. It refers to interaction of radiation with macromolecules in the cytoplasm to liberate high energy electrons which in turn interacts with other molecules like water. The electrons interaction with water creates highly reactive hydroxyl radicals which can be removed by recombination with other free radicals (like $\dot{H}$ to produce water) or by hydrogen donated from thiol compounds (such as glutathione, GSH) to produce much less reactive (damaging) radicals. The hydroxyl radical can combine with oxygen to form highly reactive oxygen species (ROS) like peroxyl radical. All these free radicals can easily diffuse and cause damage away from the origin of the first interaction. Indirect damage is most common for low LET radiation. Since 70% of human body is composed of water, most of the radiation induced injury arises indirectly from the products of interaction with water as described above[38,47]. Therefore, radiation cell kill requires oxygen and low oxygen level inhibits DNA double strand break thereby enhancing cell survival.[6,40,44].

1.3.3 Chemo-resistance in hypoxia

Hypoxic cells in an attempt to survive and propagate in an oxygen limited environment, are likely to develop a more aggressive tumor phenotype. The gene induced by hypoxia is regulated by a transcription factor called hypoxia inducible factor (HIF-1). It induces the expression of genes such as vascular endothelial growth factor (VEGF), glucose transporter-1 (GLUT-1) and multidrug resistance protein (MDR) which have direct or indirect resistance to chemotherapy[48,49].

VEGF is also called vascular permeability factor since it increases vessel permeability and angiogenesis[48,50]. Increased vessel permeability can lead to increase interstitial fluid pressure which would impede the delivery of chemo-drugs by perfusion. GLUT-1 is a transporter protein that facilitates entry of glucose into tumor cells. Under hypoxic condition in tumors, overexpression of the protein compensates for the higher energy demand of tumors since glycolysis can occur in low oxygen environment to maintain the energy supply of tumors[51]. This alternate pathway could explain why GLUT-1 indirectly induce chemo-resistance. The role of MDR is discussed in detail under §1.3.7.

1.3.4 Pancreatic cancer

Pancreatic cancer (PCa) also known as pancreatic ductal adenocarcinoma is a cancer of ductal epithelium and one of the worst solid cancers because of extremely poor prognosis. According to American National Cancer Institute cancer statistics from 2009-2015, the overall 5-year survival rate is 9.3% [52]. It is difficult to diagnose PCa early since symptoms do not appear until it is in an advanced stage or has metastasized. Pancreas is a deeply situated organs surrounded by other organs at very close proximity, hence it metastasizes easily and it cannot be palpated by health professional during routine exams[53]. Only 40% of patients with localized disease is surgically resectable. It has been established that PCa have low oxygen tension. The partial oxygen pressure (pO_2) of tumor is <5 mmHg and normal pancreatic tissues has a much higher pO_2 >24 mm of Hg[54]. It is highly resistant to chemotherapy, radiation therapy and immunotherapy[55] and low oxygen tension (hypoxia) is one of the contributing factors.

1.3.5 Treatment options for pancreatic cancer

Surgical resection alone is not sufficient for pancreatic cancer treatment as invariably microscopic disease remains in the resection margins. Whipple surgery, a surgical procedure to remove the head of the pancreas along with lymph node dissection, did not improve the overall survival[56]. A randomized trial in 1969 found that patients with unresectable pancreatic cancer treated with 5-fluorouracil (5-FU) along with radiation therapy had improved survival of 10 months compared to radiation or chemotherapy

alone[57,58]. According to the European Study Group for Pancreatic Cancer 1 Trial, the five year survival rate for resected pancreatic cancer was 10 percent for patients receiving chemoradiotherapy (CR) while the percentage was much higher (21%) for those who received chemotherapy with 5-FU alone[59]. Another study comparing CR with chemotherapy in the American cancer database sponsored by American College of Surgeons and American Cancer Society, showed that radiation improved overall survival (OS) by ~3 months on average. However, for node negative patients, radiation proved no benefit to OS [60]. Despite these small improvements in survival, prognosis of PCa is still very poor.

1.3.6 Chemo-resistance in pancreatic cancer

In pancreatic cancer and in many solid tumors, chemo-resistance is from the failure to accumulate enough concentration of cytotoxic drugs due to the efflux of these drugs from tumor cells. Proteins mediating the efflux of drugs belong to the ATP binding cassette (ABC) transporters. The family of ABC transporter responsible for mediating the drug resistance is the ABC family B and C (ABCB, ABCC), particularly the multidrug resistance protein (MDR1) P-glycoprotein (P-pg) and multidrug resistance-associated protein (MRP) 1-9. MRPs are adenosine triphosphate (ATP) dependent transmembrane protein responsible for efflux of organic anion as well as toxins in the cancer cells including cytotoxins and drugs. In particular MRP1, MRP2, MRP3 and MRP6 accounts for transport of lipophilic compounds conjugated to glutathione, glucoronate and sulfate[61,62]. MDR1 P-gp is also a membrane protein that directly efflux toxins out of the cells and it is implicated in chemo-resistance[62,63]. While there is an increased expression of MDR1-Pg and MRP1 in pancreatic cancer, there is no correlation with tumor staging or grading. Instead, mRNA for MRP3 and MRP5 are upregulated in pancreatic cancer and correlated with tumor grading[64–66].

1.3.7 Measurement of hypoxia

As discussed in §1.3.1-3, oxygen tension is a determinant of response to cancer therapy, the ability to measure tumor oxygen tension is of significant importance in treatment planning.

1.3.7.1   Polarography needle electrode system

Several techniques have been developed in the past to measure tissue oxygen tension. One such system is the commercially available Eppendorf pO_2 probe. It is invasive requiring insertion of the electrode into the tumor; the technique is limited to easily accessible tumors like the head and neck tumors, breast cancer and skin lesions[42,67]. For normal superficial tissue, pO_2 as measured by the Eppendorf probe is 40-60mmHg while hypoxic tissues have pO_2 <10mmHg[68]. In necrotic tumors where the oxygen content is significantly reduced, the probe cannot differentiate hypoxia from necrosis.

Non-invasive imaging techniques to measure hypoxia have been developed, including Magnetic Resonance Imaging (MRI) and Positron Emission Tomography (PET).

1.3.7.2   MRI measurement

MRI is an anatomical and functional imaging technique with good spatial resolution. Different functional information can be achieved with various MRI sequences. Most of the MRI images are taken using gradient echo (GRE) sequence generated due to changes in T_2^* relaxation time. T_2^* is a combination of signal due to spin-spin dephasing as well as inhomogeneity of the magnetic field. T_2^* weighted GRE sequence is the most commonly used blood oxygenation level dependent (BOLD) imaging which is influenced by susceptibility due to changes in oxygenation in the blood. BOLD takes advantage of the difference in paramagnetism of the deoxy and oxy- hemoglobin in the blood vessel. Paramagnetism causes large dephasing of spin-spin lattice which further causes inhomogeneity of water proton spins in the surrounding tissues, resulting in shortening of T_2^* signal[69]. It measures change in the oxygenation in vasculature rather than the tissue pO_2 which is important in determining the radiosensitivity[69,70]. BOLD signal only showed

correlation with temporal change in pO2 with no correlation in its magnitude. The signals can be confounded by several factors like blood flow, hematocrit concentration and the interconversion of oxy- and deoxy-hemoglobin[43,71,72]. For measuring oxygen content in the tissues, a technique similar to BOLD – tissue oxygenation level dependent (TOLD) MRI can be used. Unlike BOLD, TOLD relies on T_1 relaxation which is caused by the presence of dissolved oxygen[73].

1.3.7.3 PET imaging

A more sensitive method capable of measuring cellular oxygen level is PET. Due to upregulation of GLUTs in tumor cell membrane[74] and as HIF-1α drives glycolytic enzymes[75], [^{18}F]FDG could be used as surrogate marker for hypoxia. However, studies have reported conflicting results with some reporting that [^{18}F]FDG is not a good marker for hypoxia[6,76,77]. The cause of the discrepancies is because under reduced oxygen, the cells adapt to the environment and it undergoes anaerobic glycolysis instead of aerobic ATP production pathway. In addition, HIF-1α is also expressed in normoxic tissues resulting in non-specific uptake of [^{18}F]FDG[6].

Multiple hypoxia PET tracers have been developed in the past. Since hypoxic cells have limited blood flow to the tissue, sensitivity of the imaging probe is necessary. The contrast between the hypoxic region and the normoxia region depends on how much the tracer enters into the cell, the fraction of the tracer that undergoes reduction in the tissue, the rate of clearance of the tracer from normoxic tissues and the retention time in the hypoxic cells[78]. The commonly used nitroimidazole (NI) based hypoxia PET tracer are ^{18}F-fluoromisonidazole ([^{18}F] FMISO) and ^{18}F-fluoroazomycin arabinoside ([^{18}F]FAZA). NI were initially developed as radiosensitizers for hypoxic cells[40].

In view of the distance the tracers have to diffuse to the tumor cells which varies with different tumor types, static image acquisition is not an ideal method to distinguish hypoxia from normoxic tissues. Kinetic modelling which models the distribution and assess the reaction rate of tracer accumulation is more applicable in quantifying hypoxia[79].

Figure 1-5: Binding mechanism of [^{18}F]FAZA (nitroimidazole) in hypoxic cell
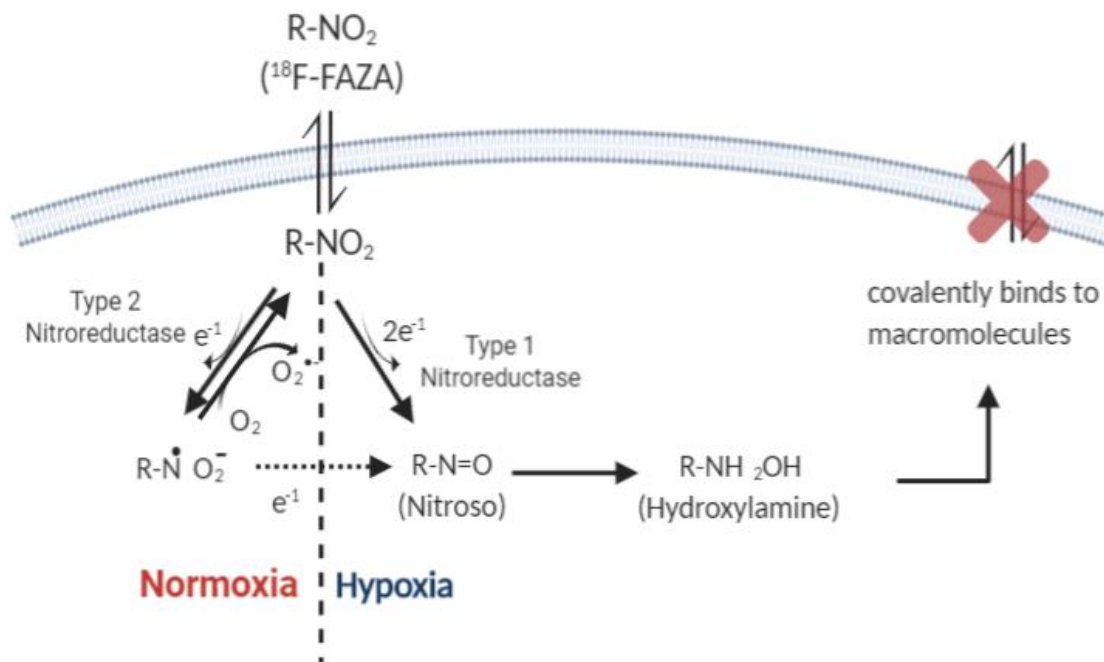
Schematic representation of [^{18}F]FAZA imaging. In normoxia, [^{18}F]FAZA is reduced by type 2 nitroreductase to nitro-oxide radical which in presence of oxygen can revert back to its original form and diffuse out of the cell. Under hypoxia condition, the nitro-oxide radical is converted into nitroso and hydroxylamine that can covalently bind to macromolecule and get trapped in the hypoxic cell.

1.3.7.4 Mechanism of action for nitroimidazoles

Nitroimidazoles are lipophilic compounds and it enter the cell through passive diffusion. NI undergoes certain degree of reduction in all the cells but in the absence of adequate oxygen supply, it undergoes further reduction. The nitro groups can be reduced by enzymes called nitroreductase, the first step of NI compound breakdown. There are two groups of nitroreductase, based on their reduction ability due to one or two electron transfer[78,80]:

1. Type 1 nitroreductase: It is oxygen insensitive enzyme, in the presence or absence of oxygen, it transfers two electrons from nicotinamide adenine dinucleotide phosphate (NADP) to its nitro group of the NI compound, producing nitroso and hydroxylamine intermediates. However, the nitroso group is so reactive and the

second two-electron transfer to form hydroxylamine is much faster than the first transfer, it is difficult to isolate the two.

2. Type 2 nitroreductase: It is oxygen sensitive enzyme which catalyzes single electron reduction to it nitro anion radical. It forms superoxide radical and due to high oxygen affinity, the radical reverts back to its original form. The cycle produces oxidative stress by producing large amounts of super-oxides. The successive steps is determinant in differentiating normal tissue from hypoxic tissue. In absence of oxygen, the re-oxygenation or formation of superoxide radical is slowed allowing for further reduction to take place. The superoxide is reduced to nitroso and hydroxylamine which binds to macromolecules like DNA, RNA and proteins that eventually gets trapped in the cell[81]. Due to the oxygen-sensitivity of this type of nitroreductase, it is of importance in hypoxia imaging.

1.3.8 Hypoxia tracers

$[^{18}F]$FMISO is a first generation hypoxia NI based tracer. It is a lipophilic tracer which allows for easy diffusion into the cell. Several studies have shown that the tracer can detect hypoxia in different tumors types like glioma, head and neck cancer and breast cancer[82–84]. Gagel et al. found good correlation between measurements from polarography needle and $[^{18}F]$FMISO uptake in head and neck tumor for $pO_2 < 10$ mmHg after 2 hour of uptake[85]. $[^{18}F]$FMISO have been shown to be a potential tracer to grade gliomas. Using a tumor to blood radio (T/B) threshold of 1.2, the uptake of tracer was in small in low grade tumor compared to high grade glioma[86]. Higher $[^{18}F]$FMISO uptake was also observed for estrogen receptor (ER) positive breast cancer and is shown to be a strong predictor of disease free survival[84]. Due to the slow plasma clearance of the tracer and hence high background activity, the tracer needs to be injected for at least two hours before the uptake of tracer can be visualized. In addition, it requires very low $pO_2 < 10$mmHg for significant $[^{18}F]$FMISO uptake[71,72,81,87].

To address the issue of slow tracer clearance, second generation 2-nitroimidazole was developed, $[^{18}F]$fluoroazyomycin arabinoside ($[^{18}F]$FAZA). The imaging mechanism is similar to $[^{18}F]$FMISO. The major advantage of $[^{18}F]$FAZA is that the tracer is more

hydrophilic with higher perfusion and higher clearance and hence higher tumor to background ratio than [^{18}F]FMISO. Maximal uptake of the tracer is observed at 2 hr p.i. while there is continual increase in uptake even at 6 hr p.i. for [^{18}F]FMISO[87]. [^{18}F]FAZA showed significantly higher uptake of tracer in the hypoxic tumors of pancreatic acinar tumor cell line compared to [^{18}F]FMISO. Furthermore, the uptake was higher in animal breathing normal air than in animals breathing pure oxygen[88]. [^{18}F]FAZA showed promising result in predicting treatment response for murine breast cancer cell line treated with chemotherapeutic drug (Triapazamine) along with radiation therapy. Significant decreased uptake and decreased tumor growth was shown in rats that underwent chemoradiation while radiation only treatment showed delay in tumor growth[89].

1.4 Radio-metabolite production

For detailed analysis of pharmacokinetics of tracer uptake in the diseased tissues, arterial blood sampling from several time points are required (see §1.2.3). The blood samples or the imaged derived AIF could be contaminated with metabolites, introducing biases in kinetic parameter estimation. Upon introduction of tracer into the blood vessel, it is immediately catabolized by chemicals like enzymes, proteases, oxidizing and hydrolyzing agent[90–92]. The biotransformation results in chemically different compounds called metabolites while the fraction of parent compound decreases. Metabolites that are tagged with radioactive element are called radio-metabolites. PET detects total signal from coincidental gamma photons that are emitted due to annihilation event. It is impossible for the detector to differentiate if the signal is originating from the innate tracer or from the radioactive element attached to the metabolites. Radio-metabolites are problematic in PET quantification since metabolites are completely different entity that can have different bio-distribution[93]. Therefore, if not accounted for in the blood plasma, can introduce biases in quantifying any dynamic PET. In addition, if deeper understanding of the physiological and pathological information is needed, detection and identification of the radio-metabolite is necessary.

Fractions of unchanged radiotracer in the blood plasma can be measured using high performance liquid chromatography (HPLC), thin layer chromatography (TLC) and other

chromatographic technique. Chromatography techniques are usually limited to the number of samples that can be analyzed. Blood samples that are taken at later time points suffer from noisy counting statistics due to reduced tracer activity [94]. Different approaches have been adopted for measuring plasma radio-metabolite. One such method is the individualized method where fraction of tracer is calculated for each individual patient. Since each individual patient are limited to small blood sample, it can introduce error due to sparse sampling. Thus, population-based method where a model is fitted through the average of the measurement taken across the population is preferred. It removes the requirement of metabolite measurement for each individual patient, however, the existence of inter-subject variability can be erroneous.

1.4.1 Separation of radio-metabolites

Several studies in the past have measured radio-metabolites. One such study was done by Rusjan et al., where he determined blood plasma radio-metabolite for [^{18}F]FEPPA binding to translocator protein in the brain. The fraction of unmodified tracer was estimated using reverse phase HPLC. For the tracer, fast metabolism was observed with 80% metabolized in the first 30 minutes. The rate of metabolism slowed with time with the presence of at least three radio-metabolites[95].

To account for radio-metabolite in the tissue double input compartment model (DICM) was developed. DICM was used by several studies in the past[96–98]. Tomasi et al., compared the kinetic parameters estimated using single input compartment model (SICM), DICM and double input spectral analysis (DISA) for two tracers: 5-[^{18}F]fluorouracil (5-[^{18}F]FU) and [^{18}F]fluorothymidine ([^{18}F]FLT). For the tracer 5-[^{18}F]FU, the fit of the curve is superior with double input method as indicated by Akaike information criteria and the quality of the fit. Distribution volume between DICM and DISA were in perfect agreement. Furthermore, the influence of DI method is dependent on the tracer. The method is more prominent for tracers that have higher metabolism, in this case 5-[^{18}F]FU, compared to ^{18}F-FLT that has lower rate of metabolism. Radio -metabolite did not show any effect on k_i estimate[97].

1.4.2 Chromatography

The fraction of unmodified or parent tracer in plasma is measured with chromatography technique like HPLC, TLC and solid phase extraction (SPE). Chromatography is a technique used to separate chemical components or analytes in a solvent using two immiscible liquid called phases, one that is usually fixated to a surface (stationary) while the mobile one called the mobile phase. The basic principle of chromatographic separation is that the solvent or the mobile phase containing the sample is continuously transported through the stationary phase. As the mobile phase flows through the stationary phase, the interaction between the phases separate or distribute the analytes. The separation is based on the properties of the phases, as determined by the intermolecular forces like polarity, ion-ion interaction, and size exclusion and so on. For the thesis in chapter 4, the separation is based on polarity. Stationary phase in column chromatography is usually a polar solvent that is fixated into a packing material like silica while in planar chromatography, silica is a thin monolayer fixated on a solid backing like glass or alumina plate. As the mobile phase containing the analyte flows through the stationary phase, the difference in the polarity separates the individual component. The sample flows through the stationary phase at same velocity as the mobile phase. The analyte that has stronger affinity with the stationary phase will spend greater proportion of time in the solid phase. In the case of separation based on polarity, analyte that is the more polar will flow through at a slower rate compared to analyte that are less polar. The differential spatial retention results in the separation of the analyte as they move through the system[99,100].

The instrumentation of each individual technique is described below:

1.4.2.1 Thin Layer Chromatography (TLC)

Thin layer chromatography is a planar chromatographic technique in which the stationary phase is supported on a planar surface. For TLC, the stationary phase is a silica gel backed on a glass or aluminum plate. In planar chromatography, the sample is spotted on a marked position, usually 1 cm from the bottom of the plate, on the silica surface. The mobile phase is allowed to develop or evaporate in a development tank with a sealable top. After the

Figure 1-6: Separation of metabolites by Thin Layer Chromatography (TLC)
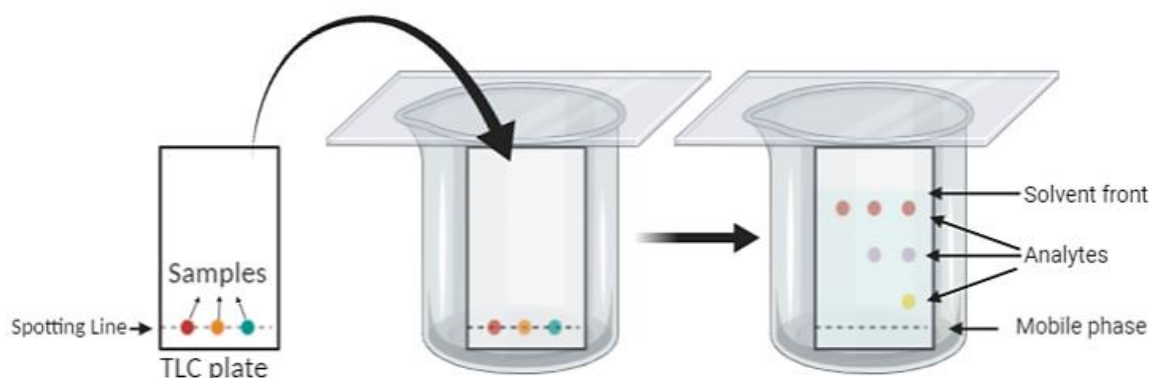
Separation of metabolite with TLC based on differences in polarity. Mobile phase acts as the solvent to carry the analyte through the plate by capillary action. In this example, three samples are spotted on the TLC plate and after immersing in the mobile phase for some time, analytes in the samples are separated by their polarity. Since silica is solid phase, the least polar the analyte is, the furthest it will move from the bottom of the plate.

development and drying of the spots on the TLC plate, bottom of the plate containing the spot is immersed in the mobile phase at an upright position such that the mobile phase front is below the sample spots. As the mobile phase permeates through the silica gel by capillary action, it separate the analytes based on polarity in the direction of the flow. After the mobile phase have migrated to specified distance, usually 1cm from the top of the plate, the plate is removed from the tank and air dried. The point at which the mobile phase moved furthest is called the solvent front[99,101].

TLC is an economical, simple and robust technique. However, it suffers from low spatial resolution and low sensitivity[102]. This led to the use of high performance TLC (HPTLC). It has many improvement compared to TLC in that the particle size of the solid phase in HPTLC is smaller (5-15µm) compared to 20 µm for conventional TLC. The smaller and more uniform and thinner layer contributes to reduced background noise, higher efficiency and tighter spots as a result of reduced spot spreading per plate length. Though HPTLC has better performance, the price tag associated with the instrumentation have prevented a rapid growth in its utilization[99]. Different method involved in detecting the radioactivity for radioactive sample is discussed in §1.4.3.

Figure 1-7: Mechanism of radio-metabolite separation using high performance liquid chromatography (HPLC)
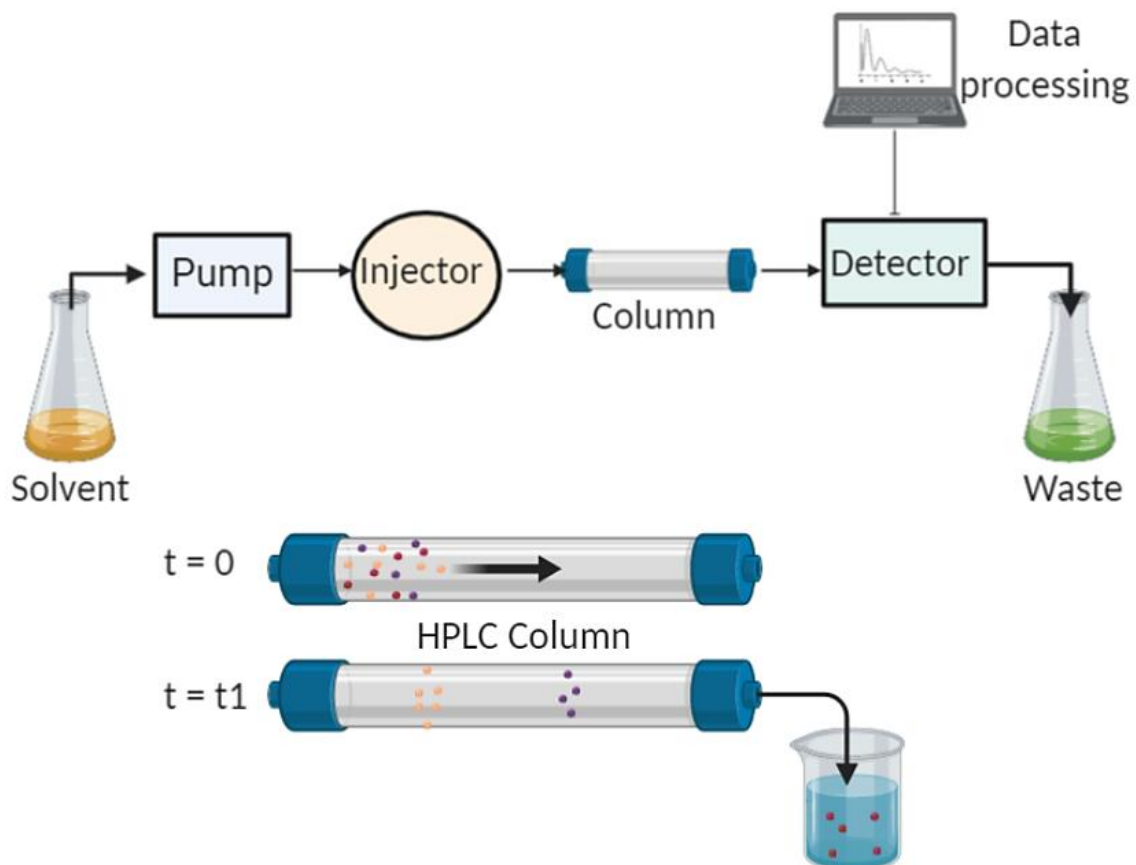
HPLC is composed of solvent that is pumped into HPLC column by a pump. The sample is injected into the solvent before entering the column. The eluent from the column is then passed through the detector which is connected to a data processing system creating chromatograph. Analyte in HPLC column, coated with polar solvent, are separated according to polarity. At time 0, solvent containing sample is injected into the column. With time, as the solvent flows through the column, the analyte that is more polar is retained in the column longer and is eluted out the last.

1.4.2.2 High Performance Liquid Chromatography (HPLC)

HPLC have gained popularity in the late 1980's due to its high performance and less labor intensive procedure. The basic principle is the same as TLC. HPLC is a complex instrument consisting of several components. It consists of a reservoir containing the solvent or mobile phase that delivers sample into HPLC column with a pump. It is designed for delivery at constant flow rate and pressure. An injector, either manual or automatic, injects the sample into the solvent before being delivered into the column. The column contains stationary

phase, usually silica packed material, responsible for separating the analyte in the mobile phase. The eluents containing the analytes are then collected and passed through detectors for signal generation. Depending on the properties of the mobile phase, the detector system could be UV light absorbance, conductance, fluorescence or a scintillation detector for radioactive element (radio-HPLC). The data or signal is then collected by a computer to generate chromatograph that can be quantified as concentration of analyte in the solvent[99,100,103].

Radio-HPLC is a very sensitive system with high resolution. Both the photons and positrons can be detected by scintillation detectors. The eluent tube containing the eluents after analyte separation are coiled for larger surface area. The scintillation detector are oriented in a way that coincidence photons caused by annihilation photons are detected in opposite direction thus reducing background noise[93,101].

There are pros and cons of using HPLC over TLC. TLC is more economical and robust. Unlike HPLC where samples are injected serially, TLC can analyze multiple sample at a time which is especially important for short lived isotopes[101]. Therefore, for HPLC which requires an operator to be present can be subjected to unnecessary radiation exposure in the radioactive samples. HPLC is time limited while TLC is spatially limited. In HPLC column, the samples flow though same distance and are separated with time influenced by flow rate of the mobile phase. TLC, on the other hand, all samples have same separation time and they are separated in space[99]. The eluting of the column in HPLC with solvent can clog the column which will require cleaning and unclogging before operation. This results in 'memory' contamination since the column is reusable and unlike TLC, it is a single use plate. For TLC, there are more robust against minor impurities in the stationary phase matrix[93,101]. HPLC boasts of higher spatial resolution compared to TLC.

1.4.2.3 Solid phase extraction (SPE):

Solid phase extraction is a chromatographic technique[104] with several advantages over TLC and HPLC. It requires less solvent, easier to use, convenient and it can easily be automated. It is based on the principle of separation by filtration and decantation by retaining or absorbing the analytes from the sample with stationary phase immobilized on a packing

Figure 1-8: Separation of metabolites using Solid Phase Extraction (SPE)
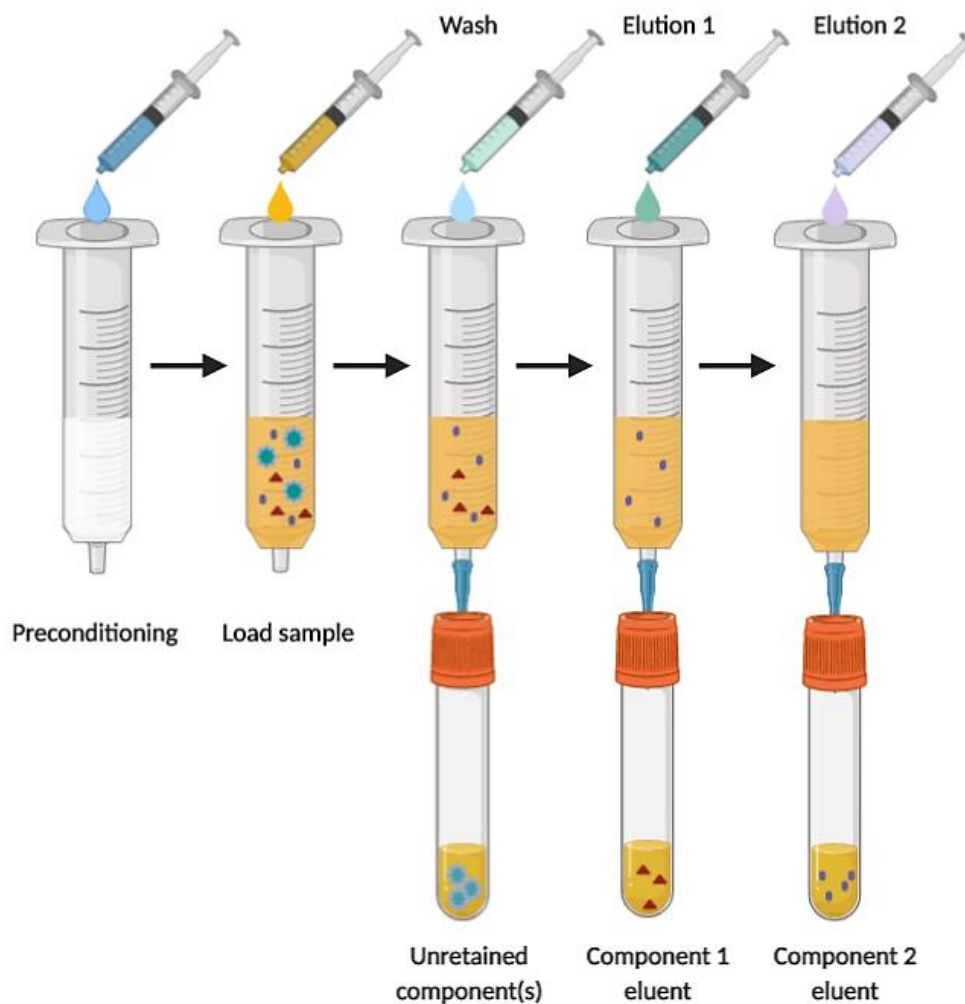
SPE consists of a cartridge packed with silica gel fiber. The cartridge is preconditioned with a solvent before loading the sample. It is then washed to remove unnecessary or waste component followed by elution with a solvent to elute out a least polar analyte. Subsequent elusions are performed with solvents that are more polar than the previous ones to elute out analytes more polar than the preceding ones. The eluted solvents are then passed through detector for activity measurement or an HPLC for analyte identification.

material. Silica is usually used as the packing material contained in a cartridge. The general first step of separation is preconditioning the cartridge for removal of contaminants in order to improve the efficiency, performance and reproducibility of result. Preconditioning involves passing a small volume of appropriate solvent through the cartridge. The sample is then loaded into the cartridge, followed by washing with a solvent to elute unnecessary interfering matrix while retaining the analytes in the cartridge for further analysis. The

analyte is eluted out of the cartridge with a stronger solvent either by gravity or vacuum suction mechanisms. For solvent with more than one analyte, second elution is necessary but with a stronger solvent [99,104]. For extraction based on polarity, the subsequent eluent will be more polar than the previous ones. In radioactive samples, the activity of the analyte in the eluents are counted using a γ counter. For identification of the analytes, the eluents can be further analyzed by HPLC[105].

Since the separation is based on physical separation, real time separation cannot be observed. Hence, it is not possible to estimate the number of times the cartridge need to be eluted for extraction of all the metabolites. Another limitation of the technique is the loss of analyte on the packing material during filtration process[99]. It is a very fast method and the cartridges (Waters Corporation) are cheap and unbreakable[104]. Depending on the samples analyzed, like HPLC, cartridges with different packing materials are available.

1.4.3 Detection of radioactivity on TLC

TLC contains very minute amount of radioactivity which necessitates the use of a very sensitive detector or technique for characterization. Some of earlier technique is zonal analysis that involves the use of liquid scintillation counting (LSC) method. In this technique, spot on the silica gel or the paper containing the separated analytes are scraped off, mixed with scintillation fluid and the activity measured using LSC. This technique is very time consuming and labor intensive and there is huge probability of losing the analyte[106,107]. Radio-TLC scanner is less labor intensive where 2D chromatographs can be acquired. It has low counting and detection efficiency with 1-7 mm of scanning step, resulting in poor spatial resolution. For determining the small fraction of radio-metabolite containing trace radioactivity, the technique is not a suitable option. The use of autoradiography overcomes the limitations. In this system, the TLC plate is placed directly on X-ray film for counting. Photo-densitometry or scintillation detector converts the counts into a chromatograph as dark spots or regions of different optical density[107]. For weak β-emitter like ^3H, long exposure time of hours or weeks is necessary for good signal intensity[99,106,108]. In addition, the lower limit of detection is very high. Though autoradiography have high resolution it suffers from very poor sensitivity.

In this work, use of a very sensitive detector is required to detect low radioactivity contained in 2µL of plasma on the TLC plate. One such system is the Beaver autoradiography (ai4r, France), mainly used for analyzing tissue and plant samples. It is used for analyzing beta and alpha particles by detecting electrons produced by ionization caused by particles emitted from radioactive decay[109]. The system is based on the principle of micro pattern gaseous (Ne + CO_2) detector (MPGD)[110]. It consists of two drift zones alternating with two amplification zone, separated by $5\mu m$ thick nickel micromesh with varying electric field (Fig. 4.1). The first and third zones are drift zones with low electric field (1kV/cm) to guide the electrons into the amplification zone. Due to high electric field of 20-30 kV/cm in the amplification zone, enough kinetic energy is imparted to the electrons to cause ionization by avalanche effect. Since TLC plate is used as cathode and it is comprised of highly insulating material, first drift zone is in contact with the plate to prevent back flux of electrons. The electron clouds exiting the second amplification zone are captured by the pixelated reading anode. The small thickness of amplification zone ensures that the avalanche electron clouds are narrow and hence excellent spatial resolution. The system has very high sensitivity of $5x10^{-4}$ cpm/mm^2 and spatial resolution of 50 µm (for high energy beta and beta plus particle)[111] and 30µm as measured by ^{3}H (low energy beta particle)[110].

1.5   Research goal and objectives

The main goal of the thesis is to improve the accuracy of kinetic model's parameter estimation and apply them in clinical cancer patient data. The objectives were accomplished in three stages:

1. The first objective is to develop a generic model for dynamic PET by incorporating the finite transit time of the tracer from the arterial end to venous end into the standard compartment model which suffers from non-physiological assumption of instantaneous arrival and washout of tracer in the blood vessel. The study utilized simulation to estimate the accuracy of kinetic parameters using the developed model and the currently used standard compartment model.

2. The second objective is to demonstrate that our developed model can be applied to real clinical patient data that was scanned with dynamic PET. The estimated parameters were compared with parameters estimated with standard compartment model and the estimated parameters were utilized in differentiating tumors from normal tissues. Furthermore, the reversibility of tracer binding was established using model independent graphical analysis method.

3. The third objective is to correct for radio-metabolite in the blood plasma. Most tracers introduced in the body will get metabolized into other radioactive products of different identity that can introduce errors in kinetic parameter estimation.

1.6   Thesis outline

1.6.1 Estimation of kinetic parameters for dynamic PET imaging: A simulation study

Kinetic parameters estimated by the developed F2TC and S2TC model were compared. Mean fractional Euclidean distance (FED) averaged all simulated parameter sets was used as a measure of accuracy. Mean FED is a measure of bias between the estimated and simulated parameter values. The accuracy is compared across factors that could affect the parameter estimation - acquisition time, noise level, mean transit time and different models (F2TC and S2TC). S2TC model is executed with two different software: our custom MATLAB version and a commercially available software called PMOD. Distribution volume estimated with the models were also compared with those estimated from graphical analysis method. The paper will be submitted under the title – *Estimation of Kinetic Parameters for Dynamic PET Imaging: A Simulation Study*.

1.6.2 Pharmacokinetic analysis of dynamic [^{18}F]FAZA PET imaging in pancreatic cancer patient

The kinetics behind the binding of [^{18}F]FAZA in hypoxic pancreatic adenocarcinoma tumor were investigated with both S2TCM and F2TCM. Model independent graphical

analysis model was utilized in estimating the reversibility of tracer binding. The DV from F2TC model was compared with DV from graphical method. Furthermore, the estimated kinetic parameters from both F2TCM and S2TCM was utilized in distinguishing the hypoxic tumor from normoxia tissues. The paper will be submitted under the title – *Pharmacokinetic Analysis of Dynamic [¹⁸F]FAZA PET Imaging in Pancreatic Cancer Patient.*

1.6.3 Plasma radio-metabolite analysis of PET tracers for dynamic PET imaging: TLC and autoradiography

Metabolites in the normal animals' blood plasma (pig and rat) were separated with thin layer chromatography (TLC). The low activity of the blood analyte or radio-metabolites were detected using Beaver autoradiography. The fraction of unmodified tracers were analyzed for [¹⁸F]FEPPA and [¹⁸F]FAZA, an inflammatory and hypoxia marker respectively. Simulation study was done on 10 parameter sets to estimation the error introduced if radio-metabolite is not corrected in the blood plasma during kinetic analysis of dynamic PET. The paper will be submitted under the title – *Radio-metabolite Analysis of PET Tracers in Plasma for Dynamic PET Imaging: TLC and Autoradiography*

1.7   References:

1.   Lee TC, Alessio A, Miyaoka R, Kinahan P. Morphology supporting function: attenuation correction for SPECT/CT, PET/CT, and PET/MR imaging. *Q J Nucl Med Mol Imaging*. 2016;60(1):25-39. doi:10.1016/j.physbeh.2017.03.040

2.   Cherry S, Dahlbom M. PET: Physics, instrumentation, and scanners. In: Phelps M, ed. *PET*. Springer-Verlag, New York; 2006:1-117. doi:10.1007/0-387-34946-4

3.   Raylman RR, Caraher JM, Hutchins GD. Sampling requirements for dynamic cardiac PET studies using image-derived input functions. *J Nucl Med*. 1993;34(3):440-447.

4.   Strother SC, Casey ME, Hoffman EJ. Measuring PET Scanner Sensitivity: Relating Countrates to Image Signal-to-Noise Ratios using Noise Equivalent Counts. *IEEE Trans Nucl Sci*. 1990;37(2):783-788. doi:10.1109/23.106715

5.   Warburg O. The metabolism of carcinoma cells. *J Cancer Res*. 1925;9(1):148-163. doi:10.1158/jcr.1925.148

6. Mees G, Dierckx R, Vangestel C. Molecular imaging of hypoxia with radiolabelled agents. *Eur J Nucl Med Mol Imaging*. 2009;36:1674-1686. doi:10.1007/s00259-009-1195-9

7. Zhu A, Lee D, Shim H. Metabolic PET imaging in Cancer Detection and Therapy Response. *Semin Oncol*. 2011;38(1):55-69. doi:10.1053/j.seminoncol.2010.11.012.Metabolic

8. Boellaard R. Standards for PET image acquisition and quantitative data analysis. *J Nucl Med*. 2009;50:11-20. doi:10.2967/jnumed.108.057182

9. Vanderhoek M, Perlman SB, Jeraj R. Impact of different standardized uptake value measures on PET-based quantification of treatment response. *J Nucl Med*. 2013;54(8):1188-1194. doi:10.2967/jnumed.112.113332

10. Huang SC. Anatomy of SUV. *Nucl Med Biol*. 2000;27(7):643-646. doi:10.1016/S0969-8051(00)00155-4

11. Keyes JW. SUV: Standard uptake or silly useless value? *J Nucl Med*. 1995;36(10):1836-1839.

12. Adams MC, Turkington TG, Wilson JM, Wong TZ. A systematic review of the factors affecting accuracy of SUV measurements. *Am J Roentgenol*. 2010;195:310-320. doi:10.2214/AJR.10.4923

13. Vriens D, Visser EP, De Geus-Oei LF, Oyen WJG. Methodological considerations in quantification of oncological FDG PET studies. *Eur J Nucl Med Mol Imaging*. 2010;37(7):1408-1425. doi:10.1007/s00259-009-1306-7

14. Thie JA. Understanding the standardized uptake value, its methods, and implications for usage. *J Nucl Med*. 2004;45(9):1431-1434.

15. Lammertsma AA. Forward to the past: The case for quantitative PET imaging. *J Nucl Med*. 2017;58(7):1019-1024. doi:10.2967/jnumed.116.188029

16. Suzuki K, Nishioka T, Homma A, et al. Value of fluorodeoxyglucose positron emission tomography before radiotherapy for head and neck cancer: Does the standardized uptake value predict treatment outcome? *Jpn J Radiol*. 2009;27(6):237-242. doi:10.1007/s11604-009-0330-7

17. Menda Y, Boles Ponto LL, Dornfeld KJ, et al. Kinetic Analysis of 3'-Deoxy-3'-18F-Fluorothymidine (18F-FLT) in Head and Neck Cancer Patients Before and Early After Initiation of Chemoradiation Therapy. *J Nucl Med*. 2009;50(7):1028-1035. doi:10.2967/jnumed.108.058495

18. Hamberg LM, Hunter GJ, Alpert NM, Choi NC, Babich JW, Fischman AJ. The dose uptake ratio as an index of glucose metabolism: Useful parameter or oversimplification? *J Nucl Med*. 1994;35(8):1308-1312.

19. Brendle C, Kupferschläger J, Nikolaou K, La Fougère C, Gatidis S, Pfannenberg C. Is the standard uptake value (SUV) appropriate for quantification in clinical PET imaging? -

Variability induced by different SUV measurements and varying reconstruction methods. *Eur J Radiol*. 2015;84(1):158-162. doi:10.1016/j.ejrad.2014.10.018

20.   Fletcher JW, Kinahan PE. PET-CT Standardized Uptake Values (SUVs) in Clinical Practice. *Semin Ultrasound CT MR*. 2010;31(6):496-505. doi:10.1053/j.sult.2010.10.001.PET/CT

21.   Hain SF, Curran KM, Beggs AD, Fogelman I, O'Doherty MJ, Maisey MN. FDG-PET as a "metabolic biopsy" tool in thoracic lesions with indeterminate biopsy. *Eur J Nucl Med*. 2001;28(9):1336-1340. doi:10.1007/s002590100563

22.   Greco C, Nehmeh SA, Schöder H, et al. Evaluation of different methods of 18F-FDG-PET target volume delineation in the radiotherapy of head and neck cancer. *Am J Clin Oncol Cancer Clin Trials*. 2008;31(5):439-445. doi:10.1097/COC.0b013e318168ef82

23.   Willemsen ATM, Hoff J van den. Fundamentals of quantitative PET data analysis. *Curr Parmaceutical Des*. 2002;8(16):1513-1526.

24.   Schmidt KC, Turkheimer FE. Kinetic modeling in positron emission tomography. *Q J Nucl Med*. 2002;46(1):70-85. http://tauruspet.med.yale.edu/staff/edm42/chapters/kinetic-modeling-chapter-23-wernick-book.pdf.

25.   Asselin MC, Cunningham VJ, Amano S, Gunn RN, Nahmias C. Parametrically defined cerebral blood vessels as non-invasive blood input functions for brain PET studies. *Phys Med Biol*. 2004;49(6):1033-1054. doi:10.1088/0031-9155/49/6/013

26.   Watabe H, Channing MA, Riddell C, et al. Noninvasive estimation of the aorta input function for measurement of tumor blood flow with [15O]water. *IEEE Trans Med Imaging*. 2001;20(3):164-174. doi:10.1109/42.918468

27.   Morris ED, Endres CJ, Schmidt KC, Christian BT, Muzic Jr RF, Fisher RE. Kinetic modeling in positron emission tomography. In: *Emission Tomography: The Fundamentals of PET and SPECT*. Elsevier Inc.; 2004:499-540. http://tauruspet.med.yale.edu/staff/edm42/chapters/kinetic-modeling-chapter-23-wernick-book.pdf.

28.   Gunn RN, Gunn SR, Cunningham VJ. Positron Emission Tomography Compartmental Models. *J Cereb Blood Flow Metab*. 2001;21(6):635-652. doi:10.1097/00004647-200106000-00002

29.   Bailey DL, Jones T, Spinks TJ. A method for measuring the absolute sensitivity of positron emission tomographic scanner. *Eur J Nucl Med*. 1991;18:374-379.

30.   Lawrence KS St., Lee T-Y. An Adiabatic Approximation to the Tissue Homogeneity Model for Water Exchange in the Brain: II. Experimental Validation. *J Cereb Blood Flow Metab*. 1998;18(12):1378-1385. doi:10.1097/00004647-199812000-00012

31.   Meier P, Zierler KL. On the theory of the indicator-diliution method for measurement of blood flow and volume. *J Applied Physiol*. 1954;6(12):731-744.

32. Gunn RN, Gunn SR, Turkheimer FE, Aston JAD, Cunningham VJ. Positron Emission Tomography Compartmental Models: A Basis Pursuit Strategy for Kinetic Modeling. *J Cereb Blood Flow Metab*. 2002;22(12):1425-1439. doi:10.1097/01.wcb.0000045042.03034.42

33. Patlak CS, Blasberg RG, Fenstermacher JD. Graphical evaluation of blood-to-brain transfer constants from multiple-time uptake data. *J Cereb Blood Flow Metab*. 1983;3(1):1-7. doi:10.1038/jcbfm.1983.1

34. Logan J. Graphical analysis of PET data applied to reversible and irreversible tracers. *Nucl Med Biol*. 2000;27(7):661-670. doi:10.1016/S0969-8051(00)00137-2

35. Innis RB, Cunningham VJ, Delforge J, et al. Consensus nomenclature for in vivo imaging of reversibly binding radioligands. *J Cereb Blood Flow Metab*. 2007;27(9):1533-1539. doi:10.1038/sj.jcbfm.9600493

36. Endo K, Oriuchi N, Higuchi T, et al. PET and PET/CT using 18F-FDG in the diagnosis and management of cancer patients. *Int J Clin Oncol*. 2006;11(4):286-296. doi:10.1007/s10147-006-0595-0

37. Hsieh C, Lee C, Liang J, Yu C, Shyu W. Cycling hypoxia increases U87 glioma cell radioresistance via ROS induced higher and long-term H1F-1 signal transduction activity. *Oncol Rep*. 2010;24:1629-1636.

38. Grimes DR, Warren DR, Warren S. Hypoxia imaging and radiotherapy: Bridging the resolution gap. *Br J Radiol*. 2017;90(1076). doi:10.1259/bjr.20160939

39. Chan N, Koritzinsky M, Zhao H, et al. Chronic hypoxia decreases synthesis of homologous recombination proteins to offset chemoresistance and radioresistance. *Cancer Res*. 2008;68(2):605-614. doi:10.1158/0008-5472.CAN-07-5472

40. Brown JM, Wilson WR. Exploiting tumour hypoxia in cancer treatment. *Nat Rev Cancer*. 2004;4(6):437-447. doi:10.1038/nrc1367

41. Gray L, Conger A, M E, S H, OCA S. The concentration of oxygen dissolved in tissues at the time of irradiaiton as a factor in radiotherapy. *Br J Radiol*. 1953;26(312):638-648. doi:10.1259/0007-1285-26-312-638

42. Ballinger JR. Imaging hypoxia in tumors. *Semin Nucl Med*. 2001;31(4):321-329. doi:10.1053/snuc.2001.26191

43. Challapalli A, Carroll L, Aboagye EO. Molecular mechanisms of hypoxia in cancer. *Clin Transl Imaging*. 2017;5(3):225-253. doi:10.1007/s40336-017-0231-1

44. Vaupel P, Thews O, Hoeckel M. Treatment resistance of solid tumors: Role of hypoxia and anemia. *Med Oncol*. 2001;18(4):243-259. doi:10.1385/MO:18:4:243

45. Teicher BA. Hypoxia and drug resistance. *Cancer Metastasis Rev*. 1994;13(2):139-168. doi:10.1007/BF00689633

46.   Hong B, Kim J, Jeong H, Bok S, Kim Y, Ahn G. Tumor Hypoxia and Reoxygenation : the Yin and Yang for R adiotherapy. *Radiat Oncol J*. 2016;34(4):239-249.

47.   Bushberg JT, Seibert JA, Leidholdt EM, Boone JM. Radiation Biology. In: Mitchell CW, ed. *The Essential Physics of Medical Imaging*. 2nd ed. Lippincott Williams & Wilkins; 2012:751-836.

48.   Shannon AM, Bouchier-Hayes DJ, Condron CM, Toomey D. Tumor hypoxia, chemotherpeutic resistance and hypoxia-related therapies. *Cancer Treat Rev*. 2003;29:297-307.

49.   Doktorova H, Hrabeta J, Khalil MA, Eckschlager T. Hypoxia-induced chemoresistance in cancer cells: The role of not only HIF-1. *Biomed Pap*. 2015;159(2):166-177. doi:10.5507/bp.2015.025

50.   Fukumura D, Jain RK. Tumor microvascular and microvenvironment.pdf. *Microvasc Res*. 2007;74:72-84.

51.   Wang YD, Li SJ, Liao JX. Inhibition of glucose transporter 1 (GLUT1) chemosensitized head and neck cancer cells to cisplatin. *Technol Cancer Res Treat*. 2013;12(6):525-535. doi:10.7785/tcrt.2012.500343

52.   National Cancer Institute (NCI). Cancer Stat Facts: Pancreatic Cancer. NCI website. https://seer.cancer.gov/statfacts/html/pancreas.html. Published 2019. Accessed January 24, 2020.

53.   The American Cancer Society medical and editorial content team. Can Pancreatic Cancer be Found Early? American Cancer Society. https://www.cancer.org/cancer/pancreatic-cancer/detection-diagnosis-staging/detection.html#written_by. Published 2019. Accessed January 28, 2020.

54.   Koong AC, Mehta VK, Quynh T Le, et al. Pancreatic Tumors Show High Levels of Hypoxia. *Int J Radiat Oncol Biol Phys*. 2000;48(4):919-922.

55.   Daniel SK, Sullivan KM, Labadie KP, Pillarisetty VG. Hypoxia as a barrier to immunotherapy in pancreatic adenocarcinoma. *Clin Transl Med*. 2019;8(1). doi:10.1186/s40169-019-0226-9

56.   Traverso LW. Pancreatic cancer: Surgery alone is not sufficient. *Surg Endosc Other Interv Tech*. 2006;20(2 SUPPL.):446-449. doi:10.1007/s00464-006-0052-1

57.   Moertel C, Childs Jr. D, Reitemeier R, Colby Jr. M, Holbrook M. Combined 5-fluorouracil and Supervoltage Radiation Therapy of Locally Unresectable Gastrointestinal Cancer. *Lancet*. 1969;294(7626):865-867. doi:10.1016/s0140-6736(69)92326-5

58.   Moertel C, S F, Hahn R, et al. Therapy of locally unresectable pancreatic carcinoma: a randomized comparison of high dose (6000 rads) radiation alone, moderate dose radiation (4000 rads + 5-fluorouracil), and high dose radiation + 5-fluorouracil: The Gastrointestinal Tumor Study Group. *Cancer*. 1981;48(8):1705-1710.

59. Neoptolemos JP, Stocken DD, Friess H, et al. A Randomized Trial of Chemoradiotherapy and Chemotherapy after Resection of Pancreatic Cancer. *N Engl J Med*. 2004;350(12):1200-1210. doi:10.1056/NEJMoa032295

60. Raoof M, Blakely AM, Melstrom LG, et al. Adjuvant chemotherapy versus chemoradiation in high-risk pancreatic adenocarcinoma: A propensity score-matched analysis. *Cancer Med*. 2019;8(13):5881-5890. doi:10.1002/cam4.2491

61. Shen H, Paul S, Breuninger LM, et al. Cellular and in vitro transport of glutathione conjugates by MRP. *Biochemistry*. 1996;35(18):5719-5725. doi:10.1021/bi960098n

62. Deng L, Tatebe S, Lin-Lee Y-C, Ishikawa T, Kuo M. MDR and MRP gene families as cellular determinant factors for resistance to clinical anticancer agents. In: Andersson B, Murray D, eds. *Clinically Relevant Resistance in Cancer Chemotherapy. Cancer Treatment and Research*. Springer, Boston, MA; 2002:49-66.

63. Zhou J, Liu M, Aneja R, Chandra R, Lage H, Joshi HC. Reversal of P-glycoprotein-mediated multidrug resistance in cancer cells by the c-Jun NH2-terminal kinase. *Cancer Res*. 2006;66(1):445-452. doi:10.1158/0008-5472.CAN-05-1779

64. König J, Hartel M, Nies AT, et al. Expression and localization of human multidrug resistance protein (ABCC) family members in pancreatic carcinoma. *Int J Cancer*. 2005;115(3):359-367. doi:10.1002/ijc.20831

65. O'Driscoll L, Walsh N, Larkin A, Ballot J, Ooi WS. MDR1 / P-glycoprotein and MRP-1 Drug Efflux Pumps in Pancreatic Carcinoma. *Anticancer Res*. 2007;27:2115-2120.

66. Chen M, Xue X, Wang F, et al. Expression and promoter methylation analysis of ATP-binding cassette genes in pancreatic cancer. *Oncol Rep*. 2012;27(1):265-269. doi:10.3892/or.2011.1475

67. Vaupel P, Knoop C, Hockel M. Oxygenationof Human Tumors: Evaluation Of Tissue Oxygen Distribution In Breast Cancers By Computerized O2 Tension Measurements. *Cancer Res*. 1991;51(12):3316-3322.

68. Xu Z, Li XF, Zou H, Sun X, Shen B. 18F-Fluoromisonidazole in tumor hypoxia imaging. *Oncotarget*. 2017;8(55):94969-94979. doi:10.18632/oncotarget.21662

69. Fan X, River J, Zamora M, Al-Hallaq H, GS K. Effect of carbogen on tumor oxygenation: combine fluorine-19 and proton MRI measurements. *Int J Radiat Oncol Biol Phys*. 2002;54(4):1202-1209.

70. Baudelet C, Gallez B. How does blood oxygen level-dependent (BOLD) contrast correlate with oxygen partial pressure (pO2) inside tumors? *Magn Reson Med*. 2002;48(6):980-986. doi:10.1002/mrm.10318

71. Krohn KA, Link JM, Mason RP. Molecular imaging of hypoxia. *J Nucl Med*. 2008;49:129S-148S. doi:10.2967/jnumed.110.075663

72.   Sun X, Niu G, Chan N, Shen B, Chen X. Tumor hypoxia imaging. *Mol Imaging Biol*. 2011;13(3):399-410. doi:10.1007/s11307-010-0420-z

73.   Lyng H, Malinen E. Hypoxia in cervical cancer: from biology to imaging. *Clin Transl Imaging*. 2017;5(4):373-388. doi:10.1007/s40336-017-0238-7

74.   Li S jiao, Guo W, Ren G xin, Huang G, Chen T, Song S li. Expression of Glut-1 in primary and recurrent head and neck squamous cell carcinomas, and compared with 2-[18F]fluoro-2-deoxy-D-glucose accumulation in positron emission tomography. *Br J Oral Maxillofac Surg*. 2008;46(3):180-186. doi:10.1016/j.bjoms.2007.11.003

75.   Semenza GL. Hypoxia, clonal selection, and the role of HIF-1 in tumor progression. *Crit Rev Biochem Mol Biol*. 2000;35(2):71-103. doi:10.1080/10409230091169186

76.   Christian N, Deheneffe S, Bol A, et al. Is 18F-FDG a surrogate tracer to measure tumor hypoxia? Comparison with the hypoxic tracer 14C-EF3 in animal tumor models. *2Radiotherapy Oncol*. 2010;97:183-188.

77.   Lopci E, Grassi I, Chiti A, et al. PET radiopharmaceuticals for imaging of tumor hypoxia: a review of the evidence. *Am J Nucl Med Mol Imaging*. 2014;4(4):365-384. doi:10.1038/bjc.2014.610

78.   Nunn A, Linder K, Strauss HW. Nitroimidazoles and imaging hypoxia. *Eur J Nucl Med*. 1995;22(3):265-280. doi:10.1007/BF01081524

79.   Shi K, Souvatzoglou M, Astner ST, et al. Quantitative assessment of hypoxia kinetic models by a cross-study of dynamic 18F-FAZA and 15O-H2O in patients with head and neck tumors. *J Nucl Med*. 2010;51(9):1386-1394. doi:10.2967/jnumed.109.074336

80.   Oliveira IM De, Bonatto D, Antonio J, Henriques P. Nitroreductases : Enzymes with Environmental , Biotechnological and Clinical Importance. *Curr Res Technol Educ Top Appl Microbiol Microb Biotechnol*. 2010:1008-1019.

81.   Casciari J, Graham M, Rasey J. A modeling approach for quantifying tumor hypoxia with [F-18]fluoromisonidazole PET time-activity data. *Med Phys*. 1995;22(7):1127-1139.

82.   Bekaert L, Valable S, Lechapt-Zalcman E, et al. [18F]-FMISO PET study of hypoxia in gliomas before surgery: correlation with molecular markers of hypoxia and angiogenesis. *Eur J Nucl Med Mol Imaging*. 2017;44(8):1383-1392. doi:10.1007/s00259-017-3677-5

83.   Bandurska-Luque A, Löck S, Haase R, et al. FMISO-PET-based lymph node hypoxia adds to the prognostic value of tumor only hypoxia in HNSCC patients. *Radiother Oncol*. 2019;130:97-103. doi:10.1016/j.radonc.2018.09.008

84.   Asano A, Ueda S, Kuji I, et al. Intracellular hypoxia measured by 18F-fluoromisonidazole positron emission tomography has prognostic impact in patients with estrogen receptor-positive breast cancer. *Breast Cancer Res*. 2018;20(1):1-8. doi:10.1186/s13058-018-0970-6

85. Gagel B, Reinartz P, DiMartino E, et al. pO2 polarography versus positron emission tomography ([18F] fluoromisonidazole, [18F]-2-fluoro-2'- deoxyglucose): An appraisal of radiotherapeutically relevant hypoxia. *Strahlentherapie und Onkol*. 2004;180(10):616-622. doi:10.1007/s00066-004-1229-y

86. Yamamoto Y, Maeda Y, Kawai N, et al. Hypoxia assessed by 18F-fluoromisonidazole positron emission tomography in newly diagnosed gliomas. *Nucl Med Commun*. 2012;33(6):621-625. doi:10.1097/MNM.0b013e3283529984

87. Peeters SGJA, Zegers CML, Lieuwes NG, et al. A comparative study of the hypoxia PET tracers [18F]HX4, [18F]FAZA, and [18F]FMISO in a preclinical tumor model. *Int J Radiat Oncol Biol Phys*. 2015;91(2):351-359. doi:10.1016/j.ijrobp.2014.09.045

88. Piert M, Machulla HJ, Picchio M, et al. Hypoxia-specific tumor imaging with 18F-fluoroazomycin arabinoside. *J Nucl Med*. 2005;46(1):106-113.

89. Beck R, Röper B, Carlsen JM, et al. Pretreatment 18F-FAZA PET predicts success of hypoxia-directed radiochemotherapy using tirapazamine. *J Nucl Med*. 2007;48(6):973-980.

90. Pike VW. PET Radiotracers: crossing the blood-brain barrier and surviving metabolism. 2009;30(8):431-440. doi:10.1016/j.tips.2009.05.005.PET

91. Masaki Y, Shimizu Y, Yoshioka T, et al. Imaging mass spectrometry revealed the accumulation characteristics of the 2-nitroimidazole-based agent "pimonidazole" in hypoxia. *PLoS One*. 2016;11(8):1-11. doi:10.1371/journal.pone.0161639

92. Masaki Y, Shimizu Y, Yoshioka T, et al. FMISO accumulation in tumor is dependent on glutathione conjugation capacity in addition to hypoxic state. *Ann Nucl Med*. 2017;31(8):596-604. doi:10.1007/s12149-017-1189-9

93. Pawelke B. Metabolite analysis in positron emission tomography studies: Examples from food sciences. *Amino Acids*. 2005;29(4 SPEC. ISS.):377-388. doi:10.1007/s00726-005-0202-0

94. Veronese M, Gunn RN, Zamuner S, Bertoldo A. A non-linear mixed effect modelling approach for metabolite correction of the arterial input function in PET studies. *Neuroimage*. 2013;66:611-622. doi:10.1016/j.neuroimage.2012.10.048

95. Rusjan PM, Wilson AA, Bloomfield PM, et al. Quantitation of translocator protein binding in human brain with the novel radioligand 18 F-FEPPA and positron emission tomography. *J Cereb Blood Flow Metab*. 2011;31(8):1807-1816. doi:10.1038/jcbfm.2011.55

96. Huang S-C, Yu D-C, Barrio JR, et al. Kinetics and modeling of L-6-[18F]fluoro-DOPA in human positron emission tomographic studies. *J Cereb Blood Flow Metab*. 1991;11(6):898-913. doi:10.1038/jcbfm.1991.155

97. Tomasi G, Kimberley S, Rosso L, Aboagye E, Turkheimer F. Double-input compartmental

modeling and spectral analysis for the quantification of positron emission tomography data in oncology. *Phys Med Biol*. 2012;57(7):1889-1906. doi:10.1088/0031-9155/57/7/1889

98. Mankoff DA, Shields AF, Graham MM, Link JM, Eary JF, Krohn KA. Kinetic analysis of 2-[carbon-11]thymidine PET imaging studies: Compartmental model and mathematical analysis. *J Nucl Med*. 1998;39(6):1043-1055.

99. Robards K, Haddad PR, Jackson PE. *Principles and Practice of Modern Chromatographic Methods*. Academic Press; 1994.

100. Scott RP. Mechanism of solute retention in chromatography. In: Brown P r, ed. *High Performance Liquid Chromatogrpahy*. John Wiley & Sons, Inc.; 1988:117-144.

101. Wilson ID. Thin-layer chromatography: A neglected technique. *Ther Drug Monit*. 1996;18(4):484-492. doi:10.1097/00007691-199608000-00030

102. Cheng SC, Huang MZ, Shiea J. Thin layer chromatography/mass spectrometry. *J Chromatogr A*. 2011;1218(19):2700-2711. doi:10.1016/j.chroma.2011.01.077

103. Waters. How does high performance liquid chromatography work? https://www.waters.com/waters/en_US/How-Does-High-Performance-Liquid-Chromatography-Work%3F/nav.htm?locale=en_US&cid=10049055. Accessed January 27, 2020.

104. McDonald PD. A sample preparation primer and guide to solid phase extraction methods development. In: McDonald PD, Bouvier ES., eds. *Solid Phase Extraction Applications Guide and Bibliography: A Resource for Sample Preparation Methods Development*. 6th ed. Waters Corporation; 1995.

105. Hennion M-C. Solid-phase extraction: method development, sorbents, and coupling with liquid chromatography. *J Chromatogr A*. 1999;856:3-54.

106. Marx AM, Kronberg H, Neuhoff V. Determination of the specific radioactivity of amino acids by a combination of thin-layer chromatography and quantitative autoradiography. *J Chromatogr*. 1987;393(19):407-417. doi:10.1017/CBO9781107415324.004

107. Clark T. Radioactivity Detection. In: *Encyclopedia of Separation Science*. Academic Press; 2000:899-906.

108. Roberts T. Radio-thin layer chromatography. In: *Radiochromatography: The Chromatography and Electrophoresis Radiolabelled Compounds*. Elsevier Inc.; 1978:45-81.

109. Sardini P, Angileri A, Descostes M, et al. Quantitative autoradiography of alpha particle emission in geo-materials using the Beaver[TM] system. *Nucl Instruments Methods Phys Res Sect A Accel Spectrometers, Detect Assoc Equip*. 2016;833:15-22. doi:10.1016/j.nima.2016.07.003

110. Donnard J, Arlicot N, Berny R, et al. Advancements of labelled radio-pharmaceutics imaging with the PIM-MPGD. *J Instrum*. 2009;4(11):1-9. doi:10.1088/1748-0221/4/11/P11022

111. Ai4r. BeaQuant. http://www.ai4r.com/real-time-autoradiography/product/. Published 2017. Accessed January 31, 2020.

Chapter 2

2 Estimation of kinetic parameters for dynamic PET imaging: A simulation study

2.1 Introduction

Positron Emission Tomography (PET) imaging with targeted probes can provide metabolic, physiologic and molecular information about diseases and their treatment responses. It also holds great promise for quantitative imaging, in particular kinetics modelling, however this capability is not fully utilized for different reasons. Currently, clinical PET is quantified using standardized uptake value (SUV). It is a measure of tracer uptake in the tissue normalized by the amount of tracer injected and the body weight derived from an image acquired at a single time point after administration of the targeted probe. Comparing SUV measured at follow-up to baseline is accepted as a quantitative measure of treatment response[1]. While SUV is simple to use and provides reproducible quantitative assessment rather than subjective visual interpretation of PET images, it is an imperfect surrogate measure of target concentration/activity. Therefore, the diagnostic accuracy of SUV is dependent on the properties of the tracer used, for example, fast vs slow blood clearance, and the particular clinical/research question under investigation[2–4]. SUV also varies with the time at which it is measured post administration of the tracer. To optimize SUV contrast between target and background tissue would require detailed knowledge of the kinetics of tracer, for example, irreversible vs reversible binding, rate of binding vs dissociation from target and these rates relative to the bidirectional rates of tracer permeation of the blood-tissue barrier[5,6]. These kinetic properties could vary between patients making optimal SUV measurement for individual patients difficult.

Tissue uptake of targeted tracer is governed by three processes - perfusion delivery, bidirectional permeation of the blood-tissue barrier during the finite transit time of the blood vessels, interaction with (i.e. binding to and dissociation from) target. SUV measured at any time post injection is the balance of these three processes. As each of the uptake processes requires at least two parameters to describe (see §2.1 below), it is clear a single

image (i.e. SUV) is unable to characterize all three processes. This is the motivation for dynamic PET wherein images at multiple time points post injection are acquired in order to estimate the three uptake processes. For targeted tracers, the kinetic parameters of interest include: the rate constants of binding to and dissociation from target as well as the distribution volume (*DV*). The rate constants provide a measure of target concentration/activity and the reversibility of the binding to the target while *DV* can be regarded as the theoretical background subtracted SUV when the different processes involved (as discussed above) in the uptake of the probe are in 'dynamic' equilibrium and is therefore a summary measure of both the bidirectional permeation of the blood-tissue barrier as well as the binding and dissociation of the targeted probe.

One frequently used method to analyze dynamic PET is kinetic modelling wherein a model of the tracer uptake processes is used to replicate the tissue uptake vs time or time-activity curve (TAC) measured by dynamic PET. Compartment models, in particular, the standard two tissue compartment (S2TC) model with the implicit blood compartment, have been widely used to analyze dynamic PET studies of targeted tracers. The first tissue compartment comprises the free (unbound) tracer in the extravascular extracellular space (EES) from the bidirectional permeation of the blood – tissue barrier while the second tissue compartment the bound tracer in EES and/or cells. However, modelling blood vessels as a well-mixed compartment does not accurately describe the delivery and accumulation of the free tracer in the first tissue compartment, hence would affect the estimation of the kinetics between the first and second compartment, that is, the binding and dissociation of the tracer from its target. We have developed the flow modified two tissue compartment (F2TC) model which models the flow of tracer in blood vessels as well as the bidirectional permeation of the endothelial barrier between blood vessels and tissue during the finite transit time through these vessels, in addition to modelling the free and bound tracer in the tissue as two compartments as in the S2TC model. In this simulation study, we compared S2TC to F2TC model to investigate the effect of noise, blood vessel transit time and permeation, and time duration of the dynamic PET study on model parameter estimation.

Figure 2-1: Compartment models for dynamic PET
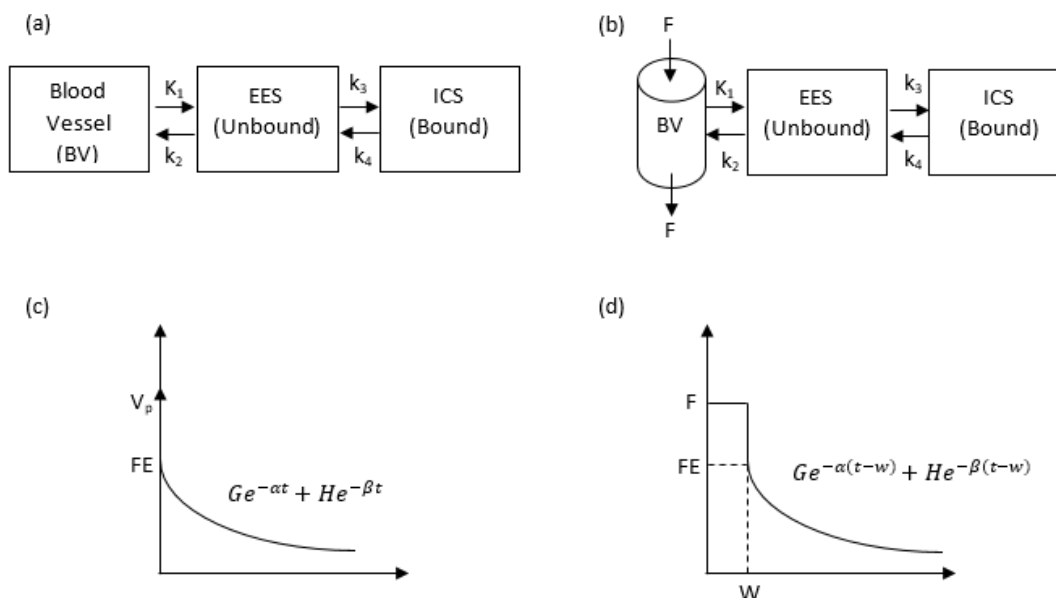
Compartment models used in the simulation with its corresponding $\mathbf{IRF_F(t)}$ (c and d). (a) Standard two tissue compartment (S2TC) model with delta function in the $\mathbf{IRF_F(t)}$ showing the instantaneous arrival of tracer in blood vessel and extraction of tracer into the extravascular extracellular space (EES) (c); and (b) our developed flow modified two tissue compartment (F2TC) model where the blood flow effect in the $\mathbf{IRF_F(t)}$ is represented as a rectangular function to model the extraction of tracer into EES over the transit time of vessels (d). ICS is the intracellular space

Besides kinetic modeling, graphical analysis (GA) methods, namely Patlak and Logan[7–9], have also been developed to analyze dynamic PET data. GA methods were formulated using compartments but without specifying a particular model structure (as in S2TC model) except for the presence or absence of irreversible or reversible binding to a bound compartment with the Patlak and Logan method respectively. Nevertheless, because GA methods do not account for

bidirectional permeation of the blood-tissue barrier during the finite transit time of the blood vessels, we will also investigate whether distribution volume (DV) estimated with the Logan method could be different from that estimated with the F2TC model.

2.2   Methods

2.2.1   Kinetics Modeling of Tissue TAC

If the tracer uptake processes are time invariant during the duration of the dynamic PET study and PET scanner response (signal) is linear with tracer concentration, then by the principle of linear superimposition, the tissue TAC can be modeled as

$$Q(t) = C_p(t) \otimes IRF_F(t) \text{ ... ... } (1)$$

where $\otimes$ is the convolution operator, $C_p(t)$ is the arterial TAC and $IRF_F(t)$ is the flow scaled impulse residue function. $IRF_F(t)$ is the idealized tissue TAC in response to an arterial TAC of the form $F \cdot \delta(t)$ where F is blood flow and $\delta(t)$ is the Dirac delta function. Depending on the kinetic model used, $IRF_F(t)$ incorporates all or some of the three tracer uptake processes - perfusion delivery, bidirectional permeation of the blood-tissue barrier, interaction with (i.e. binding to and dissociation from) the target. When the arterial TAC is measured at a site upstream to the tissue, equation (1) can be modified to account for the time delay, T_o between the tracer arrival at the artery and tissue as follows:

$$Q(t) = C_p(t) \otimes IRF_F(t - T_o) \text{ ... ... } (1b)$$

2.2.2 IRF_F for Standard Two-tissue Compartment (S2TC) Model

S2TC model is the most commonly used compartment model for targeted tracer where blood vessels are assumed to be a compartment (figure 2.1). Free (unbound) tracer from the bidirectional permeation of the blood-tissue barrier accumulates in the first tissue compartment, also called the extravascular extracellular space. The forward transfer (influx) of tracer from blood to EES is governed by the rate constant, K_1, while the efflux of tracer from EES to blood by the rate constant k_2. Tracer bound to target constitutes the second tissue compartment with k_3 describing the rate constant of target binding of free (unbound) tracer in EES and k_4 the dissociation rate constant of the bound tracer back to free tracer in EES. The compartmental assumption for blood vessel neglects the finite transit time with each circulation of the tracer through the tissue and assumes all blood

vessels are filled with tracer at the arterial concentration and leaks into EES instantaneously. In reality, during this transit the tracer influx into the EES is not the product of K_1 and the arterial concentration as is implicitly assumed in the compartmental assumption but has to take into account the spatial gradient of tracer concentration along the blood vessels. This would lead to error in the estimation of tracer concentration in the EES and consequently error in estimation of K_1 and $k_i, i = 2,3,4$. Because of the compartment assumption for blood vessels, the IRF_F of the S2TC model consists of a delta function of magnitude V_p, the blood volume at time zero for the vascular phase. Besides the vascular component delta function, the extravascular component (phase) of the S2TC model IRF_F comprises of a sum of two decaying exponentials to describe the binding to and dissociation from the target and washout of the tracer once it has been extracted into the first tissue compartment (i.e. EES). Taking the above considerations together, the S2TC model IRF_F (figure 2.1(c)) can be written as in equation (2):

$$IRF_F(t) = \begin{cases} V_p\delta(t) & t = 0 \\ Ge^{-\alpha t} + He^{-\beta t} & t > 0 \end{cases} \quad \ldots\ldots\ldots (2)$$

where

$$\alpha, \beta = \frac{k_2 + k_3 + k_4 \pm \sqrt{(k_2 + k_3 + k_4)^2 - 4k_2 k_4}}{2} \quad \ldots\ldots\ldots (3)$$

$$G = \frac{K_1(\alpha - k_3 - k_4)}{\alpha - \beta}; H = \frac{K_1(k_3 + k_4 - \beta)}{\alpha - \beta} \quad \ldots\ldots\ldots (4)$$

Equations (2-4) show that the S2TC model IRF_F is characterized by the following parameters: V_p (blood volume), K_1 and k_2 (bidirectional permeation of the blood-tissue barrier) and k_3 and k_4 (binding to and dissociation from target). As expected, blood flow and vascular mean transit time that characterize perfusion delivery are not included in the IRF_F. Instead, an amount of tracer equal to the initial value ($t = 0$) of the extravascular component or $G + H = K_1$ is assumed to be instantaneously deposited in the EES as soon as the tracer arrives at the vessels. Kinetic analysis of dynamic PET based on the S2TC

model makes use of equations (1b) and (2) to find the best fit to the measured tissue TAC by iteratively adjusting the fitting parameters G, H, α, β, V_p and T_o. Equations (5 & 6) can then be used to determine K_1 and $k_i, i = 2,3,4$ in terms of G, H, α and β as follows:

$$K_1 = G + H; \quad k_2 = \frac{G\alpha + H\beta}{G + H} \tag{5}$$

$$k_3 = \frac{GH(\alpha - \beta)^2}{(G + H)(G\alpha + H\beta)}; \quad k_4 = \frac{(G + H)\alpha\beta}{(G\alpha + H\beta)} = \frac{\alpha\beta}{k_2} \tag{6}$$

DV of the tracer defined as the ratio of (average) tracer concentration in the two tissue compartments (i.e. the EES and the bound compartment) to the blood concentration at kinetic (distribution) equilibrium can be calculated from the explicit model parameters as:

$$DV = \frac{K_1}{k_2}\left(1 + \frac{k_3}{k_4}\right) \tag{7}$$

It follows *DV* can be viewed as the blood background corrected 'equilibrium' SUV without having to perform the static imaging at the time of distribution equilibrium which can have inter- and intra-patient heterogeneity and may require waiting a long time after injection of the tracer. Total *DV*, V_T, is the sum of *DV* and V_p. Besides *DV*, there are two other summary kinetic parameters of interest. Binding potential (*BP*), defined as the concentration ratio of bound to free/unbound tracer at kinetic equilibrium [10,11], and the net influx rate of tracer from blood to tissue indicated by K_i :

$$BP = \frac{k_3}{k_4}; \quad K_i = \frac{k_1 k_3}{k_2 + k_3 + k_4} \tag{8}$$

2.2.3 IRF_F for Flow Modified Two-tissue Compartment (F2TC) Model

We propose the F2TC model as a hybrid of the Johnson-Wilson-Lee model [12] and the S2TC model. The Johnson-Wilson-Lee (JWL) model is used to describe the perfusion delivery of the tracer and the bidirectional permeation of the endothelial barrier during the transit

time of the blood vessels while the S2TC model is used to describe the binding to and dissociation from the target and washout of the tracer in the first tissue compartment (i.e. EES). By combining the IRF_F for the JWL and S2TC model we arrive at the IRF_F for our proposed F2TC model (figure 2.1d), expressed as:

$$IRF_F(t) = \begin{cases} F & 0 \le t < W \\ Ge^{-\alpha(t-W)} + He^{-\beta(t-W)} & t \ge W \end{cases} \quad \text{...... ... (9)}$$

where G, H, α and β are related to K_1 and $k_i, i = 2,3,4$ as defined for the S2TC model and equations (3-6), F is blood flow and W is the transit time through blood vessels. JWL model assumes plug flow in blood vessels, so W is also the vascular mean transit time (MTT). As shown in equation (9), IRF_F for the F2TC model is comprised of two periods: vascular transit period when the tracer is either in the blood vessels, EES or bound compartment and washout period beyond MTT. Because of conservation of mass, IRF_F is a rectangular function equal to F during the vascular transit period. One important result from the JWL model is that in each circulation of the tracer through the tissue, during the transit time of the vessels, the amount of tracer extracted into the EES is equal to the flow (F) extraction fraction (E) product and E is given by $1 - e^{-\frac{PS}{F}}$ where PS is the permeability and (perfused) surface area product of blood vessels as first discussed by Crone [5]. Therefore, $G + H$ or K_1 is equal to FE. Instead, in the S2TC model, the extraction of the tracer is instantaneous as soon as the tracer arrives. Note also that by the Central Volume Principle[13], blood volume (V_p) is equal to $F * W$.

Equations (3-4 & 9) show that the F2TC model IRF_F is characterized by the following parameters: F and W (perfusion delivery of tracer), K_1 and k_2 (bidirectional permeation of the blood-tissue barrier) and k_3 and k_4 (binding to and dissociation from target). Kinetic analysis of dynamic PET based on the F2TC model makes use of equations (1b) and (9) to find the best fit to the measured tissue TAC by adjusting the fitting parameters $G, H, \alpha, \beta, F, W$ and T_o. Equations (5 & 6) can then be used to determine the explicit model parameters K_1 and $k_i, i = 2,3,4$ in terms of G, H, α and β as before and equations (7 & 8) for DV, BP and K_i.

2.2.4　　Simulation Experiments

As the F2TC model is more realistic (as discussed in §2.3) in describing the tracer kinetics, the simulated tissue TACs were generated with the F2TC model for the following simulation experiments.

2.2.4.1　　Noise Behavior of the S2TC and F2TC Model

Simulated tissue TACs were generated using ten set of parameters (table 2.1) obtained from patients with high grade glioma scanned with [^{18}F]fluoro-ethyl-tyrosine ([^{18}F]FET) PET[14]. F, T_0 and W values were selected to cover the range of values seen in CT Perfusion studies of stroke and tumor studies in our lab. The IRF_F of each parameter set is convolved with a simulated arterial TAC (figure 2.2) given by equation (10)[15,16]:

$$C_p(t) = [A_1(t - t_0)^\alpha - A_2 - A_3]e^{-\lambda_1(t-t_0)} + A_2 e^{-\lambda_2(t-t_0)} + A_3 e^{-\lambda_3(t-t_0)} \ldots\ldots\ldots. (10)$$

where $A_1 = 800, \alpha = 1.0,\ A_2 = 20,\ A_3 = 20,\ \lambda_1 = 4\ min^{-1}, \lambda_2 = 0.015\ min^{-1}, \lambda_3 = 0.15\ min^{-1}, t_0 = 0.15\ min$, to generate ten simulated tissue TAC. The simulated tissue TAC for parameter set #1 is shown in figure 2.2.

Both simulated arterial and tissue TAC were generated at 0.5 s intervals initially and then averaged according to the following framing schedule to simulate a 22 min dynamic PET protocol – 10 @ 10 s, 5 @ 20 s, 4 @ 40 s, 4 @ 60 s, 4 @ 180 s. The average values were placed at the mid-point of each framing interval to give the averaged arterial and tissue TAC, $C_{p,av}(t)$ and $Q_{av}(t)$ respectively. For simulations where longer acquisition times were used (see §2.4.2), the number of frames of 180 s was increased until it reached the specified time of 45 and 60 min.

Following frame averaging, Poisson noise was introduced into the averaged tissue TAC, $Q_{av}(t)$ according to Logan's random PET noise model[17]:

$$\widetilde{Q_{av}}(t) = Q_{av}(t) + e^{\lambda t}SD(t) \ldots\ldots\ldots (11)$$

$$SD(t) = x.Sc \sqrt{\frac{e^{-\lambda t}Q_{av}(t)}{\Delta t}} \dots\dots\dots (12)$$

where λ is the decay constant of the PET radionuclide, $\widetilde{Q_{av}}(t)$ is the noisy averaged tissue TAC, $e^{-\lambda t}Q_{av}(t)$ is the decayed $Q_{av}(t)$, and $e^{\lambda t}SD(t)$ is noise contribution at time t, x is a random number from a zero mean Gaussian distribution with variance of one, Sc is noise scaling factor and Δt is the frame duration. Logan used Sc that ranged from 0.25 to 8. In this simulation study, Sc was set at either 1 or 5 to represent low and high noise respectively. For each of the ten simulated tissue TACs, fifty noisy curves were simulated.

Table 2.1: Ten set of parameters used for simulating tissue time activity curve (TAC)

SET#	F (mL·min⁻¹·g⁻¹)	W (s)	K_1 (mL·min⁻¹·g⁻¹)	k_2 (min⁻¹)	k_3 (min⁻¹)	k_4 (min⁻¹)	V_p (mL·g⁻¹)	DV (mL.g⁻¹)
1	0.37	7	0.0930	0.5920	0.1840	0.0410	0.043	0.8621
2	0.27	7	0.1370	0.3310	0.2300	0.0700	0.032	1.7738
3	0.10	10	0.0740	0.3440	0.1520	0.0370	0.016	1.0988
4	0.29	10	0.0720	0.4580	0.2880	0.0770	0.048	0.7452
5	0.44	5	0.2220	0.4720	0.1900	0.0870	0.037	1.4975
6	0.26	15	0.1940	0.3280	0.2830	0.1720	0.065	1.5646
7	0.38	8	0.0960	1.0000	0.3060	0.0670	0.051	0.5344
8	0.20	10	0.1010	0.5180	0.3510	0.0750	0.034	1.1075
9	0.64	10	0.4790	1.0000	0.2210	0.1370	0.106	1.2517
10	0.87	15	0.2180	0.4980	0.4480	0.0840	0.218	2.7724

2.2.4.2 Effect of Dynamic PET Acquisition Time on the Estimation of Model Parameters

Dynamic PET of reversibly bound tracers requires long acquisition time of 60-90 minutes to reach distribution (kinetic) equilibrium. Some studies showed that tracer accumulation was still increasing past 90 min (i.e. equilibrium had not been reached)[18,19]. It is important to investigate how the performance of the two models changes with increased dynamic PET acquisition time from 22 min (used in §2.4.1) to 45 and 60 min. TACs were simulated with the parameters listed in table 2.1 except MTT (W) was set to 20 s for all ten parameter

sets and noise was simulated with a *Sc* of 5. The same fitting software as in §2.4.1 was used to estimate the model parameters.

2.2.4.3   Effect of MTT on the Estimation of Model Parameters

Since the bidirectional permeation of the endothelial barrier in the F2TC model occurs during the MTT of blood vessels whereas this process is assumed to happen instantaneously in the S2TC model, the effect of three different MTTs (5, 10 and 20s) were observed while other parameters remained the same (as in table 2.1). The MTTs were chosen to cover larger range of MTTs observed in the hypoxic and ischemic regions. An acquisition time deemed sufficient from §2.4.2 was used and noise was simulated with *Sc* of 5 in this simulation. The same fitting software as in §2.4.1 was used to estimate the model parameters.

2.2.4.4   Kinetic Parameters Estimation by Different Models/software

As discussed above (§2.2), the compartment assumption for blood vessels in S2TC model can lead to error in the EES tracer concentration and subsequently error in estimation of K_1 and $k_i, i = 2,3,4$ and summary parameters like K_i, *DV* and *BP*. To test for these modelling differences, the estimated parameters using F2TC model were compared with those estimated using S2TC model (with custom software or PMOD) for the 10 parameter sets in table 2.1 for the case of MTT 20s, *Sc* 5 and acquisition time of 45 minutes. To remove the influence of noise but keeping the effect of frame averaging that is ubiquitous in dynamic PET to improve the signal to noise ratio of tissue TAC, the same comparison between F2TC and S2TC model was repeated with noise set to zero (*Sc* =0) while keeping the other factors the same.

2.2.4.5 Numerical Algorithm for the Estimation of Model Parameters

The noisy curves were fitted with both S2TC and F2TC model using software developed by ourselves in MATLAB 2019b (The Mathworks Inc.). Besides the in-house custom software, PMOD (PMOD Technologies LCC.) was also used for fitting with the S2TC model with blood delay estimation. Fitting with either S2TC or F2TC model is a nonlinear optimization problem which requires an initial guess of the model parameters as close to real values as possible to prevent the solution being trapped in local minima. In our in-house program, the initial guess was estimated using spectral analysis[20]. In addition, for robust parameter estimation, sequential search of time delay (T_0) and MTT were implemented. T_0 and W (only for F2TC model) were searched from 0 s to 15 s and 0 s to 25 s respectively at 0.5 s intervals. Within the iterative sequential search for T and W, the rest of the other model parameters – G, H, α, β and V_p (for S2TC model) or F (for F2TC model) were estimated with the non-linear optimization routine *'interior-point'* in MATLAB. Minimum root mean squared deviation (RMSD) between the fitted curve and the simulated curve was used as the measure of the best fitted curve. From the fitting parameters α, G, β and H of the best fitted curve, the explicit model parameters K_1 and $k_i, i = 2,3,4$ can be calculated using equations (5) and (6).

2.2.4.6 Logan Graphical Analysis for Estimation of Distribution Volume

The Logan graphical analysis plots the tissue TAC normalized time integral of the tissue TAC $\left(\int_0^t \widetilde{Q_{av}}(s)ds / \widetilde{Q_{av}}(t) \right)$ vs that of the arterial TAC $\left(\int_0^t C_{p,av}(s)ds / \widetilde{Q_{av}}(t) \right)$, where $C_{p,av}(t)$ is the averaged arterial activity in a dynamic PET image. As discussed by Logan, after some time the plot becomes linear with a slope equal to the V_T[7,8,17]. The Logan plot is usually concave (curving upward) before it becomes linear. Therefore, starting from the origin, the derivative of the Logan plot would increase until it reaches a maximum where the plot becomes linear. The slope of the Logan plot was determined by linear regression of data points from the maximum derivative onwards. V_T estimated with the Logan plot,

F2TC and S2TC (both software) models from TACs of 45 and 60 min duration at a noise *Sc* of 5 and MTT of 20 s were compared with the 'true' (simulated) value by modified Bland-Altman analysis[21] and non-parametric paired test as in §2.4.4.

2.2.4.7   Analysis of the Simulation Experiment Results

The performance of S2TC and F2TC model and the fitting software was evaluated in each simulation experiment using fractional Euclidean distance (*FED*) or root sum of squared fractional deviations of all explicit parameters from the truth, defined as follows:

$$FED = \sqrt{\left(\frac{p_1 - p_{1true}}{p_{1true}}\right)^2 + \left(\frac{p_2 - p_{2true}}{p_{2true}}\right)^2 + \cdots + \left(\frac{p_n - p_{ntrue}}{p_{ntrue}}\right)^2} \qquad (13)$$

where $p_i, i = 1 \ldots p_n$ are the explicit F2TC or S2TC model parameters: $n = 6$; $V_P, K_1, k_i\ i = 2,3,4, T_0$ (*W* and *F* parameter in F2TC model were combined and evaluated as V_p). Results on *FED* of the estimated parameters were displayed either as the average and standard deviation (SD) over 50 noisy simulations for each parameter set or, as average *FED* and within group SD of all parameter sets. In the pairwise comparison of estimated *FED* using different models/software under different conditions described above (§2.4.1-4), non-parametric paired test (Wilcoxon signed rank test or sign test) on the median difference of *FED* between parameter sets was used. Similarly, to test the null hypothesis that the median difference in the parameters estimated by F2TC and S2TC

Figure 2-2: Curves used for simulation experiment
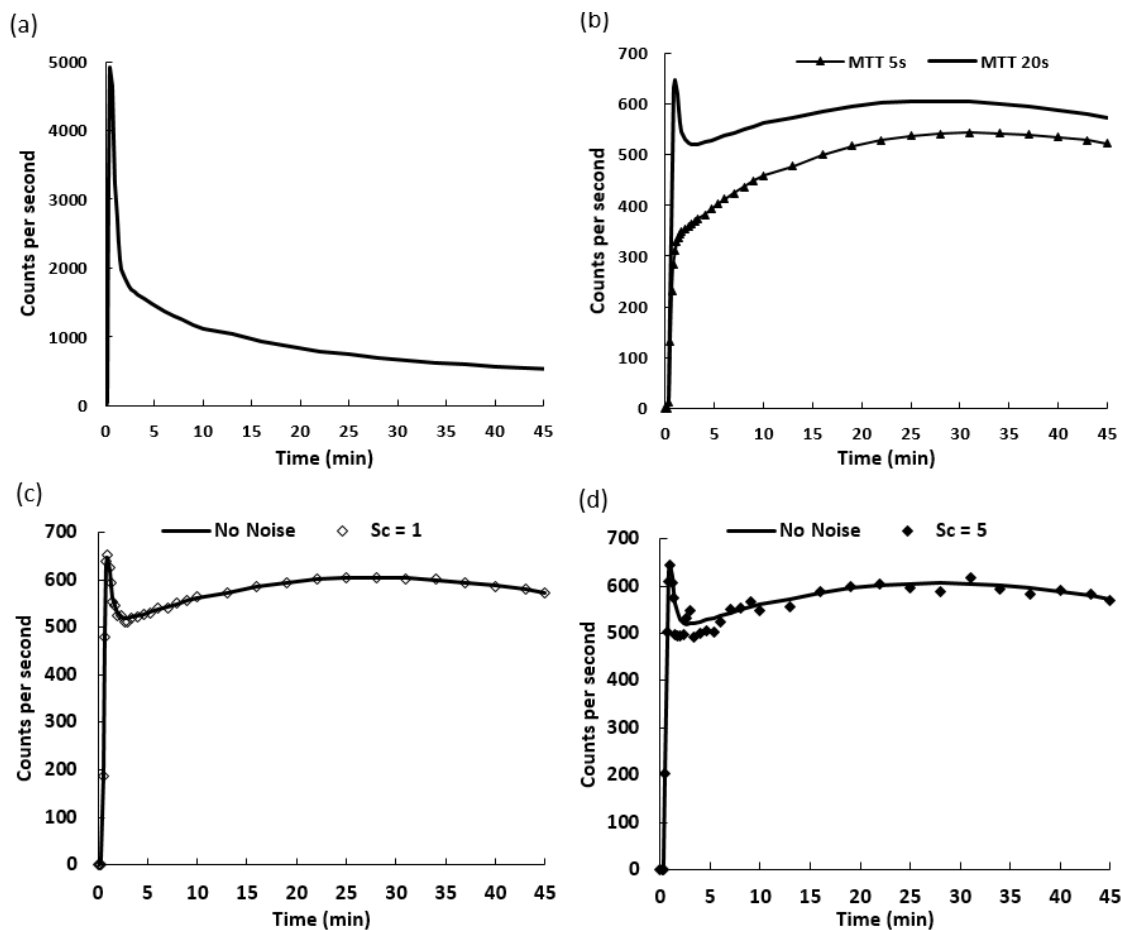
Curves used for simulation. (a) Arterial TAC (b) Tissue TAC for parameter set #1 with MTT of 5 s and 20 s. Simulated tissue TAC with (c) noise scaling factor of 1 and MTT of 20 s and (d) with noise scaling factor of 5 and MTT of 20 s

model (with either custom software or PMOD) was not significantly different from zero. Non-parametric paired test was used with Bonferroni correction for multiple comparisons. Either Wilcoxon signed-rank test or sign test was used based on the distribution of the differences between the groups compared. Unlike Wilcoxon signed test, sign test is not affected by the symmetrical distribution assumption. All statistical analysis was performed with SPSS Statistics for Windows, version 26 (SPSS Inc., Chicago, Ill., USA).

Figure 2-3: Comparison of F2TC and S2TC model at different noise level
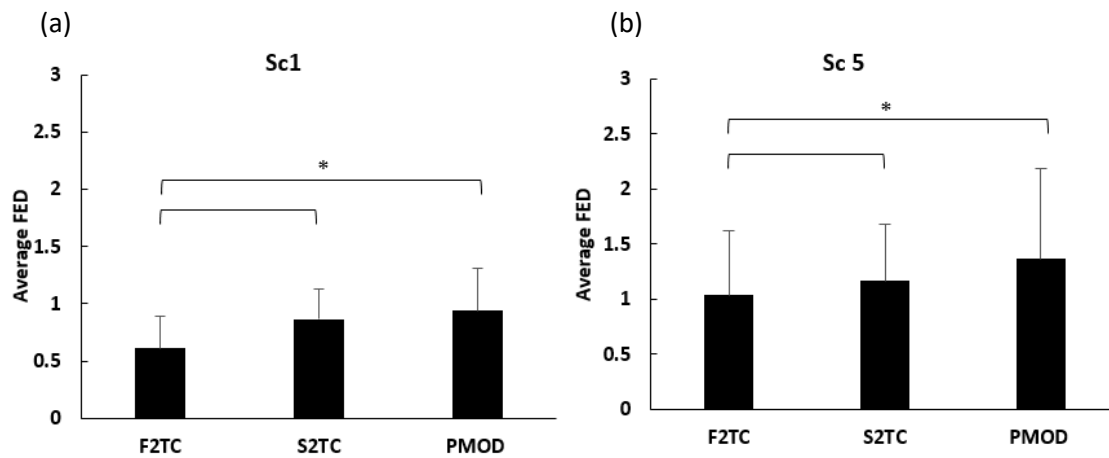
Comparison of F2TC model and S2TC model with custom software and PMOD at different noise level for simulations with parameter sets from Table 2.1. Average *FED* and within group SD as error bar at noise *Sc* of 1 (a) and 5 (b). Data connected by bracket were different with statistical significance indicated by * for P<0.05.

2.3   Results

2.3.1   Simulation Curves

Figure 2.2 shows the simulated arterial TAC used in the simulations along with tissue TACs simulated using the F2TC model. The tissue TACs were generated using parameter set #1 with two different MTTs: 5 and 20 s. Larger value of MTT results in a wider rectangular portion in IRF_F. Since tissue TAC is the convolution of arterial TAC with IRF_F, a longer MTT or vascular transit period would result in a longer time integral of the arterial TAC and hence a higher tissue TAC.

2.3.2   Comparison between F2TC and S2TC Models at Different Noise Level

The average *FED* and the within group SD of the parameter sets are plotted in figure 2.3(a) and figure 2.3(b) for noise *Sc* of 1 and 5 respectively. For both noise levels, based on non-parametric test, median *FED* for F2TC model was statistically lower than S2TC model with

Figure 2-4: Noise effect on F2TC and S2TC model
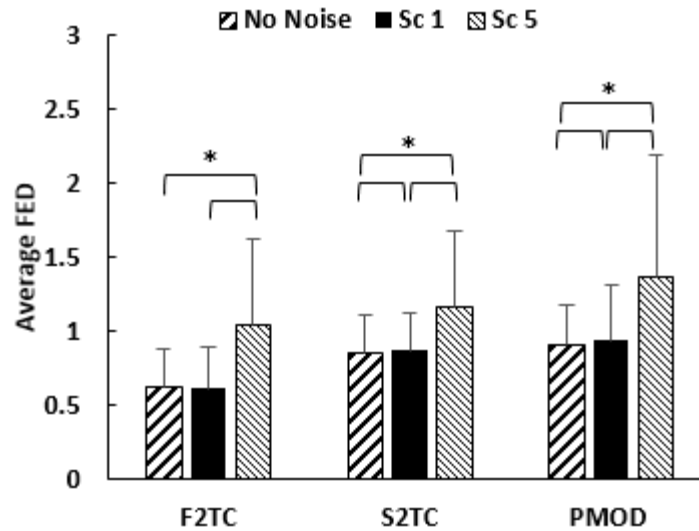
Average *FED* and within group SD as error bar for F2TC model, S2TC model with custom software and PMOD (a) at noise *Sc* of 0 (noiseless), 1, and 5. Data connected by brackets are different with statistical significance indicated by * for P<0.05.

either custom software or PMOD (p<0.0015) and median *FED* for S2TC model was lower with custom software than PMOD (p< 0.0015). As expected, *FED* for Sc = 5 is higher than Sc =1 for all the models/software.

2.3.3   Noise Effect for F2TC and S2TC Models

Figure 2.4 shows the noise effect on the two models and software using average *FED* for all parameter sets and the within parameter set SD as error bar. For all models and software, based on the non-parametric paired comparison (either Wilcoxon signed rank or signed test, see §2.7), *FED* was statistically different between all noise levels (p<0.05) with Bonferroni correction for multiple comparisons (N=3 in this case). Largest average *FED* was observed for *Sc* 5 for both models/software. Though significant, the average *FED* for noiseless and *Sc* 1 were very close to each other with largest average *FED* difference of 0.04 observed in custom S2TC software.

Figure 2-5: Effect of time acquisition on kinetic models
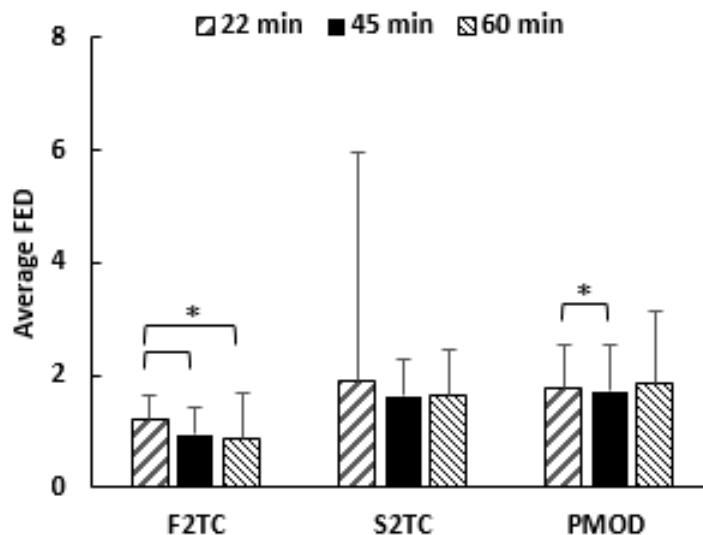
Average *FED* with within group SD of all parameter sets as error bar for F2TC model, S2TC model with custom software and PMOD for 22, 45 and 60 min of data acquisition time and noise *Sc* of 5. Data connected by brackets are different with statistical significance indicated by * for P<0.05.

2.3.4 Effect of Dynamic PET Acquisition Time on the Estimation of Model Parameters

Average *FED* using different data acquisition times for both models/software are shown in figure 2.5. Statistical difference in *FED* was observed for F2TC model when comparing 22 min with 45 ($p<0.0015$) and 60 min ($p < 0.0015$) of acquisition. For F2TC with custom software, the parameter estimation error for 22 min was the highest but the error for 45 and 60 min was comparable suggesting increasing the data acquisition time from 45 to 60 minute might not improve the accuracy of parameter estimation. This was not the case for the S2TC model with both software, the error did not decrease with longer acquisition time and no statistical significant difference was found between any time acquisitions for custom software. Since increasing data acquisition time beyond 45 min did not significantly affect the parameter estimation for the F2TC model, this time was used for comparing the effect of MTT and models on parameter estimation.

Figure 2-6: Effect of MTTs on model parameters
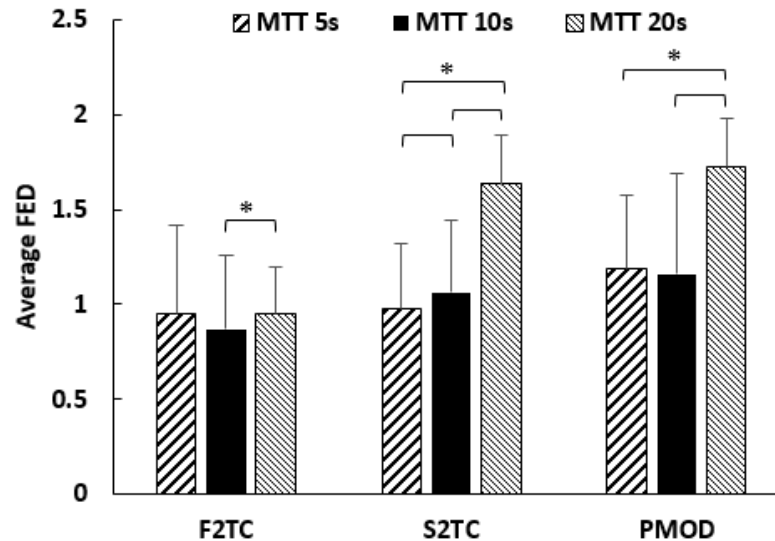
Comparison of error in parameter estimation for 5, 10 and 20 s MTT, with F2TC model and S2TC model with custom software and PMOD, 45 min acquisition time and noise *Sc* of 5. Data connected by brackets are different with statistical significance indicated by * for P<0.006.

2.3.5 Effect of MTT on the Estimation of Model Parameters

Figure 2.6 shows the effect of MTT on parameter estimation. For the F2TC model, the error in parameter estimation remained the same as MTT increased from 5 to 10 and 20 s, despite the error being statistically different between MMT of 10 and 20 s. For S2TC model with either custom software or PMOD, the error between MTT of 5 and 10s was small even though for custom software it was significant. The error between MTT of 20 s and 5 or 10 s were all significant with error with MTT of 20 s being the largest.

2.3.6 Estimation of Model Parameters with Different Models/software

Table 2.2 shows the median differences and limits of agreement (LOA) between the parameters (both explicit and summary) estimated by F2TC and S2TC (both software) model for MTT 20 s, *Sc* 5 and 45 min acquisition. Limits of agreement is defined Q1-1.5*IQR and Q3+1.5*IQR where Q1 and Q3 are the first and third quartile respectively,

and IQR is interquartile range[22]. According to non-parametric paired test, the median difference between parameters estimated by F2TC model and S2TC model with either custom software or PMOD were significantly different from zero (p<0.004) and the error was higher for K_1, k_2 (except PMOD), V_p, DV and BP (all >0.01). Table 2.3 compares the error for the case of noiseless simulated curves but still with the frame averaging effect. There is a general trend of the error being larger for all kinetic parameters estimated from noiseless TAC. Similar to *Sc* 5 (Table 2.2), larger error was observed for K_1, k_2, V_p, DV and *BP*. PMOD estimated the kinetic parameters with larger error compared to the custom S2TC model relative to the F2TC model. Table 2.4 compares the parameters estimated by the F2TC model and custom S2TC model against the simulated (true) parameters showing larger median differences for custom S2TC model. Tables 2.5 compare the error in estimated parameters for MTT 10 s, *Sc* 5 and 45 min acquisition. The median difference between the parameters estimated by F2TC model and S2TC model (both software) were significantly different from zero (except BP), LOA being larger for PMOD software. The LOA for MTT of 10 s shown in table 2.5 was smaller than that for MTT of 20 s in table 2.2.

Table 2.2: Median and limits of agreement (LOA) of difference between the parameters estimated by F2TC and S2TC model (both software) for MTT 20 s, noise scaling of 5 and 45 min of acquisition

	S2TC (Custom) vs F2TC		S2TC (PMOD) vs F2TC	
	Median Difference	**LOA**	**Median Difference**	**LOA**
K_1	-0.010[*]	-0.06 to 0.03	-0.021[*]	-0.13 to 0.07
k_2	-0.018[*]	-0.21 to 0.12	-0.006[*]	-0.24 to 0.19
k_3	0.006[*]	-0.02 to 0.03	0.009[*]	-0.05 to 0.08
k_4	0.002[*]	-0.01 to 0.02	0.002[*]	-0.01 to 0.01
V_P	0.016[*]	-0.03 to 0.07	0.013[*]	-0.04 to 0.08
DV	-0.013[*]	-0.06 to 0.03	-0.108[*]	-0.33 to 0.08
BP	0.021[*]	-0.32 to 0.30	0.054[*]	-0.51 to 0.72
K_i	-0.0005[*]	-0.004 to 0.002	-0.004[*]	-0.02 to 0.01

[*]Median difference significantly different from zero at P<0.05 with Bonferroni correction for multiple (N=8) comparisons.

Table 2.3: Median and limits of agreement (LOA) of difference between the parameters estimated by F2TC and S2TC model (both software) for MTT 20 s, noise scaling of 0 (noiseless) and 45 min of acquisition

	S2TC (Custom) vs F2TC		S2TC (PMOD) vs F2TC	
	Median	LOA	Median Difference	LOA
K_1	-0.016*	-0.06 to 0.02	-0.037*	-0.38 to 0.20
k_2	-0.037*	-0.14 to 0.05	-0.108*	-0.66 to 0.31
k_3	0.007	-0.01 to 0.03	0.006	-0.05 to 0.06
k_4	0.003*	-0.01 to 0.02	0.005	-0.01 to 0.02
V_P	0.027*	-0.01 to 0.07	0.036*	-0.12 to 0.24
DV	-0.026*	-0.07 to 0.01	-0.115*	-0.19 to -0.02
BP	0.050	-0.40 to 0.34	-0.102	-0.89 to 0.66
K_i	-0.001	-0.003 to 0.001	-0.005*	-0.03 to 0.01

*Median difference significantly different from zero at P<0.05 with Bonferroni correction for multiple (N=8) comparisons.

Table 2.4: Median and limits of agreement (LOA) of difference between the simulated parameters and parameters estimated by both F2TC and S2TC model (both software) for MTT 20 s, noise scaling of 5 and 45 min of acquisition

	F2TC vs Truth		S2TC (Custom) vs Truth	
	Median	LOA	Median Difference	LOA
K_1	-0.004*	-0.07 to 0.06	-0.021*	-0.12 to 0.07
k_2	0.013	-0.45 to 0.43	-0.047*	-0.63 to 0.45
k_3	0.024*	-0.12 to 0.16	0.024*	-0.10 to 0.15
k_4	0.003*	-0.01 to 0.02	0.006*	-0.01 to 0.03
V_P	0.012*	-0.05 to 0.08	0.033*	-0.03 to 0.10
DV	-0.016*	-0.09 to 0.06	-0.040*	-0.12 to 0.04
F	-0.222*	-1.64 to 0.90	N/A	
BP	0.185	-1.36 to 1.68	0.139*	-1.54 to 1.64
K_i	0.001*	-0.01 to 0.02	-0.001*	-0.01 to 0.01

*Median difference significantly different from zero at P<0.05 with Bonferroni correction for multiple (N=8) comparisons.

Table 2.5: Median and limits of agreement (LOA) of difference between the parameters estimated by F2TC and S2TC model (both software) for MTT 10 s, noise scaling of 5 and 45 min of acquisition

	S2TC (Custom) vs F2TC		S2TC (PMOD) vs F2TC	
	Median	LOA	Median	LOA
K_1	-0.005[*]	-0.03 to 0.01	-0.008[*]	-0.06 to 0.03
k_2	-0.009[*]	-0.09 to 0.05	0.003[*]	-0.13 to 0.13
k_3	0.003[*]	-0.01 to 0.02	0.006[*]	-0.03 to 0.05
k_4	0.001[*]	-0.003 to 0.006	0.001[*]	-0.005 to 0.007
V_P	0.008[*]	-0.02 to 0.04	0.005[*]	-0.03 to 0.05
DV	-0.007[*]	-0.04 to 0.02	-0.059[*]	-0.21 to 0.06
BP	0.017	-0.23 to 0.25	0.060[*]	-0.45 to 0.62
K_i	-0.0002[*]	-0.003 to 0.002	-0.001[*]	-0.01 to 0.01

[*]Median difference significantly different from zero at P<0.05 with Bonferroni correction for multiple (N=8) comparisons.

2.3.7   Logan Graphical Analysis

Figure 2.7 compares estimated V_T from the Logan plot, F2TC model and S2TC model with custom software and PMOD with the true simulated V_T value for the cases where MTT was 20 s for all parameter sets of table 2.1 and an acquisition time of either 45 or 60 min. The estimated V_T was compared against the 'true' value using a modified Bland-Altman plot where the x- axis was the average of the estimated V_T and the true value while the y-axis was the difference between the true and estimated V_T. Each plot shows 8 instead of 10 cluster lines because two sets of two similar V_T's are clustered together. In each plot, the solid line is the median difference while the dash are the LOA. For V_T estimated by the F2TC model and Logan analysis, the median difference from the truth became smaller when the acquisition time increased from 45 to 60 min with the F2TC model being more accurate than Logan analysis at 60 min (P= 0.2 vs 0.001). The LOA of the F2TC model also decreased more than Logan analysis as the acquisition time increased. For V_T estimated by the S2TC model with custom software and PMOD and 60 min of data acquisition, custom software was more accurate than PMOD as well the LOA was larger with PMOD than custom software.

Figure 2-7: Comparison of V$_T$ estimated by F2TC, S2TC and Logan with simulated V$_T$
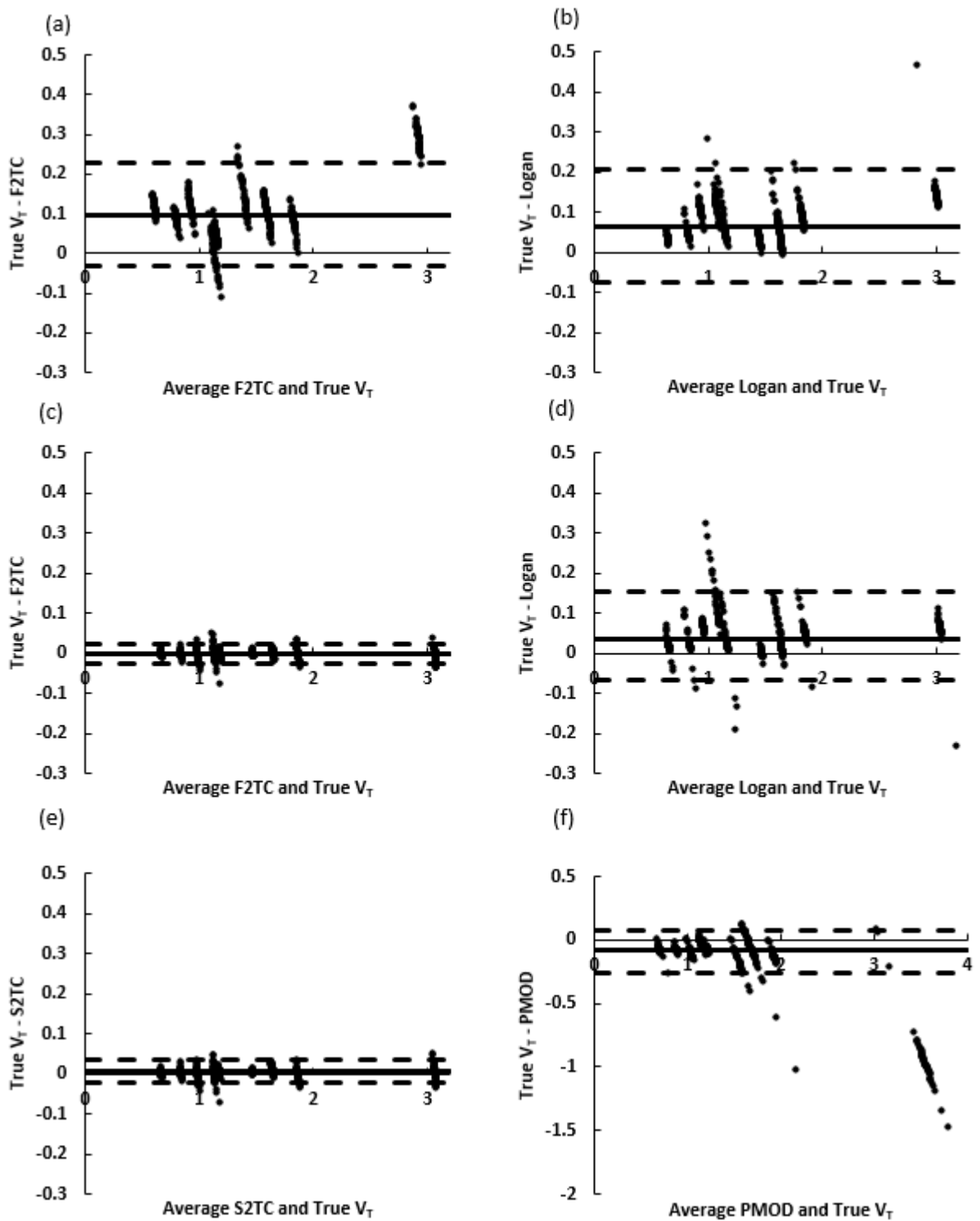
Modified Bland-Altman plot comparing true *DV* against estimated *DV* from 45 min (a, b) and 60 minute (c-f) of data acquisition. *DV*'s were estimated with F2TC model (a, c), Logan analysis (b,d), S2TC model with custom software (e) and with PMOD (f). Details of the plots are described in the text.

2.4   Discussion and Conclusion

In this study we demonstrated that the compartmental assumption for blood vessels affects the accuracy of estimated kinetic parameters because the bidirectional permeation of the blood-tissue barrier occurs instantaneously rather than over a period, equals to the transit time of blood vessels. The error was estimated as the average *FED* over all the parameter sets where *FED* is the fractional distance of the estimated from the true set of parameters in multidimensional parameter space (see equation 13). There was significantly larger error for both the S2TC model software than F2TC model, with PMOD performing the worst. As expected, the error was larger for higher noise level for all models/software. Concerning the length of acquisition time required for accurate parameter estimation, the F2TC model results show that 45 min was comparable to 60 min in the accuracy of estimated kinetic parameters and hence is sufficient for parameter estimation from dynamic PET. Due to the introduction of mean transit time in the F2TC model, we investigated the effect of MTT from 5 to 10 and 20s. For the F2TC model, *FED* did not change appreciably with MTT even though there was significant difference between 10 and 20 s. However, with both the S2TC software, increasing MTT from 5 to 20 s introduced a 50% increase in *FED*. In addition, V_T estimated by the F2TC model was more accurate than Logan analysis or the PMOD software.

Though F2TC model is used for simulating the tissue TAC, errors were observed when the simulated curve was fitted with the same model. There are several reasons for the errors. First, estimation of either the S2TC or F2TC model parameters requires the use of non-linear optimization techniques, which are iterative and depending on the initial estimates chosen to start the iteration could converge to a local instead of the global minimum, resulting in errors in the estimated parameters [23]. In this study, spectral analysis with the S2TC model was used to generate the initial parameter estimates that could be 'close' to the global minimum thereby minimizing this source of error. Linearization of tissue TAC would allow linear least squares methods to be used for model parameter estimation, which requires much less computation time than iterative non-linear optimization and more significantly would converge to the global minimum. However, the linearized tissue TAC involves double integral of the original curve, the correlated noise would lead to biased

model parameter estimates [24]. Another source of error was frame averaging that is invariably used in dynamic PET to improve the signal-to-noise of the tissue TAC. In this study, both the arterial and tissue TAC were simulated at 0.5 s interval, frame averaged and placed at mid time point of the framing schedule. From table 2.3, it demonstrated that frame averaging introduced errors in K_1 and k_2 estimated by the S2TC model (both software) when compared to the F2TC model.

Figure 2.6 shows that longer mean transit time caused larger average *FED* of parameters estimated using the S2TC model with either custom software or PMOD than F2TC model. In dynamic PET imaging, the tracer is injected intravenously (systematically) and continues to recirculate throughout the whole body. During each transit of tracer through the vessels, there is continuous influx and efflux of tracer into the EES (from nonzero K_1 and k_2 values), failure to properly model the transit time can result in erroneous (larger bias) K_1 and k_2 estimate, hence would also affect the downstream k_3 and k_4. This is especially important in conditions like ischemic stroke where there is increased mean transit time with decreased cerebral blood flow and blood volume[25]. Additionally, S2TC model's assumption of instant arrival and washout of tracer led to zero or underestimation of blood volume which is not physiological and could explain why some kinetic studies did not report on the estimates of blood volume[26–28] or was reported as zero[29].

Using *FED*, figures 2.3-6 showed that the F2TC model is better than the S2TC model with either the custom software or PMOD. *FED* being a summary over all parameters is affected by the parameters related to the vascular effect (K_1, k_2 and V_p) as well as binding to and dissociation from target (k_3 and k_4). Since dynamic PET data are 'corrupted' by frame averaging and noise, a fair comparison of model performance would have to include these effects. Consistent with these considerations, parameter estimates obtained by the S2TC and F2TC model on simulated curves that included frame average and noise (see simulation procedure in §2.4.1) for MTT 20 s were compared. The error in parameters estimated by the S2TC model with custom software was >0.01 for K_1, k_2, V_p, *DV* and *BP* and <0.01 for other parameters (table 2.2). With only frame averaging simulation, the error in parameters estimated by the S2TC model (both software) was higher (table 2.3). With lower MTT of 10 s, the error was reduced to <0.01 for all parameters estimated by the S2TC model with

the exception of *BP*. Taken together, these results support our proposition that ignoring the transit time effect in blood vessels affect the accuracy in the estimation of vascular parameters (K_1, k_2 and V_p) as well as k_3 and k_4 albeit the effect on the latter two parameters is less than the first group. Of interest, noise seem to reduce the error of estimated parameters which could be due to the effect of noise masking the error introduced by frame averaging. This effect merits further investigation. Another finding is that accuracy of parameter estimates with PMOD was much poorer compared to the custom software we developed for the S2TC model. As PMOD is a proprietary software it is difficult to diagnosis what was the root cause.

Logan analysis is independent of the structure of the compartments and should be more robust in V_T estimation. However, our study showed otherwise – F2TC model estimated V_T was more accurate than Logan analysis. Similar result was also observed by the Logan's simulation study where V_T estimated by Logan analysis was subject to bias when noise was present in the tissue TAC [17]. The bias increased with V_T and noise. The noise dependence means that it also depends on the physical half-life of the tracer used - shorter half-life means higher level of noise at later time points of the tissue TAC. Logan analysis plots the time integral of tissue TAC vs that of the arterial TAC (see § 2.6) and the V_T is the slope of the linear regression line in such a plot. A fundamental assumption of linear regression is that noise in the data is uncorrelated. However, time integrals add noise of the tissue or arterial activity at different points together leading to noise correlation. The violation of the independence of noise would lead to the observed bias in the estimate of V_T [24].

In this study, we showed that the F2TC model has better accuracy in estimating kinetic parameters from dynamic PET imaging than the S2TC model. Noise which is more prominent in voxel wise than ROI analysis, influences strongly the accuracy and precision of estimated kinetic parameters. Contrary to current practice, we found that 45 minute of data acquisition is sufficient for accurate parameter estimation for the 10 sets of parameter obtained from [18F]FET. Larger parameter sets covering wider range of physiological conditions will need to be further investigated. One major disadvantage of the F2TC model is that it is iterative and computationally more expensive due to estimation of *W* (vessel mean transit time) and T_0 (tracer arrival time) by sequential step-wise search. However,

with machine learning or by executing the program in C++, the fitting time can be improved considerably.

2.5   References

1. Vriens D, Visser EP, De Geus-Oei LF, Oyen WJG. Methodological considerations in quantification of oncological FDG PET studies. *Eur J Nucl Med Mol Imaging*. 2010;37(7):1408-1425. doi:10.1007/s00259-009-1306-7

2. Lammertsma AA. Forward to the past: The case for quantitative PET imaging. *J Nucl Med*. 2017;58(7):1019-1024. doi:10.2967/jnumed.116.188029

3. Suzuki K, Nishioka T, Homma A, et al. Value of fluorodeoxyglucose positron emission tomography before radiotherapy for head and neck cancer: Does the standardized uptake value predict treatment outcome? *Jpn J Radiol*. 2009;27(6):237-242. doi:10.1007/s11604-009-0330-7

4. Menda Y, Boles Ponto LL, Dornfeld KJ, et al. Kinetic Analysis of 3'-Deoxy-3'-18F-Fluorothymidine (18F-FLT) in Head and Neck Cancer Patients Before and Early After Initiation of Chemoradiation Therapy. *J Nucl Med*. 2009;50(7):1028-1035. doi:10.2967/jnumed.108.058495

5. Crone C. The Permeability of Capillaries in Various Organs as Determined by Use of the 'Indicator Diffusion' Method. *Acta Physiol Scand*. 1963;58(4):292-305. doi:10.1111/j.1748-1716.1963.tb02652.x

6. Dimitrakopoulou-Strauss A, Pan L, Strauss LG. Quantitative approaches of dynamic FDG-PET and PET/CT studies (dPET/CT) for the evaluation of oncological patients. *Cancer Imaging*. 2012;12(1):283-289. doi:10.1102/1470-7330.2012.0033

7. Logan J. Graphical analysis of PET data applied to reversible and irreversible tracers. *Nucl Med Biol*. 2000;27(7):661-670. doi:10.1016/S0969-8051(00)00137-2

8. Logan J. A review of graphical methods for tracer studies and strategies to reduce bias. *Nucl Med Biol*. 2003;30(8):833-844. doi:10.1016/S0969-8051(03)00114-8

9. Patlak CS, Blasberg RG, Fenstermacher JD. Graphical evaluation of blood-to-brain transfer constants from multiple-time uptake data. *J Cereb Blood Flow Metab*. 1983;3(1):1-7. doi:10.1038/jcbfm.1983.1

10. Mintun MA, Raichle ME, Kilbourn MR, Wooten GF, Welch MJ. A quantitative model for the in vivo assessment of drug binding sites with positron emission tomography. *Ann Neurol*. 1984;15(3):217-227. doi:10.1002/ana.410150302

11. Gunn RN, Lammertsma AA, Hume SP, Cunningham VJ. Parametric imaging of ligand receptor binding in PET using a simplified reference region model. *Neuroimage*. 1997;6:279-287.

12. Lawrence KS St., Lee T-Y. An Adiabatic Approximation to the Tissue Homogeneity Model for Water Exchange in the Brain: II. Experimental Validation. *J Cereb Blood Flow Metab*. 1998;18(12):1378-1385. doi:10.1097/00004647-199812000-00012

13. Meier P, Zierler KL. On the theory of the indicator-diliution method for measurement of blood flow and volume. *J Applied Physiol*. 1954;6(12):731-744.

14. Debus C, Afshar-Oromieh A, Floca R, et al. Feasibility and robustness of dynamic 18F-FET PET based tracer kinetic models applied to patients with recurrent high-grade glioma prior to carbon ion irradiation. *Sci Rep*. 2018;8(1):1-17. doi:10.1038/s41598-018-33034-5

15. Ben Bouallègue F, Vauchot F, Mariano-Goulart D. Comparative assessment of linear least-squares, nonlinear least-squares, and Patlak graphical method for regional and local quantitative tracer kinetic modeling in cerebral dynamic 18 F-FDG PET. *Med Phys*. 2019;46(3):1260-1271. doi:10.1002/mp.13366

16. Feng D, Huang S-C, Wang X. Models for computer simulation studies of input functions for tracer kinetic modeling with positron emission tomography. *Int J Biomed Comput*. 1993;32(2):95-110. doi:https://doi.org/10.1016/0020-

7101(93)90049-C

17. Logan J, Fowler JS, Volkow ND, Ding YS, Wang GJ, Alexoff DL. A strategy for removing the bias in the graphical analysis method. *J Cereb Blood Flow Metab*. 2001;21(3):307-320. doi:10.1097/00004647-200103000-00014

18. Hamberg LM, Hunter GJ, Alpert NM, Choi NC, Babich JW, Fischman AJ. The dose uptake ratio as an index of glucose metabolism: Useful parameter or oversimplification? *J Nucl Med*. 1994;35(8):1308-1312.

19. Rosiers MHD Des, Sokoloff L, Reivich M, et al. The [14C]Deoxyglucose Method for the Measurement of Local Cerebral Glucose Utilization: Theory, Procedure, and Normal Values in the Conscious and Anesthetized Albino Rat. *J Neurochem*. 1977;28(5):897-916. doi:10.1111/j.1471-4159.1977.tb10649.x

20. Veronese M, Rizzo G, Bertoldo A, Turkheimer FE. Spectral analysis of dynamic PET studies. *J Cereb Blood Flow Metab*. 1993;13(1):15-23. doi:10.1038/jcbfm.1993.5

21. Altman DG, Bland JM. Measurement in Medicine: The Analysis of Method Comparison Studies. *Stat*. 1983;32(3):307. doi:10.2307/2987937

22. Tukey J. *Exploratory Data Analysis*. Reading (MA): Addison-Wesley; 1977.

23. Feng D, Huang S-C, Wang Z, Ho D. An unbiased parametric imaging algorithm for nonuniformly sampled biomedical system parameter estimation. *IEEE Trans Med Imaging*. 1996;15(4):512-518.

24. Feng D, Ho D, Lau KK, Siu WC. GLLs for optimally sampled continuous dynamic system modeling: Theory and algorithm. *Comput Methods Programs Biomed*. 1999;59(1):31-43. doi:10.1016/S0169-2607(98)00099-6

25. Lin MP, Liebeskind DS. Imaging of Ischemic Stroke. *Contin (Minneap Minn)*. 2016;22(5):1399-1423. doi:10.1212/CON.0000000000000376

26. Muzi M, Vesselle H, Grierson JR, et al. Kinetic analysis of 3′-deoxy-3′-fluorothymidine PET studies: Validation studies in patients with lung cancer. *J*

Nucl Med. 2005;46(2):274-282.

27.   Rusjan PM, Wilson AA, Bloomfield PM, et al. Quantitation of translocator protein binding in human brain with the novel radioligand 18 F-FEPPA and positron emission tomography. *J Cereb Blood Flow Metab*. 2011;31(8):1807-1816. doi:10.1038/jcbfm.2011.55

28.   Richard MA, Fouquet JP, Lebel R, Lepage M. Determination of an optimal pharmacokinetic model of 18F-FET for quantitative applications in rat brain tumors. *J Nucl Med*. 2017;58(8):1278-1284. doi:10.2967/jnumed.116.180612

29.   Dimitrakopoulou-Strauss A, Strauss LG, Schwarzbach M, et al. Dynamic PET 18F-FDG studies in patients with primary and recurrent soft-tissue sarcomas: Impact on diagnosis and correlation with grading. *J Nucl Med*. 2001;42(5):713-720.

Chapter 3

3 Pharmacokinetic Analysis of Dynamic [^{18}F]FAZA PET Imaging in Pancreatic Cancer Patient

3.1 Introduction

Pancretic cancer (PCa) ranks as the fourth most common cause of cancer death in North America because of its lowest overall five-year survival rate [1,2]. In 2018 alone, 55,440 Americans were diagnosed with the cancer and 44,330 died from it according to American Cancer Society [3]. Diagnosis of PCa is often made at an advanced stage after the tumor has metastasized resulting in poor survival rate [4,5]. In addition, PCa is very challenging to treat because of hypoxia induced chemo- and radio-resistance [4,6,7]. The non-invasive diagnosis of hypoxia in PCa to guide personalized treatment may improve the survival of patients.

Positron emission tomography (PET) is a non-invasive in-vivo imaging method to study the molecular and functional characteristics of cancer. A number of hypoxic tracers have been developed of which nitroimidazole (NI) based tracers, [^{18}F]fluoromisonidazole ([^{18}F]FMISO) and [^{18}F]fluoroazomycin arabinoside ([^{18}F]FAZA), are widely used. [^{18}F]FAZA is the preferred hypoxia tracer due to its higher lipophilic property, leading to faster delivery into the cells and blood clearance and hence higher tumor to blood ratio [7–9]. In general, the tracer enters the cell through passive diffusion and the nitro group is reduced by nitroreductase to NO_2^- radical. Under well-oxygenation conditions, the radical is oxidized back to its original form and diffuses out of the cells. Under poor oxygenation

Figure 3-1: [^{18}F]FAZA binding mechanism
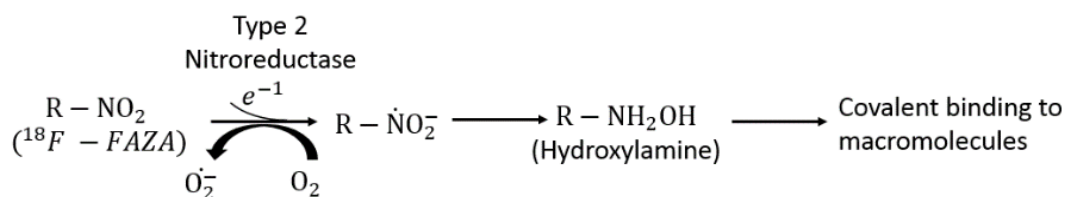
Current view of [^{18}F]FAZA binding in cells under condition of normoxia and hypoxia

Figure 3-2: Kinetic models for dynamic PET
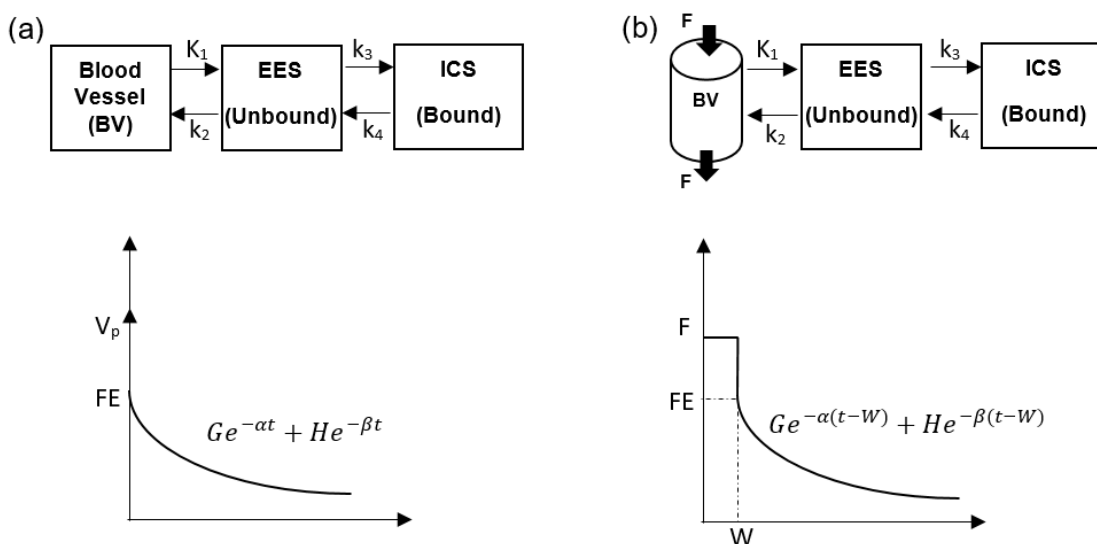
S2TC model (a): free unbound tracer in the blood vessel and extravascular extracellular space (EES) and the bound tracer in intracellular space (ICS) are categorized into different compartments. $K_1 (mL \cdot min^{-1} \cdot g^{-1})$ is the tracer influx rate into EES, k_2 (min^{-1}) is the efflux rate constant from EES to blood, $k_3 (min^{-1})$ is binding rate constant, and k_4 (min^{-1}) is disassociation rate constant. If tracer binding is irreversible, k_4 is zero. (b) F2TC model: The EES and ICS compartment are retained as in S2TCM but blood vessels are represented as a cylindrical tube, and as tracer traverse the blood vessels, it diffuses into EES creating a concentration gradient from arterial to venous end. $F(mL \cdot min^{-1} \cdot g^{-1})$ is blood flow. The corresponding flow scaled impulse residue function (IRF$_F$) is shown below the model.

condition or hypoxia, the highly reactive -NO$_2$ radical damages DNA and traps the ^{18}F labelled radical. NO$_2^-$ radical can be further reduced to hydroxylamine and its intermediates are trapped in the cells by covalently bonding to proteins and macromolecules[9–16]; normally the direct covalent bonding of NO$_2^-$ radical to DNA is much faster than further downstream reduction via hydroxylamine[10,17]. With either route of metabolism, [^{18}F]FAZA is assumed to be irreversibly trapped in hypoxic cells (Fig. 3.1).

Dynamic PET provides data on the temporal distribution of a tracer in tissue, which is necessary for modelling the pharmacokinetics of the tracer[18,19]. The classical method of analysing the kinetics of NI tracer is standard irreversible two-tissue compartment (S2TC)

model (Fig. 3.2a). One limitation of S2TC model is that it does not model the transit of the tracer through blood vessels rather it is lumped together as the product of the tracer concentration in (arterial) blood and the blood volume. A consequence is that the estimated blood volume can be very small particularly if the dynamic PET study has rapid framing rate (5-10 s per frame) in the first phase and the S2TC model fit includes this fast first phase. To better describe the transport of tracer into tissue, we combine the Johnson-Wilson-Lee (JWL) model [20] with the S2TC model to arrive at the flow modified two-tissue compartment (F2TC) model. It models the flow of tracer in blood vessels and the bidirectional permeation of the blood-tissue barrier during the finite transit time through these vessels leading to a concentration gradient from the arterial end to the venous end (Fig. 3.2b). In contrast, S2TC model assumes the bidirectional permeation of the blood-tissue barrier occurs 'instantaneously' rather than over a period equals to the transit time of blood vessels.

Contrary to the common understanding of the in-vivo behaviour of NI tracers, some studies have shown that the tissue time-activity curve (TAC) is best fitted using a reversible S2TC model[21,22]. In this study, we investigated the nature of [18F]FAZA binding to pancreatic tumor in patients using graphical analysis[23] and S2TC and F2TC model. As noted above F2TC model does while S2TC model does not account for the fact that transport of tracer into tissue occurs over the transit time of the blood vessels rather than instantaneously, use of both models will show how this effect affects the estimated model parameters. To confirm model fitting, depending on the nature of tracer binding, forward transfer rate (plasma to tissue influx rate) for irreversible bound tracer[24] or distribution volume for reversible tracer[23] as calculated from the estimated S2TC and F2TC model parameters will be compared with that estimated by graphical analysis. Finally the estimated model parameters can shed light on the possible pharmacokinetics and hence the mechanisms behind the accumulation of [18F]FAZA and washout from tumor cells.

3.2   Methods

3.2.1 Patient population and image acquisition

The patient cohort consisted of 20 patients with biopsy confirmed and previously untreated pancreatic ductal adenocarcinoma. The study was approved by University Health Network Research Ethics Board and a signed consent form from each enrolled patient was obtained. Details of the patient population and image acquisition were described previously[25,26]. Dynamic images were acquired over 55 min with the following imaging protocol: 12@10s intervals, 8@30s, 7@120s and 7@300s. PET scans were acquired with in-line PET/CT scanner (Discovery ST-16; GE Healthcare). Whole tumor TAC was derived from regions manually contoured by an experienced radiologist in all tumor containing tumor slices. Arterial input function (AIF) was obtained from aorta at the same level as the tumor ROIs with no metabolite correction. Out of the 20 patients, only 14 patients had TAC from normal tissue due to pancreatic atrophy in the remaining patients.

3.2.2 Dynamic PET analysis

Whole tumor TAC and AIF from each patient were analyzed in three ways: graphical analysis and kinetic analyses using the S2TC and F2TC models.

3.2.2.1   Graphical analysis

It is a compartmental analysis technique which is independent of the number and connectivity of the compartments and can be used to investigate the nature of the binding of [^{18}F]FAZA to tumor. For irreversible binding, when tissue TAC ($ROI(t)$) and AIF ($C_p(t)$) are transformed as shown in Eq (1), a linear Patlak[23,24] plot is obtained following a short delay where the slope (K_i) is the forward transfer rate of tracer from blood to the bound pool and the intercept is the blood volume (V_b):

$$\frac{\int_0^t C_p(\tau)\, d\tau}{C_p(t)} = K_i \frac{ROI(t)}{C_p(t)} + V_P \tag{1}$$

On the other hand, Eq (2) shows that for reversible binding, the transformed $ROI(t)$ and $C_p(t)$ after a short delay are linearly related (Logan plot[23,27]) with slope equal to the sum

of the extravascular distribution volume (DV) and blood volume (V_P) or total distribution volume ($V_T = V_P + V_D$):

$$\frac{\int_0^t C_p(\tau)d\tau}{ROI(t)} = (V_P + DV)\frac{\int_0^t ROI(\tau)d\tau}{ROI(t)} + Int. \tag{2}$$

If the plot according to either Eq(1) or Eq(2) is linear, then the tracer is irreversibly or reversibly bound respectively.

3.2.2.2 Standard two-tissue compartment model (S2TC)

In dynamic PET, the measured tissue activity arises from tracer in the blood vessels, free unbound tracer in extravascular space and tracer bound in the target. S2TC model categorizes these different anatomical/physiological states of the tracer as compartments. In this model, the consequence of modeling blood vessels as a compartment is that tracer once arrived is assumed to be immediately mixed uniformly with tracer already in the vessels and to immediately diffuse out to tissue. This is reflected in the flow scaled impulse residue function (IRF$_F$(t)) where the vascular component is a delta function of area equal to the blood volume, $V_P(ml \cdot g^{-1})$. IRF$_F$(t) is an idealized tissue TAC if the total amount of tracer is injected as a tight bolus into a blood vessel supplying the tissue of interest. The tissue TAC, ROI(t) corresponding to a systemic injection of tracer as in dynamic PET is obtained by convolution of the AIF with IRF$_F$(t) based on the principle of linear superimposition. The above discussion is summarized by the following equations:

$$ROI(t) = C_p(t) \otimes IRF_F(t - T_0) \tag{3}$$

where T_0 is the delay (s) in arrival of tracers from the site where AIF is measured to the tissue region of interest

$$IRF_F(t) = \begin{cases} V_P\delta(t) & t = 0 \\ Ge^{-\alpha t} + He^{-\beta t} & t > 0 \end{cases} \tag{4}$$

$$\alpha = \frac{k_2 + k_3 + k_4 + \sqrt{(k_2 + k_3 + k_4)^2 - 4k_2k_4}}{2} \tag{5}$$

$$\beta = \frac{k_2 + k_3 + k_4 - \sqrt{(k_2 + k_3 + k_4)^2 - 4k_2k_4}}{2} \tag{6}$$

$$G = \frac{K_1(\alpha - k_3 - k_4)}{\alpha - \beta} ; H = \frac{K_1(k_3 + k_4 - \beta)}{\alpha - \beta} \qquad (7)$$

α, β, G and H are fitting parameters estimated from curve fitting and it is expressed in terms of the explicit model parameters K_1, k_2, k_3 and k_4 as defined in the legend of Fig. 3.2; and $\otimes$ is the convolution operator.

3.2.2.3 Flow modified two-tissue compartment (F2TC) model

To avoid the compartmental assumption for tracer in blood vessels with shortcomings as discussed above, we developed a new model called flow modified two – tissue compartment model (F2TC). It models the bidirectional tracer permeation of the blood-tissue barrier during the finite transit time through blood vessels (Fig. 3.2b). This is reflected in the $IRF_F(t)$ where the delta function in the case of S2TC model is replaced by a rectangular function with a width equal to the transit time (w) of the tracer from arterial to venous end of blood vessels. The rest of $IRF_F(t)$ remains the same as the S2TC model. The mathematical representation for F2TC model's $IRF_F(t)$ is:

$$IRF_F(t) = \begin{cases} F & 0 \leq t < w \\ Ge^{-\alpha(t-w)} + He^{-\beta(t-w)} & t \geq w \end{cases} \qquad (8)$$

The fitting parameters are the same as the S2TC model except that V_P is replaced by w and can be calculated as the product of w and F according to the Central Volume Principle [28].

3.2.2.4 Analysis of Tumor and Tissue TAC

PKIN (PMOD technologies LLC, Zurich, Switzerland) with blood delay option was used to fit the S2TC model to the tumor and normal tissue TAC while custom software developed in MATLAB (The Mathworks Inc.) incorporating the 'interior-point' non-linear optimization routine was used to fit F2TC model to the same the TACs. The model that better represented the TACs was determined by comparing the root mean square deviations (RMSD) between the TAC and the model fit with Wilcoxon signed-rank test and by the Akaike Information Criteria (AIC [22]) for small sample size

$$AIC = N.\ln\left(\frac{RMSD}{N}\right) + \frac{2(K+1)(K+2)}{N-K-2} \qquad (9)$$

where N is the number of time frames, K is number of parameters in each model. With explicit model parameters estimated from curve fitting, important summary parameters like $K_i = \frac{k_1 k_3}{k_2+k_3+k_4}$ $V_D = \frac{k_1}{k_2}\left(1 + \frac{k_3}{k_4}\right)$ and $BP = \frac{k_3}{k_4}$ can be calculated. K_i is the net influx rate from the blood vessel to the bound pool and BP the binding potential [29,30]. Bland-Altman plot [31] of median and interquartile extremes of V_T estimated with the F2TC and S2TC model were compared against those estimated by Logan plot. The extremes are calculated as Q1-1.5*IQR and Q3+1.5*IQR, where Q1 and Q3 are the first and third quartile and IQR is the interquartile range. Both the summary and explicit parameters estimated by F2TC and S2TC model were compared using non-parametric paired test. Depending on whether the distribution of the differences between the two sets of parameters is symmetrical or asymmetrical, either Wilcoxon signed rank test or sign test, respectively, was used to test for significant difference between the two models. Univariable logistic regression of explicit model parameters (V_P, K_1, k_i i=2,3,4) and DV was used to determine their significance in differentiating normal tissue from cancer. Logistic regression with backward elimination of a group of above parameters, each selected if the associated

Figure 3-3: Graphical analysis of [^{18}F]FAZA tissue TAC from a pancreatic tumor
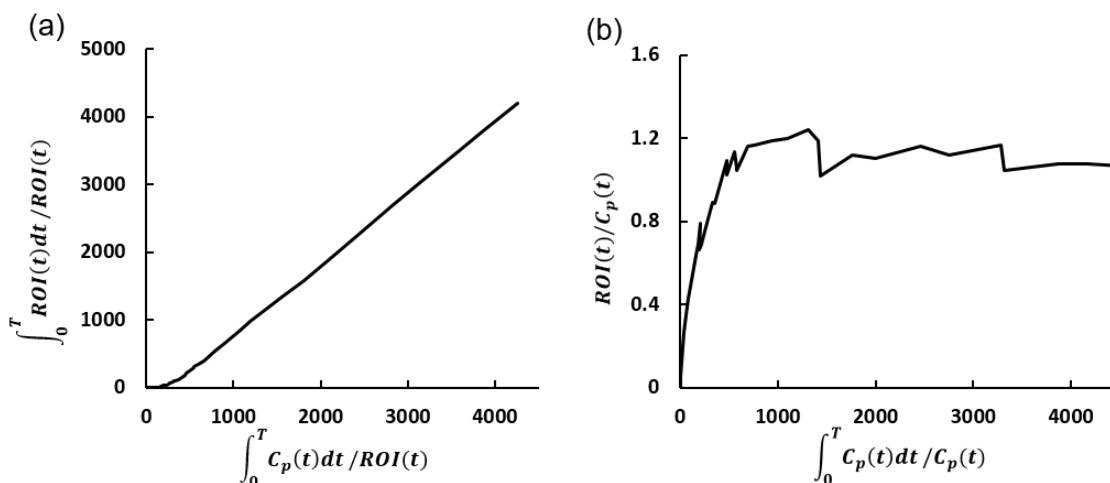
Linear plot of Logan analysis (a) and non-linear plot of Patlak analysis (b) indicated that the tracer was reversibly bound contrary to the current view of irreversible binding

univariable analysis attained a P-value of < 0.1, was used to determine the optimal set of parameters to differentiate normal from hypoxic tumors.

3.3　Results

3.3.1　Reversibility of [^{18}F]FAZA Binding

The non-linear Patlak analysis plot vs the linear Logan analysis plot (Fig. 3.3) proved that the tracer was reversibly bound contrary to the commonly held view that it is irreversibly bound. This result was further corroborated by pharmacokinetic analysis where the median RMSD difference between the model fit and measure TAC in either normal tissue or tumor was smaller with reversible F2TC model (both α and β estimated) than the irreversible model (β set to zero) (z = 3.78, p<0.005).

3.3.2   Model selection

Figure 3-4: RMS and AIC comparison from F2TC and S2TC model fitting
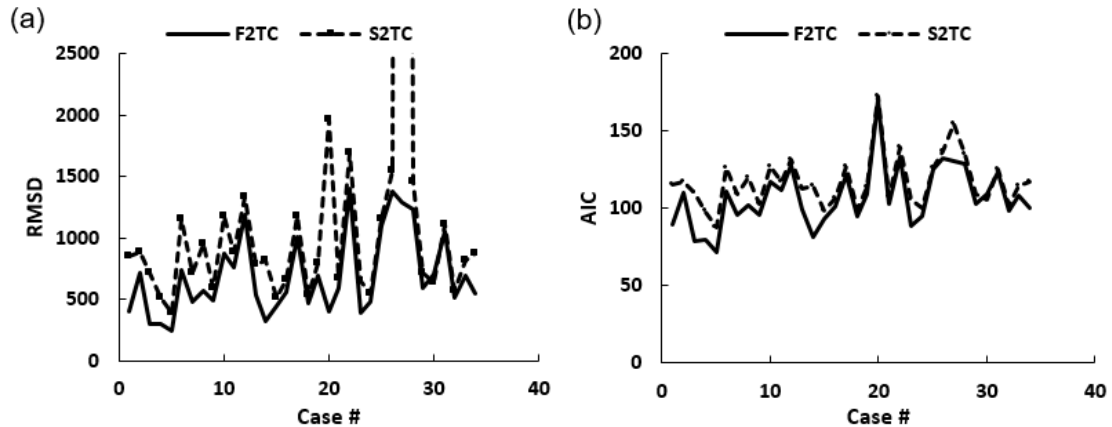
Comparison of F2TC and S2TC model in fitting tumor and normal tissue TAC using (a) RMSD and (b) AIC as measure of goodness of fit. The x-axis is patient number. Case #1-20 corresponds to tumors and Case #21-34 are normal pancreatic tissues from same patients as 1-20. Normal tissues were observable in PET imaging in 14 patients only

As indicated by AIC and RMSD in Fig. 3.4, our developed F2TC model was able to fit the tumor and normal tissue TAC better than S2TC model (p = 0.002, p<0.0005 respectively). S2TC model also estimated the blood volume (V_P) poorly. The average tumor V_P estimated by F2TC and S2TC models, though not significantly different, was 0.1039 and 0.0737 $mL \cdot g^{-1}$ respectively with a few S2TC model's V_P estimated to be zero which is non-physiological. According to non-parametric test, the explicit model parameters (V_P, K_1, k_i (i = 2,3,4)) as well as the summary parameter BP and K_i estimated by the F2TC and S2TC model were not significantly different (p> 0.05). However, DV and K_1/k_2 were significantly different (p<0.0005). Fig. 3.5 are Bland-Altman plots comparing V_T estimated by Logan analysis against the F2TC and S2TC model. The median differences (thick black line) and extremes of agreement (dash lines) were significantly lower for F2TC model compared to S2TC model and V_T from F2TC model was not but S2TC model was significantly different from that estimated by Logan analysis. Extremes of agreement were Q1-1.5*IQR and Q3+1.5*IQR where Q1, Q3 and IQR are 1st and 3rd quartile and interquartile range respectively.

Figure 3-5: Bland- Altman plots comparing total distribution volume
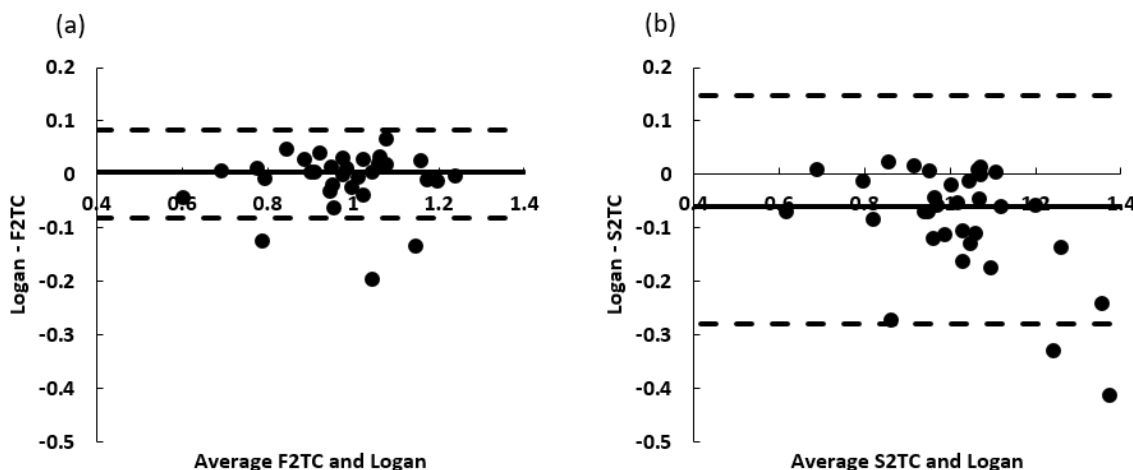
Bland-Altman plot comparing total distribution volume (V_T) estimated for hypoxic and normal tissue with Logan graphical analysis and with (a) F2TC and (b) S2TC model. The solid lines are the median differences and dashed lines are explained in the text.

3.3.3   Differentiation of Tumor from Normal Tissue

Among the kinetic parameters estimated with the F2TC model, only k_4 and DV were significant (p<0.05) in univariable logistic regression analysis to separate normal tissue from tumor. Using a subset of kinetic parameters (V_P, DV and k_4), each of which had p<0.1 in univariable analysis, logistic regression with backward elimination identified k_4 and DV as a significant model (p=0.003) to separate normal tissues from hypoxic cancerous tissues (Fig. 3.6a). The model correctly classified 79% of the cases with specificity of 57% and sensitivity of 95%. The positive predictive value (PPV) was 76% and negative predictive value (NPV) 89%. With the S2TC model, univariate analysis showed that only DV had p<0.1 that correctly classified 71% of cases with sensitivity, specificity, PPV and NPV of 90 %, 43%, 68% and 64% respectively (p = 0.047).

3.4   Discussion

The developed F2TC model models the bidirectional permeation of the blood-tissue barrier as the tracer traverses the blood vessels over a period equals to the mean transit time,

Figure 3-6: Differentiation of hypoxic tumor from normal tissue with kinetic parameters estimated by F2TC and S2TC model
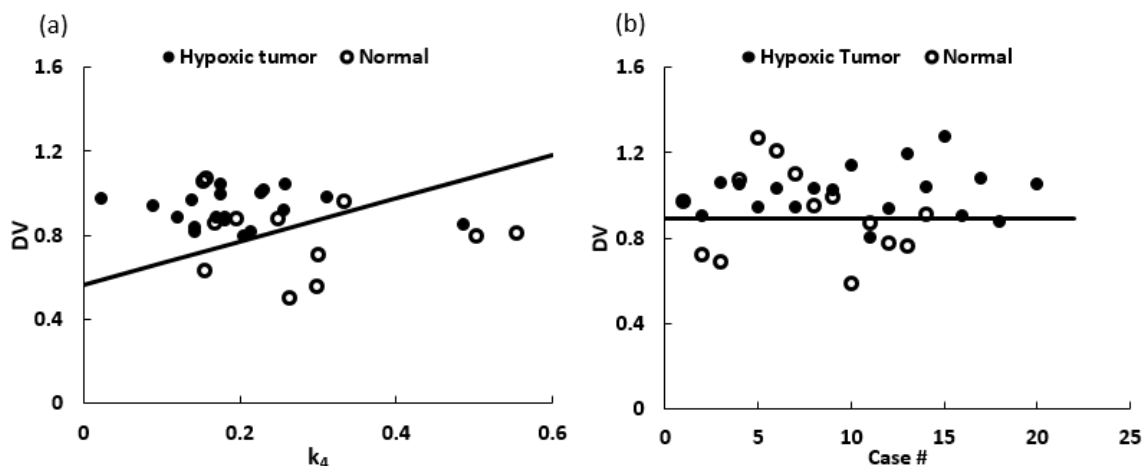
Distinguishing pancreatic tumor from normal tissue using kinetic parameters estimated with F2TC and S2TC model. (a) For the F2TC model, distribution volume (DV) and k_4 can distinguish the two tissue types with sensitivity of 95% and (b) For the S2TC model, DV achieved a sensitivity of 90%. The solid line in each case is the linear discriminator derived from the Youden index (Cancer 1950; 3(1): 32-35). For each case, DV for one patient's hypoxic tumor is large due to zero β estimate which was not plotted here but was included in the performance metric calculations

resulting in a concentration gradient from the arterial to venous end of vessels. On the other hand, S2TC model assumes that fresh tracer in arterial blood is instantaneously and uniformly mixed with tracer already in the blood vessels and instantaneously washout of blood vessels. This unrealistic assumption resulted in a smaller V_P estimate than the F2TC model and in some cases even a non-physiological estimate of zero. Total distribution volume, V_T, estimated by the F2TC model for both tumor and normal pancreatic tissue was not but that estimated by the S2TC model was significantly different from Logan graphical analysis. This result was also supported by both AIC and RMSD of the fit to the tissue

Figure 3-7: Proposed binding mechanisms of [18F]FAZA binding
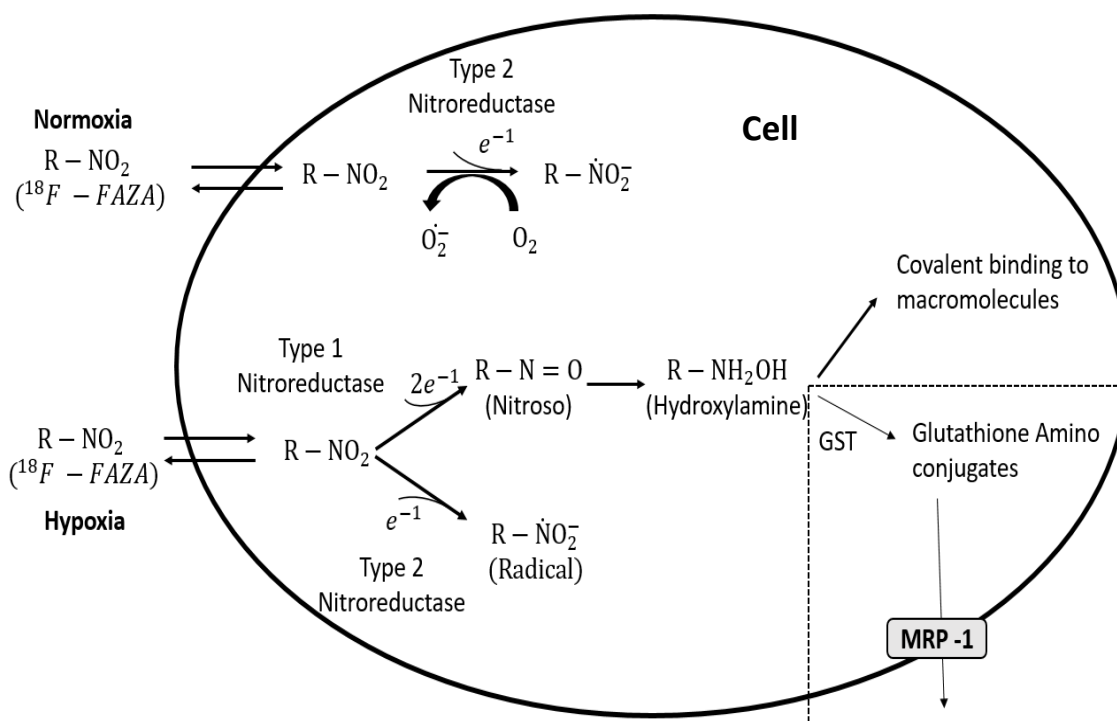
Mechanisms for hypoxia imaging with nitroimidazole based tracers like [^{18}F]FAZA. The region indicated by dashed box is the proposed mechanisms behind the reversibility of tracer binding

TAC that the F2TC model was more suited than S2TCM for describing the kinetics of [^{18}F]FAZA in hypoxic tumor and normal tissue of the pancreas.

The hypoxic pancreatic cancer tissue can be characterized from the normal tissues using k_4 and DV from the F2TC model with high sensitivity of 95% and negative predictive value of 89%. On the contrary, DV from the S2TC model can distinguish the two tissue types with lower sensitivity and NPV. DV is a surrogate marker of SUV acquired at sufficiently long time after tracer injection, when the blood background is negligible[32]. Therefore, using DV from S2TC model corroborates the usage of SUV for hypoxia imaging in the clinics, which is performed at least one hour after injection. Nevertheless kinetic analysis by providing k_4 and DV could out-perform SUV (DV) in this diagnostic task.

Graphical method as well as lower RMSD from the reversible (non-zero β) F2TC model compared to the irreversible model demonstrated that the tracer [^{18}F]FAZA was reversibly bound to hypoxic PCa, contrary to the current view that NI based tracers are trapped in hypoxic cells. Unlike kinetic modelling, graphical method is independent on the structure (connectivity) and the number of compartments in the model which makes it more adaptable to prevailing tumor heterogeneity, i.e. a single F2TC or S2TC model may not apply to all regions in a tumor. Hence, graphical analysis is a reliable method to determine the reversibility of tracer binding. Previous studies also corroborated our finding that the kinetics of NI based tracers are best analyzed using reversible S2TC model[21,22]. Nonetheless, the mechanism behind the reversible binding of NI based tracers was not well described in the literature.

A group in Japan studied the mechanism of NI based [^{18}F]FMISO binding in nude mice by implanting cells from the human FaDu cancer line [14,33,34]. They found that the majority of the tumor radioactivity was from low molecular weight metabolite, glutathione (GST) conjugate of amino-FMISO (amino-FMISO-GH)[14,34,35]. Amino-FMISO-GH is highly hydrophilic and cannot diffuse out of the cell. However, it could efflux out via the adenosine triphosphate (ATP) dependent multi-drug resistant protein (MRP-1)[34,36], which is highly expressed in pancreatic tumor cells [5,37–39] and is responsible for drug resistance. A similar efflux of amino-FAZA-GH could explain the non-trapping of [^{18}F]FAZA in hypoxic tissue and hence the estimation of non-zero β with kinetics modelling. Since k_4 and distribution volume were comparatively larger for normal than cancerous tissue, it is likely that more amino-FAZA-GH was effluxing out of the normal tissue leading to higher tracer accumulation and contrast between tumor and normal tissue in SUV imaging. As suggested by Masaki et al., NI based tracers may be imaging a complex processes involving nitroreductase, glutathione, and MRP-1 mediated efflux activity[34]. The tracer, [^{18}F]FAZA could be used to monitor MRP-1 activity and glutathionylation; hence could lead to personalization of treatment protocol by boosting radiation treatment in high hypoxic region and possibly treating high k_4 pancreatic cancer with MRP-1 blockers. This hypothesis warrants further investigation with more patients.

The major drawback of this study is that normal tissue from six patients could not be contoured due to tissue atrophy. The image derived AIF was not corrected for radio-metabolites which could introduce error in the estimation of kinetic parameters. With a complete set of normal data, the sensitivity and specificity could improve. The measurement of oxygen partial pressure in the tumor of this group of patients was not done as the approved ethics protocol did not include this invasive procedure. Nevertheless, pancreatic glands in PCa are surrounded by dense desmoplastic reaction for the survival of the cancer cells [40]. The high sensitivity (95%) in distinguishing the tumor from normal tissue agrees with the current view that pancreatic tumor is highly hypoxic due to this prevalent desmoplasia and the tracer $[^{18}F]FAZA$ is a specific substrate for nitroreductase in hypoxic cells. Furthermore, normal tissue neighbouring PCa may be relatively hypoxic compared to that in normal pancreas owing to the dense mass of fibrogen and collagen from desmoplasia. This could explain the low specificity observed in separating tumor from normal tissue.

3.5 Conclusion

We have developed the flow modified two tissue compartment (F2TC) model to analyze the kinetics of the hypoxic tracer $[^{18}F]FAZA$ kinetics in pancreatic cancer. Using the F2TC model, the estimated distribution volume (DV) and dissociation rate constant (k_4) of the tracer were able to distinguish pancreatic cancer from normal tissue with high sensitivity (95%) and high negative predictive value (89%). Our result also showed that $[^{18}F]FAZA$ was not irreversibly trapped in the putative hypoxic pancreatic cancer cells because the glutathione conjugated nitroreductase reduced product can exit hypoxic cells via the MRP-1 efflux pump.

3.6 References

1.   Canadian Cancer Statistics Advisory Committee. Canadian Cancer Statistics Special topic: HPV Associated Cancers. Canadian Cancer Society. doi:0835-2976

2.   The American Cancer Society Medical and Editorial Content Team. Lifetime Risk of Developing or Dying From Cancer. American Cancer Society. https://www.cancer.org/cancer/cancer-basics/lifetime-probability-of-developing-or-dying-from-cancer.html#written_by. Published 2018. Accessed October 1, 2014.

3.   Facts and Figures 2018. American Cancer Society. https://www.cancer.org/cancer/pancreatic-cancer/about/key-statistics.html#references. Published 2018.

4.   Koong AC, Mehta VK, Quynh T Le, et al. Pancreatic Tumors Show High Levels of Hypoxia. *Int J Radiat Oncol Biol Phys*. 2000;48(4):919-922.

5.   Chen M, Xue X, Wang F, et al. Expression and promoter methylation analysis of ATP-binding cassette genes in pancreatic cancer. *Oncol Rep*. 2012;27(1):265-269. doi:10.3892/or.2011.1475

6.   Brown JM, Wilson WR. Exploiting tumour hypoxia in cancer treatment. *Nat Rev Cancer*. 2004;4(6):437-447. doi:10.1038/nrc1367

7.   Piert M, Kumar P, Wiebe LI, Schwaiger M. Hypoxia-Specific Tumor Imaging with 18F-Fluoroazomycin Arabinoside. 2016;46(1):106-114.

8.   Peeters SGJA, Zegers CML, Lieuwes NG, et al. A comparative study of the hypoxia PET tracers [18F]HX4, [18F]FAZA, and [18F]FMISO in a preclinical tumor model. *Int J Radiat Oncol Biol Phys*. 2015;91(2):351-359. doi:10.1016/j.ijrobp.2014.09.045

9.   Nunn A, Linder K, Strauss HW. Nitroimidazoles and imaging hypoxia. *Eur J Nucl Med*. 1995;22(3):265-280. doi:10.1007/BF01081524

10.   Lopci E, Grassi I, Chiti A, et al. PET radiopharmaceuticals for imaging of tumor hypoxia: a review of the evidence. *Am J Nucl Med Mol Imaging*. 2014;4(4):365-384. doi:10.1038/bjc.2014.610

11.   Krohn KA, Link JM, Mason RP. Molecular imaging of hypoxia. *J Nucl Med*. 2008;49:129S-148S. doi:10.2967/jnumed.110.075663

12.   Asano A, Ueda S, Kuji I, et al. Intracellular hypoxia measured by 18F-fluoromisonidazole positron emission tomography has prognostic impact in patients with estrogen receptor-

positive breast cancer. *Breast Cancer Res*. 2018;20(1):1-8. doi:10.1186/s13058-018-0970-6

13. Oliveira IM De, Bonatto D, Antonio J, Henriques P. Nitroreductases : Enzymes with Environmental , Biotechnological and Clinical Importance. *Curr Res Technol Educ Top Appl Microbiol Microb Biotechnol*. 2010:1008-1019.

14. Masaki Y, Shimizu Y, Yoshioka T, et al. The accumulation mechanism of the hypoxia imaging probe "fMISO" by imaging mass spectrometry: Possible involvement of low-molecula metabolites. *Sci Rep*. 2015;5(July):1-9. doi:10.1038/srep16802

15. Koder RL, Haynes CA, Rodgers ME, Rodgers DW, Miller AF. Flavin thermodynamics explain the oxygen insensitivity of enteric nitroreductases. *Biochemistry*. 2002;41(48):14197-14205. doi:10.1021/bi025805t

16. Edwards DI. Nitroimidazole drugs--action and resistance mechanisms. I. Mechanisms of action. *J Antimicrob Chemother*. 1993;31(1):9-20. doi:10.1093/jac/31.1.9

17. Ang CW, Jarrad AM, Cooper MA, Blaskovich MAT. Nitroimidazoles: Molecular Fireworks That Combat a Broad Spectrum of Infectious Diseases. *J Med Chem*. 2017;60(18):7636-7657. doi:10.1021/acs.jmedchem.7b00143

18. Willemsen ATM, Hoff J van den. Fundamentals of quantitative PET data analysis. *Curr Parmaceutical Des*. 2002;8(16):1513-1526.

19. Thorwarth D, Eschmann SM, Paulsen F, Alber M. A kinetic model for dynamic [18F]-Fmiso PET data to analyse tumour hypoxia. *Phys Med Biol*. 2005;50(10):2209-2224. doi:10.1088/0031-9155/50/10/002

20. Lawrence KS St., Lee T-Y. An Adiabatic Approximation to the Tissue Homogeneity Model for Water Exchange in the Brain: II. Experimental Validation. *J Cereb Blood Flow Metab*. 1998;18(12):1378-1385. doi:10.1097/00004647-199812000-00012

21. Shi K, Souvatzoglou M, Astner ST, et al. Quantitative assessment of hypoxia kinetic models by a cross-study of dynamic 18F-FAZA and 15O-H2O in patients with head and neck tumors. *J Nucl Med*. 2010;51(9):1386-1394. doi:10.2967/jnumed.109.074336

22. Verwer EE, van Velden FHP, Bahce I, et al. Pharmacokinetic analysis of [18F]FAZA in non-

small cell lung cancer patients. *Eur J Nucl Med Mol Imaging*. 2013;40(10):1523-1531. doi:10.1007/s00259-013-2462-3

23. Logan J. Graphical analysis of PET data applied to reversible and irreversible tracers. *Nucl Med Biol*. 2000;27(7):661-670. doi:10.1016/S0969-8051(00)00137-2

24. Patlak CS, Blasberg RG, Fenstermacher JD. Graphical evaluation of blood-to-brain transfer constants from multiple-time uptake data. *J Cereb Blood Flow Metab*. 1983;3(1):1-7. doi:10.1038/jcbfm.1983.1

25. Metran-Nascente C, Yeung I, Vines DC, et al. Measurement of Tumor Hypoxia in Patients with Advanced Pancreatic Cancer Based on 18F-Fluoroazomyin Arabinoside Uptake. *J Nucl Med*. 2016;57(3):361-366. doi:10.2967/jnumed.115.167650

26. Taylor E, Gottwald J, Yeung I, et al. Impact of tissue transport on PET hypoxia quantification in pancreatic tumours. 2017;7:101. doi:10.1186/s13550-017-0347-3

27. Logan J, Fowler JS, Volkow ND, Ding YS, Wang GJ, Alexoff DL. A strategy for removing the bias in the graphical analysis method. *J Cereb Blood Flow Metab*. 2001;21(3):307-320. doi:10.1097/00004647-200103000-00014

28. Meier P, Zierler KL. On the theory of the indicator-diliution method for measurement of blood flow and volume. *J Applied Physiol*. 1954;6(12):731-744.

29. Mintun MA, Raichle ME, Kilbourn MR, Wooten GF, Welch MJ. A quantitative model for the in vivo assessment of drug binding sites with positron emission tomography. *Ann Neurol*. 1984;15(3):217-227. doi:10.1002/ana.410150302

30. Gunn RN, Lammertsma AA, Hume SP, Cunningham VJ. Parametric imaging of ligand receptor binding in PET using a simplified reference region model. *Neuroimage*. 1997;6:279-287.

31. Altman DG, Bland JM. Measurement in Medicine: The Analysis of Method Comparison Studies. *Stat*. 1983;32(3):307. doi:10.2307/2987937

32. Thie J. Clarification of fractional uptake concept. *J Nucl Med*. 1995;36(4):711-712.

33. Masaki Y, Shimizu Y, Yoshioka T, et al. Imaging mass spectrometry revealed the accumulation characteristics of the 2-nitroimidazole-based agent "pimonidazole" in

hypoxia. *PLoS One*. 2016;11(8):1-11. doi:10.1371/journal.pone.0161639

34. Masaki Y, Shimizu Y, Yoshioka T, et al. FMISO accumulation in tumor is dependent on glutathione conjugation capacity in addition to hypoxic state. *Ann Nucl Med*. 2017;31(8):596-604. doi:10.1007/s12149-017-1189-9

35. Shimizu Y, Zhao S, Yasui H, et al. A Novel PET Probe "[18F]DiFA" Accumulates in Hypoxic Region via Glutathione Conjugation Following Reductive Metabolism. *Mol Imaging Biol*. 2018:1-8. doi:10.1007/s11307-018-1214-y

36. Shen H, Paul S, Breuninger LM, et al. Cellular and in vitro transport of glutathione conjugates by MRP. *Biochemistry*. 1996;35(18):5719-5725. doi:10.1021/bi960098n

37. König J, Hartel M, Nies AT, et al. Expression and localization of human multidrug resistance protein (ABCC) family members in pancreatic carcinoma. *Int J Cancer*. 2005;115(3):359-367. doi:10.1002/ijc.20831

38. O'Driscoll L, Walsh N, Larkin A, Ballot J, Ooi WS. MDR1 / P-glycoprotein and MRP-1 Drug Efflux Pumps in Pancreatic Carcinoma. *Anticancer Res*. 2007;27:2115-2120.

39. Cao D, Qin S, Mu Y, Zhong M. The role of MRP1 in the multidrug resistance of colorectal cancer. *Oncol Lett*. 2017;13(4):2471-2476. doi:10.3892/ol.2017.5741

40. Pandol S, Edderkaoui M, Gukovsky I, Lugea A, Gukovskaya A. Desmoplasia of Pancratic Ductal Adenocarcinoma. *Clin Gastroenterol Hepatol*. 2009;7(110):S44-S47.

Chapter 4

4 Plasma Radio – metabolite analysis of PET tracers for dynamic PET imaging: TLC and autoradiography

4.1 Introduction

To derive molecular/metabolic information from dynamic PET, a kinetic analysis of the radiolabeled tracer is required. Obtaining the time concentration curve of the radiotracer in blood plasma, the arterial input function (AIF), is crucial to accurately portray the pathophysiology. One frequently used method is to sample arterial blood serially and use a radiation detector to measure the activity in the blood samples. The detector only detects the annihilation photons from the decaying positron-emitting isotope and cannot distinguish whether the radionuclide remains attached to the parent tracer or its metabolites[1]. AIF can be image derived obtained by measuring the activity in the arterial region in dynamic PET. Regardless of the method, measuring the activity in blood could overestimate the AIF because of the metabolite activity. Without correcting for the metabolite activity, results from kinetic analysis based on the overestimated AIF would be erroneous.

The metabolites can be separated from the parent tracer using chromatographic technique like thin layer chromatography (TLC), solid–phase extraction (SPE), or high performance liquid chromatography (HPLC)[2,3]. A rapid separation method, SPE techniques require a high amount of manual manipulation, which may pose a safety hazard from routine use. They can also be used to purify samples before they are submitted to HPLC for further analysis[4]. HPLC is widely used in analytical chemistry and pharmaceutical industry and research to determine the purity of samples. It has high resolution between metabolites and parent tracer with high sensitivity in radioactivity detection due to the use of a scintillation detector coupled with a photo-multiplier tube[5]. However, as a serial analyzer, HPLC can only analyze one sample at a time which can take up to 20 min for each sample. These instruments rely on finely tuned pumps, sensitive detectors, and various separation media. This results in high initial purchasing and upkeep costs. Preparing plasma samples for

HPLC analysis can be labor intensive and exposes personnel to additional ionizing radiation. Finally, HPLC separation is susceptible to impurities in the solvent mobile phases[1].

An economical alternative to HPLC is TLC which is a simpler version of HPLC. It is not susceptible to impurities and multiple samples can be analyzed at the same time. The major drawbacks are that TLC suffers from poorer analyte resolution and requires a very sensitive detector to detect analytes at low concentration on the TLC plate. Different techniques have been developed in the past for radio-TLC. Earlier techniques include the zonal analysis[6] and autoradiography technique where the TLC plate is directly exposed to x-ray film[7]. Later, radio-scanners were developed that measured radioactivity at $1 - 2$ mm steps. These techniques have poor analyte resolution (albeit from the intrinsic TLC characteristics), low sensitivity (MBq/mL range), and usually require long exposure time from hours to months for low activity samples and are prone to error[5,7]. Therefore, our objective was to explore a different detection system with improved sensitivity and time efficiency for radio-TLC.

4.2   Materials and Methods

4.2.1   Beaver autoradiography system

Beaver autoradiography (ai4r, France) is a multimodality real time digital autoradiography system that can image beta and alpha particles[8]. The detector is based on the principle of micro pattern gaseous (Ne + 10% CO_2) detector (MPGD). The one we used was designed for imaging large samples with high spatial resolution of 50µm (high energy beta and beta plus) and sensitivity of 5×10^{-4} cpm.mm^{-2} [9]. The detector is comprised of two drift zones alternating with two amplification zones separated by nickel micromeshes (Figure 4.1). The special feature of the drift zone is the low electric field (1kV/cm) that guides the electrons from the site of ionization by beta particles from radionuclide decay into the amplification zone[10]. Electrons are multiplied by avalanche effect in the amplification zone due to kinetic energy imparted by the high electric field. The amplification zones are shallow in depth (50µm) to limit the spread of electron avalanche (cloud) and hence improve spatial resolution[11]. The TLC plate is used as the cathode of the detector and serves

Figure 4-1 Schematic diagram of Beaver autoradiography detector system
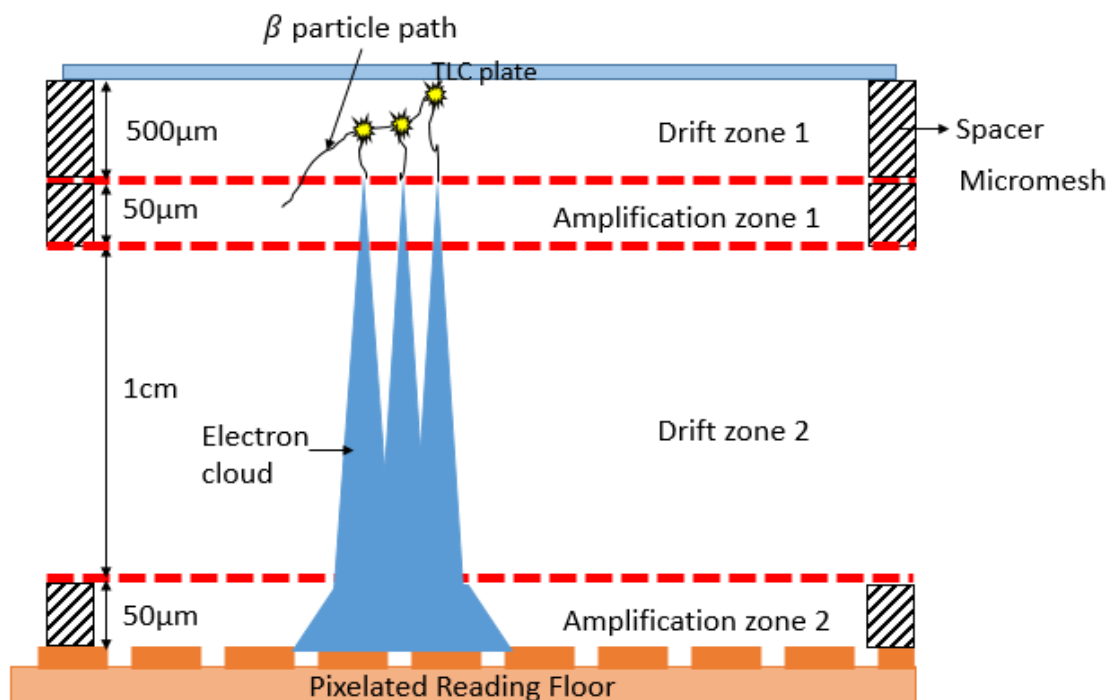
Working principle of Beaver MPGD for β- particle (adapted from *J Instrum. 2009; 4:1-9*[11])

as the back end of the first drift zone to prevent back flux of electrons. The electron cloud exiting the second amplification zone is captured by the pixelated reading anode.

4.2.2   Animal protocol

All experimental procedures were approved by and performed in accordance with guidelines from institutional animal ethics committee. Five farm pigs were procured from a farm nearby and two athymic Rowett Nude (RNU) rats were purchased from Charles River (Saint Constant, Quebec, Canada). The C57BL/10J mouse used in optimization of [18F]FEPPA mobile phase was purchased from Jackson Laboratory (Maine, USA). The animals were under no dietary restriction with free food access before each experiment. Pigs were first anesthetized with Telazole intramuscular injection (1 mL/kg) while rats and mouse by masking with 5% isoflurane, and maintained using isoflurane at 2-3% balanced oxygen and medical air. Pigs (33.7 ± 9.33 kg) were used for [18F]FEPPA (21.9 ± 6.34

MBq/kg) analysis. [^{18}F]FEPPA rats (309.75 ± 29.64 g) were used for [^{18}F]FAZA (49.54 ± 9.39 MBq/kg) analysis. The tracers were manufactured at the cyclotron/radiochemistry facility of our institution following published procedures [12,13]. Blood samples were drawn at 8 time points post tracer injection (p.i.) – 5, 10, 15, 20, 30, 40, 50 and 60 min. Each rat underwent two blood draws, two weeks apart, to make up a total of 4 sets of rat blood samples. For rats, blood (0.2 mL) was drawn for each sample from a tail artery using heparinized syringe into plasma separator tube. Due to the larger total blood volume of pigs, 2mL of blood was drawn for each sample from a cephalic vein into EDTA coated tubes.

4.2.3   Blood preparation for metabolite analysis

The blood samples were immediately placed on ice to prevent further catabolism. Within 1-2 min after the last sample was taken, all samples were centrifuged at 1,000G in Sero-fuge II centrifuge (Clay-Adams Company, Inc.) for 5 minutes. The supernatant plasma was aspirated for radio-metabolite analysis.

4.2.4   Thin Layer Chromatography (TLC) preparation

Silica coated TLC plates with F$_{254}$ fluorescent indicator were purchased from MilliporeSigma. Each plate was scored to a height of 9 cm to fit the 13x9 cm holder of the Beaver TLC detector. Blood plasma (2 µL) from each blood sample was spotted 1 cm from the bottom of the plate with a micropipette. For optimal use of each imaging session with the TLC detector, two 5 cm wide plates were used. Five samples including one parent tracer reference (0.11 – 0.30 MBq in 3 – 5 mL of isotonic saline) can be spotted on each plate. The plate was air dried after spotting then immersed into the mobile phase in a beaker, making sure the solution was less than 5 mm high. The beaker was then covered with parafilm wax paper. The TLC plate developed for approximately 15 minutes until the solvent (mobile phase) front was roughly 1cm from the top of the plate. The plate was then removed, air dried, and imaged with the autoradiographic detector for 4 h.

4.2.5 Optimization of the mobile phase

Using different volume fractions of ethyl acetate, methanol, and hexane, the mobile phase was optimized for each tracer. The solution that allowed the least polar analyte to migrate furthest away from the spotting baseline as well as giving a good separation of the metabolites from the unmodified tracer in the autoradiography image was selected as optimized solution. Due to poor analyte resolution with TLC, the plasma metabolites did not appear as discrete spots. [^{18}F]FEPPA and [^{18}F]FAZA were optimized with blood from a mouse and a human volunteer respectively, drawn at 90 min and 60 min p.i. respectively. In this study, with the optimized mobile phase (solvent), the parent tracer was always closest to the solvent front after the TLC plate was developed.

4.2.6 Image analysis

Autoradiography images were analyzed with Analyze 12.0 (Analyze Software System). Line profiles were generated by summing the detected counts in a 7 mm segment centered on the sample "track" at 10 mm intervals.

For line profiles where the adjacent metabolite peak overlapped with the parent tracer peak, the area underneath the latter was estimated with a custom developed program using MATLAB (The MathWorks, Inc.). These line profiles were fitted with two Gaussian functions. The parent tracer peak area was determined as the area of the fitted Gaussian between the limits of $\mu \pm 1.96\,\sigma$, where μ is the mean and σ is the standard deviation. For spots where the adjacent metabolite peak did not overlap with the parent tracer peak, the latter was fitted with a Gaussian function and the parent tracer peak area was similarly determined as for the case of overlap.

The fraction of the parent tracer was calculated using the formula:

$$fraction = \frac{Area\ under\ native\ tracer}{Total\ area\ under\ line\ profile}$$

Each estimated parent tracer fraction for different times p.i. was compared to published literature values for validation.

4.2.7 Effect of radio-metabolites on kinetic parameter estimation

The kinetic parameters associated with the tracer uptake are obtained by deconvolving the AIF of the parent tracer from the measured tissue concentration curve or tissue time activity curve (TAC). A simulation study was performed to observe the effect of blood plasma radio-metabolites in the estimation of kinetic parameters. For simulating the tissue TAC, our in-house flow modified two compartment (F2TC) model [14] that models the bi-directional permeation of the endothelial barrier during the transit time of the tracer through blood vessels, was utilized. The flow scaled impulse residue function (IRF$_F$(t)) for the model is expressed as:

$$IRF_F(t) = \begin{cases} F & 0 \le t < W \\ Ge^{-\alpha(t-W)} + He^{-\beta(t-W)} & t \ge W \end{cases}$$

where F is the blood flow, W is the mean transit time through blood vessels and G, H, α and β are the fitting parameters obtained by iteratively fitting tissue TAC with non-linear 'interior point' optimization technique. The model's explicit parameters can be calculated from the fitting parameters as follows:

$$K_1 = G + H; \quad k_2 = \frac{G\alpha + H\beta}{G + H}$$

$$k_3 = \frac{GH(\alpha - \beta)^2}{(G + H)(G\alpha + H\beta)}; \quad k_4 = \frac{(G + H)\alpha\beta}{(G\alpha + H\beta)} = \frac{\alpha\beta}{k_2}$$

The explicit parameters are the influx (K_1) and efflux (k_2) rate constant of tracer through the blood tissue barrier and k_3 and k_4 are the binding and disassociation rate constant of the parent tracer to and from the target respectively.

The measured AIF with metabolite contamination, AIF$_m$ was simulated using Feng's model [15,16]:

$$AIF_m(t) = [A_1(t - t_0)^\alpha - A_2 - A_3]e^{-\lambda_1(t-t_0)} + A_2e^{-\lambda_2(t-t_0)} + A_3e^{-\lambda_3(t-t_0)}$$

where $A_1 = 800, \alpha = 1.0, \ A_2 = 20, A_3 = 20, \lambda_1 = 4 \ min^{-1}, \lambda_2 = 0.015 \ min^{-1}, \lambda_3 = 0.15 \ min^{-1}, t_0 = 0.15 \ min$

AIF$_m$ was simulated at 0.5 s and corrected for radio-metabolite by multiplying with the fraction of parent [^{18}F]FEPPA measured in §3.4:

$$AIF_c = AIF_m * fraction$$

The corrected AIF$_C$ was used to simulated tissue TAC at 0.5 s with ten sets of parameters (Table 4.1) from patients with high grade glioma [17]. All the curves were frame averaged according to the

Table 4.1: Ten parameter sets used for simulating the effect of radio-metabolite correction in blood plasma

SET#	K_1 (mL·min^{-1}·g^{-1})	k_2 (min^{-1})	k_3 (min^{-1})	k_4 (min^{-1})	F (mL·min$^-$	W (s)	V_p (mL·g^{-1})	DV (mL.g$^-$
1	0.0930	0.5920	0.1840	0.0410	0.37	7	0.043	0.8621
2	0.1370	0.3310	0.2300	0.0700	0.27	7	0.032	1.7738
3	0.0740	0.3440	0.1520	0.0370	0.10	10	0.016	1.0988
4	0.0720	0.4580	0.2880	0.0770	0.29	10	0.048	0.7452
5	0.2220	0.4720	0.1900	0.0870	0.44	5	0.037	1.4975
6	0.1940	0.3280	0.2830	0.1720	0.26	15	0.065	1.5646
7	0.0960	1.0000	0.3060	0.0670	0.38	8	0.051	0.5344
8	0.1010	0.5180	0.3510	0.0750	0.20	10	0.034	1.1075
9	0.4790	1.0000	0.2210	0.1370	0.64	10	0.106	1.2517
10	0.2180	0.4980	0.4480	0.0840	0.87	15	0.218	2.7724

following frame schedule: 10 @ 10 s, 5 @ 20 s, 4 @ 40 s, 4 @ 60 s, 11 @ 180 s and 1@ 120 s (total 45 min). The two sets of kinetic parameters estimated by deconvolving AIF$_m$ and AIF$_c$ from simulated tissue TACs were compared. The difference of the parameters estimated with and without metabolite correction was tested for statistical significance using non-parametric test – either Wilcoxon signed rank or sign test depending on whether the distribution of the differences was symmetric or non-symmetric, respectively. P<0.05 was declared significant with Bonferroni correction for multiple comparison with 8 parameters (K_1, k_i $(i = 2,3,4), V_p, DV, W, K_i$).

Figure 4-2: Optimization of mobile phase for [^{18}F]FAZA and [^{18}F]FEPPA
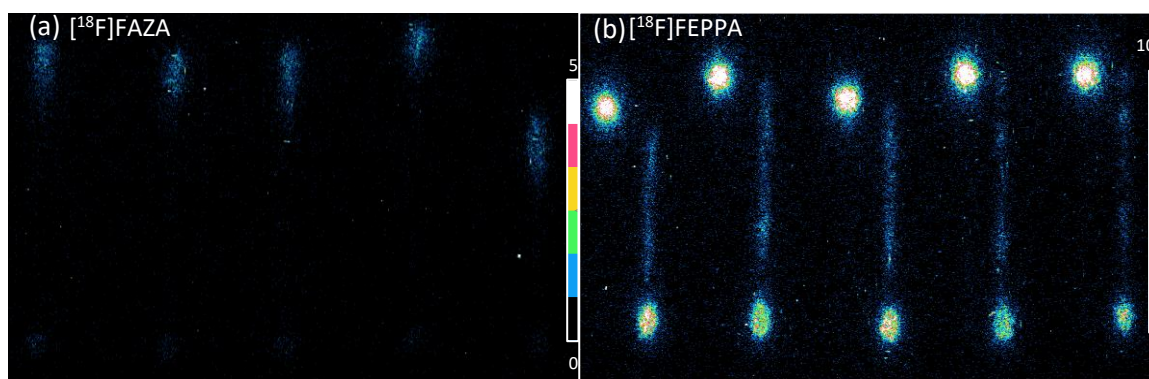
Mobile phase optimization for (a) [^{18}F]FAZA and (b) [^{18}F]FEPPA in human and mouse blood respectively at 90 min and 60 min (respectively) post injection, using different fractions of methanol, ethyl acetate and hexane. For each tracer, five different mixtures were used. For [^{18}F]FAZA only blood samples were used while for [^{18}F]FEPPA each blood sample was paired with the native tracer in normal saline as the reference. The optimal mobile phase would spread the radio-metabolites along the entire lane and move the reference furthest from the spotting line. For [^{18}F]FEPPA the fourth solution from the left comprised of 8% methanol, 10% hexane and 82% ethyl acetate was optimal while for [^{18}F]FAZA, it was the third solution comprised of 7% methanol and 93% ethyl acetate.

4.3   Results

4.3.1   Optimization of the mobile phase

The separation of radio-metabolites in blood plasma with different mixtures of methanol, hexane and ethyl acetate for both tracers is shown in Figure 4.2. The optimized mobile phase for [^{18}F]FEPPA and [^{18}F]FAZA were 8% methanol and 10% hexane in ethyl acetate (v/v; fourth solution) and 7% methanol in ethyl acetate (v/v; third solution) respectively.

4.3.2   Autoradiography

Figure 4.3 shows the autoradiographic images obtained from TLC plasma metabolite analysis of [^{18}F]FAZA (rat) or [^{18}F]FEPPA (pig), respectively. Each image showed two TLC plates with the parent tracer in normal saline as reference on each, as well as plasma obtained at different times p.i.. Since the reference parent tracer spot moved the furthest

Figure 4-3: Autoradiographic image of TLC for [^{18}F]FAZA and [^{18}F]FEPPA
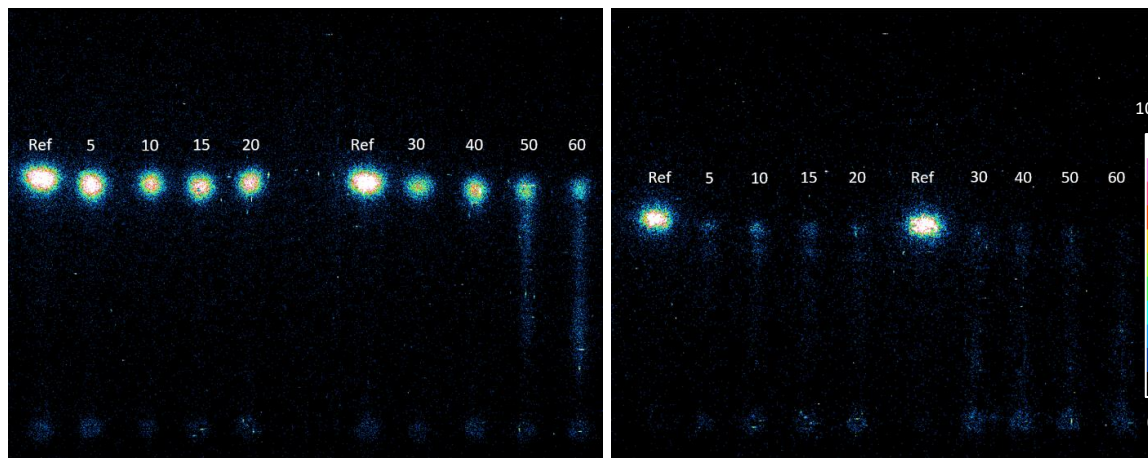
Autoradiography image of plasma samples obtained from a rat injected with [18F]FAZA (left) and from a pig injected with [18F]FEPPA (right). 'Ref' is the reference spot on each TLC plate. The number above each line shows the time in min at which the blood sample was drawn post tracer injection. The direction of motion of the mobile phase (solvent) front from capillary action was from bottom to top. The radio-metabolites that did not move with mobile phase show up as faint 'spots' at the bottom along the spotting line.

from the spotting baseline, it was the least polar analyte. The spots with similar retention factors (R_f) to the reference spots were the fractions of the parent tracer in plasma at different times p.i.. For [^{18}F]FAZA on the left, the reference spots' R_f was 0.66 ± 0.01 . Most of the activity was from the parent tracer while that at the spotting line could be from the more polar radio-metabolites. Significant conversion of tracer to radio-metabolite was observed from 50 min p.i.. For [^{18}F]FEPPA on the right, the reference spots' R_f was 0.54 $\pm$ 0. Radio-metabolites were observed as early as 5 min p.i. as indicated by activity directly below the reference R_f as well as activity along the spotting line. At 1 h p.i., the parent tracer spot almost disappeared as there was almost complete conversion into metabolites observed as activity all along the track.

4.3.3   Line profile

Figure 4.4 shows the line profiles of selected [^{18}F]FEPPA spots – reference, 5 min and 1 h p.i. – in the right image of Figure 4.3. For the reference, a well-defined peak was observed

Figure 4-4: Line profile of autoradiography image
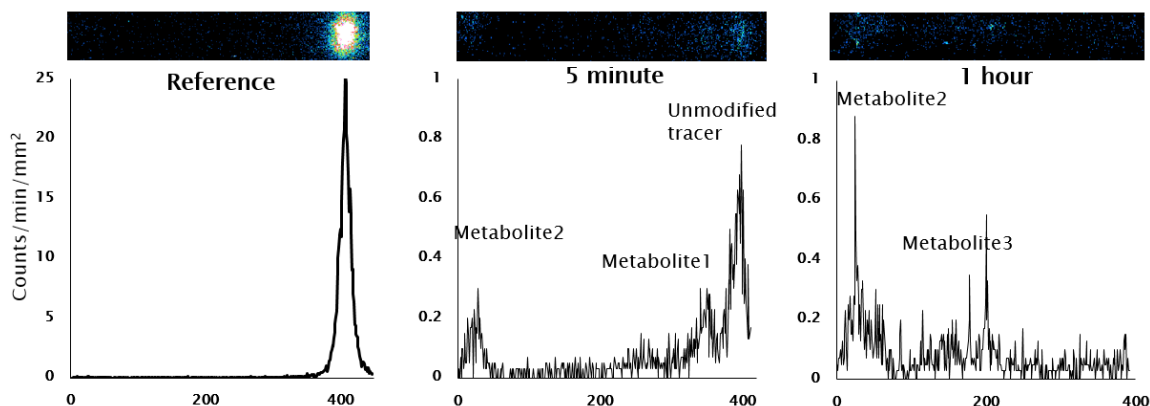
Line profile of [^{18}F]FEPPA reference, plasma from a pig obtained at 5 min and 1 h post tracer injection. The y-axis is detected counts and the x-axis is distance in mm. The corresponding autoradiography image is displayed above the profile. The direction of movement of the solvent front from capillary action was from left to right

due to high signal to noise ratio. At 5 min p.i., three prominent peaks were discernible. The peak on the furthest right was the parent [^{18}F]FEPPA, the peak for the least polar radio–metabolite was close to the parent tracer. The most polar radio-metabolite was located close to the spotting baseline. At 1 h p.i., the parent [^{18}F]FEPPA peak was not identifiable. A new peak corresponding to radio-metabolites of intermediate polarity was observed and the amount of the most polar radio-metabolite increased, as indicated by the area. Therefore, the parent [^{18}F]FEPPA was almost completely metabolized to radio-metabolites at 1 h p.i..

4.3.4   Fraction of parent tracer versus post-injection time

Figure 4.5 shows the fraction of parent [^{18}F]FAZA and [^{18}F]FEPPA in blood at different times post-injection (p.i.). For [^{18}F]FAZA, the fraction of parent tracer remained relatively constant at 91% until 40 min p.i. The fraction then decreased to 62% and 40% at 50 and 60 min p.i., respectively. On the other hand, close to 50% of activity in blood was from [^{18}F]FEPPA metabolites as early as 5 min p.i. and the parent tracer fraction decreased to 19% at 1 hour p.i. Table 4.2 shows the coefficient of variation (CoV) of the parent tracer

fraction arising from inter-subject variability. For [18F]FEPPA, CoV ranged from 0.07 to 0.43 while [18F]FAZA from 0.01 to 0.25.

4.3.5   Simulation study

Due to conversion of parent tracer to radio-metabolite, metabolite correction lowered the AIF as p.i. time increased (Figure 4.6(a)). When AIF_C was deconvolved from the tissue TACs, the parameters estimated were statistically different from those estimated by deconvolving AIF_m; errors greater than 32% were observed for all parameters (Table 4.3). The negative values indicate that values estimated by AIF_m is larger than those estimated by AIF_c.

Table 4.2: Coefficient of Variation of native tracer fraction for [18F]FEPPA and [18F]FAZA at eight time point post tracer injection

	5 min	10 min	15 min	20 min	30 min	40 min	50 min	60 min
[18F]FEPPA	0.07	0.13	0.17	0.17	0.24	0.32	0.26	0.43
[18F]FAZA	0.02	0.03	0.03	0.04	0.01	0.03	0.12	0.25

Figure 4-5: Fraction of parent tracer for [^{18}F]FAZA and [^{18}F]FEPPA

(a)

(B (b)
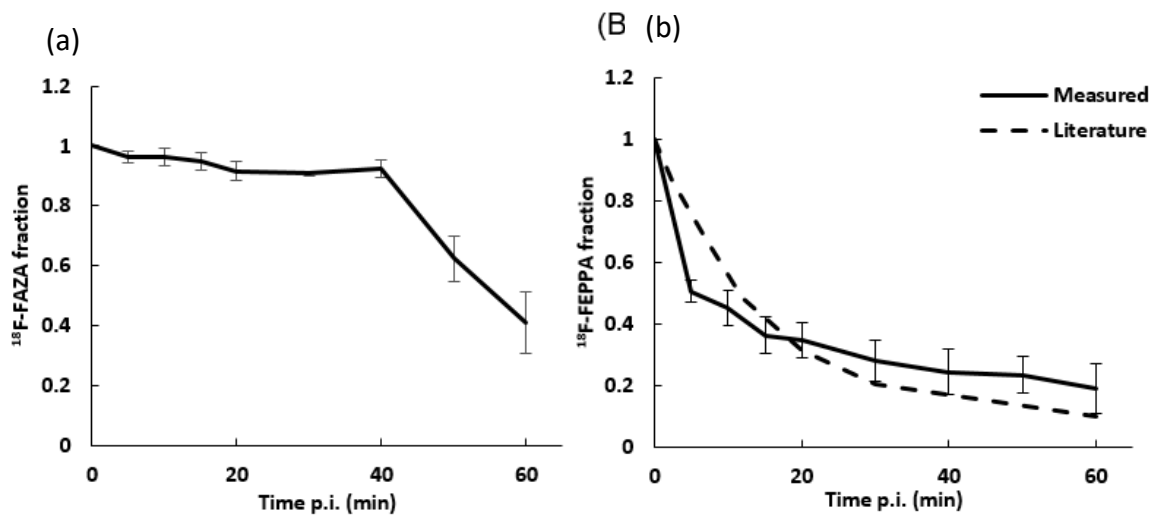
Native tracer fraction vs time post injection (p.i.) for (a) [^{18}F]FAZA and (b) [^{18}F]FEPPA. The dashed line in (b) is native tracer fraction from (18).The error bar corresponds to standard deviation for 5 pig blood samples ([^{18}F]FEPPA) and 4 rat blood samples ([^{18}F]FAZA)

4.4 Discussion

In this study, we established an alternate method to HPLC to determine the fraction of radio-labeled parent tracer at different times p.i. based on inexpensive TLC and a sensitive beta detector. Fraction of parent [^{18}F]FAZA and [^{18}F]FEPPA in normal healthy rats and pigs (respectively) p.i. were measured and compared to literature values, if available. There were large variations in the rate of metabolite production with the same tracer (either [^{18}F]FAZA or [^{18}F]FEPPA) and between the two tracers in the same and different animals. CoV of parent tracer fraction in blood could be as high as 43%. Since the mobile phase

Figure 4-6: Simulation curve for investigating the effect of radio-metabolite correction in blood plasma
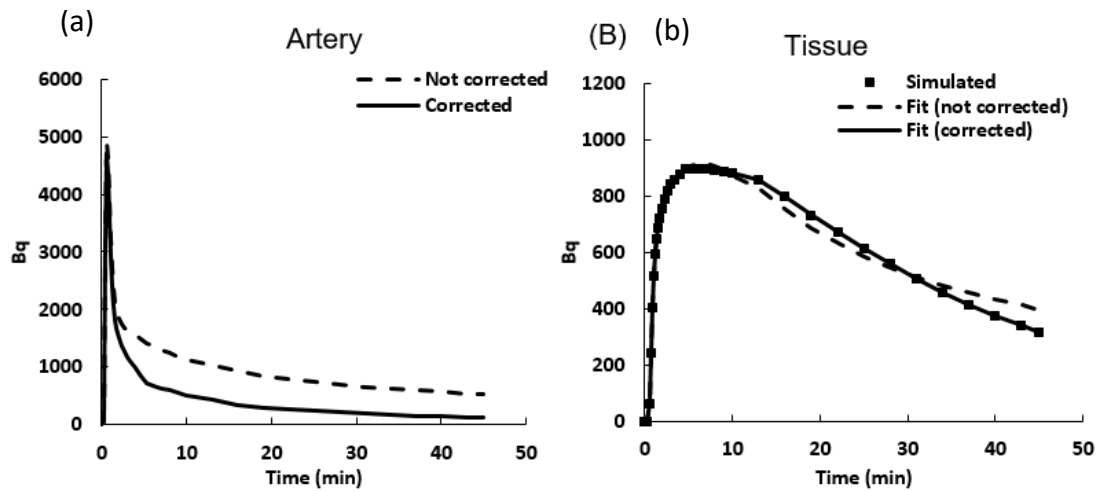
Curves utilized for simulating the effect of radio-metabolite on kinetic parameter estimation in dynamic PET cases. (a) Arterial curve simulated with Feng's model for measured (not corrected, dashed line) and radio-metabolite corrected curve (solid line). (b) Tissue curve simulated with parameter set #6 (table 4.1, solid square) and fitted curves obtained with measured arterial curve (dashed line) and with radio-metabolite corrected arterial curve (solid line).

optimization and the successful metabolite analyses were performed on different animal species as well as human subject, it showed that the mobile phase could be optimized in animals and transferred to human population. Furthermore, simulation study investigating the effect of radio-metabolite correction in measured arterial curve suggested that large error (30 – 400%) can result in the estimation of kinetic parameters if correction was not incorporated.

Table 4.3: Median differences between parameters in table 4.1 estimated using AIF with and without metabolite correction using [^{18}F]FEPPA fraction . P value is estimated by non-parameter test

Parameter	K_1 (mL·min^{-1}·g^{-1})	k_2 (min^{-1})	k_3 (min^{-1})	k_4 (min^{-1})	V_p (ml.g^{-1})	DV (ml.g^{-1})	W (min)
Median	-0.001	-0.118	0.105	-0.043	0.006	0.718	0.021
P	0.75	0.004	0.005	0.004	0.013	0.004	0.083
* Bias (%)	403	-32.0	51.0	-171	71.0	50.0	166

*Although the differences in the estimated parameters were not normally distributed, the percentage bias was used to approximate the expected error

The acquired autoradiography images showed clear distinction between radio-metabolites and the parent tracer. The large signal difference between reference and plasma sample was due to 6.7 times difference in the activity between the two. Reference [^{18}F]FEPPA (parent tracer in normal saline) was spotted with activity of 126 ± 17 Bq in 2 uL while plasma samples from pigs were lower in activity – at 5 min p.i. the activity was approximately 17 Bq in 2 uL. For our metabolite studies, either 15.2 ± 1.8 MBq (41–59MBq/kg) or 427 – 1216 MBq (13 – 27 MBq/kg) was administered for the rat ([^{18}F]FAZA) and pig ([^{18}F]FEPPA), respectively at the time of injection. These were lower than other published metabolite studies in mice where doses ranging from 20 – 30 MBq (1 GBq/kg) [18] to as high as 68 MBq (3.4 GBq/kg) [19] of tracer were administered due to the lower sensitivity of the radiation detector used. In our studies, even with >77 times less dose (normalized to body weight to account for the body mass of different species), peaks corresponding to the parent tracer could be distinguished from radio-metabolites. In the few cases where radio-metabolites overlapped with the parent tracer because of similar polarity and hence strength of adhesion to the silica media, the parent tracer peak could be adequately resolved by the curve fitting procedure discussed in §2.6. Taken the above results together, our method of combining TLC and the Beaver proprietary beta particle detector has the analyte resolution and sensitivity for blood metabolite determination for both [^{18}F]FAZA and [^{18}F]FEPPA in individual large (pig) or small (rodents) animals. Nevertheless, by comparing the [^{18}F]FEPPA dose used in our pig studies (13–27 MBq/kg)

to the published patient dose (2.5 – 6.2 MBq/kg [20–23]) the sensitivity of the detector has to be increased by at least 5 times for the method to be used for blood metabolite determination in individual patients.

From the [18F]FEPPA results (Table 4.2), inter-subject variation was observed with more pronounced variability at later time points p.i. This supports our view that the current practice of using a population average in normal subjects to correct for metabolite contamination [24] is not optimal for kinetic analysis and there is a need to determine blood metabolite in individual studies. HPLC is the most commonly used method to measure metabolite fraction in blood. It is a serial analyzer; samples are analyzed one at a time. Because multiple timed samples must be analyzed, HPLC is both labor intensive and time consuming if it is used to construct the metabolite fraction curve over ~ 60 min for each individual study. This limitation has resulted in the use of population based (even cross species) blood metabolite fraction for individual studies with the assumption that the inter-subject (inter-species) variability in metabolite production is negligible. As our study and other studies showed [20,24,25], inter-subject variabilities do exist invalidating the above assumption. In contrast, with our method, multiple samples can be analyzed together within one imaging session, the exact number of samples depends on the detector size. Currently, we can analyze 8 samples but with a larger detector size, the number of samples can be increased to 12 or more making it feasible for individualized radio-metabolite analysis.

The effect of not correctly accounting for blood radio-metabolite was investigated with computer simulation using a previously published kinetics model [14]. For all parameter sets listed in Table 4.1, the fitting to the simulated tissue time activity curve (TAC) failed when radio-metabolite contamination was not corrected for in the arterial TAC. This failure led to large errors (30 – 400%) in parameter estimation and possible misinterpretation of the tracer pharmacokinetics. For instance, distribution volume of [18F]FAZA is related to the amount and activity of nitroreductase present in hypoxic tissue [26] while that of [18F]FEPPA is related to density and activity of translocator protein (TSPO) found on the outer mitochondrial membrane [27], particularly within activated immune cells [28].

Our measured fractions of parent [18F]FEPPA in blood over time p.i. agreed well with those obtained by Rusjan et al.[20]. On the other hand, measured fractions of parent [18F]FAZA

over time p.i. were not found in literature. Studies of [^{18}F]FAZA by Verwer et al. showed that only 10% of the activity in blood was from metabolites at 70 min p.i. [22] with the use of solid phase extraction and HPLC. Our study showed that significant metabolite fraction (~ 10%) in blood started at 40 min and increased to 60% at 60 min p.i.. Jans et al [18] also used TLC to estimate the metabolite fraction in blood and no metabolite was observed. However, there were two mitigating factors with their experiments that could explain the difference in the measured metabolite fraction in blood. First, it was not known whether the mobile phase used was optimized for the tracer; second, the detector used may not be as sensitive as our one.

The time required for blood metabolite analysis using our method starting with the collected blood samples (excluding the image processing time) comprised of: 5 min of centrifugation, 5 min for spotting samples on and drying the TLC plate, and 15 minutes of TLC plate development for a total of 25 – 30 minutes. Technically, the solvent front is required to move beyond the furthest point the samples or the parent tracer moved during development. In our experiments, the parent tracer (either [^{18}F]FAZA or [^{18}F]FEPPA) which moved the furthest, moved approximately 4.5 cm while the solvent front moved over 7 cm. Therefore, the development time can be shortened to 10 min. The autoradiograph image was acquired over 4 h in this study. However, one–hour acquisition was tested, the acquired image showed good image quality (signal-to-noise ratio) as shown in the supplementary figure. Unlike HPLC where it occupies the operator's attention the entire time while the samples are analyzed, here the imaging (1 or 4 h) is completely operator independent.

In comparison, radio – HPLC takes approximately 10 min for each sample analyzed, not including sample preparation time. With multiple samples (say 8 samples as in this study), the total preparation time required could be over 80 min compared to 10 min with our method. Other comparative similarities and differences between our method and HPLC include the following. First, our method requires a smaller volume of plasma (2 μL) than HPLC. Sample volume required, ranging from 1 to 2000 µL, for HPLC depending on the size of the column [29]. Second, both requires the mobile phase to be optimized for each tracer. Third, inexpensive TLC plates can be used for all tracers but can be used only once

while different expensive HPLC columns may be required, one for each tracer but each column is reusable. Fourth, HPLC columns require regular washing to prevent clogging and to remove metabolites from previous runs which can cause residual memory issue[1,30]; these issues do not arise with TLC because a new inexpensive plate is used for each metabolite analysis run and TLC is less prone to impurities present in the solvent. Fifth, HPLC has superior analyte resolution than TLC which avoids potential overlapping of the parent tracer peak with that of metabolites. However, this overlap of peaks can be resolved by Gaussian fitting as discussed in §2.6. Since the chemical identity of the radio-metabolites is not required for metabolite fraction correction, this simple correction method is sufficient for our purpose. Finally, the Beaver autoradiography system is marginally more expensive than an HPLC, however, it is a multipurpose system with tissue slice imaging capabilities able to detect both α and β particles. Taking all the above comparative advantages and disadvantages of our method and HPLC into consideration, we conclude that our method is more suited for individualized metabolite measurement in blood than HPLC. Note that independent of whether the AIF is measured with timed arterial blood sample or is image derived by measuring the activity in an arterial region in dynamic PET images, metabolite correction is required.

There are several limitations with our study. The measured blood metabolite fraction was not validated against the reference HPLC method. However, our [^{18}F]FEPPA results agreed with literature values measured with reverse phase HPLC (Figure 4.6(b)). The number of blood samples used for each tracer was small. Even with this small number of animals, the inter-subject variability in metabolite fraction was prominent (Table 4.2) suggesting that this result could be the true *in vivo* situation and the importance to measure metabolite fraction for each individual subject. For this study, the plasma whole blood ratio was not taken into consideration which could introduce additional errors in kinetic parameter estimation. We investigated only two tracers, [^{18}F]FEPPA and [^{18}F]FAZA, as examples. Since analyte separation of TLC depends on the polarity of the tracer and its metabolites, for other tracers the mobile phase will have to be optimized. We have tested our method only with the ^{18}F radionuclide. Since other common PET radionuclides including ^{11}C, ^{13}N, ^{68}Ga and ^{89}Zr emit β^- particles in their decay, our method would also work except, like the

mobile phase, the limit of radioactivity detection must be determined for each radionuclide separately.

4.5 Conclusion

We were able to measure the fraction of parent radiolabeled tracer in blood after it was injected into the body using TLC and the Beaver autoradiography system. This fraction is required to correct the arterial input function (AIF) obtained by measuring the activity in timed arterial blood samples or in arterial region in dynamic PET images. Without this correction, the AIF will be overestimated leading to errors in the kinetic analysis of dynamic PET. Although we used two specific tracers, [^{18}F]FAZA and [^{18}F]FEPPA, to develop the method, the system can be used for other tracers by optimizing the mobile phase for each of them. Due to its capability to analyze multiple (>8) blood samples at the same time with preparation time as short as 25 – 30 min, our method will enable individualize blood metabolite correction for kinetic analysis of dynamic PET.

4.6   Supplementary figure

(a)   (b)
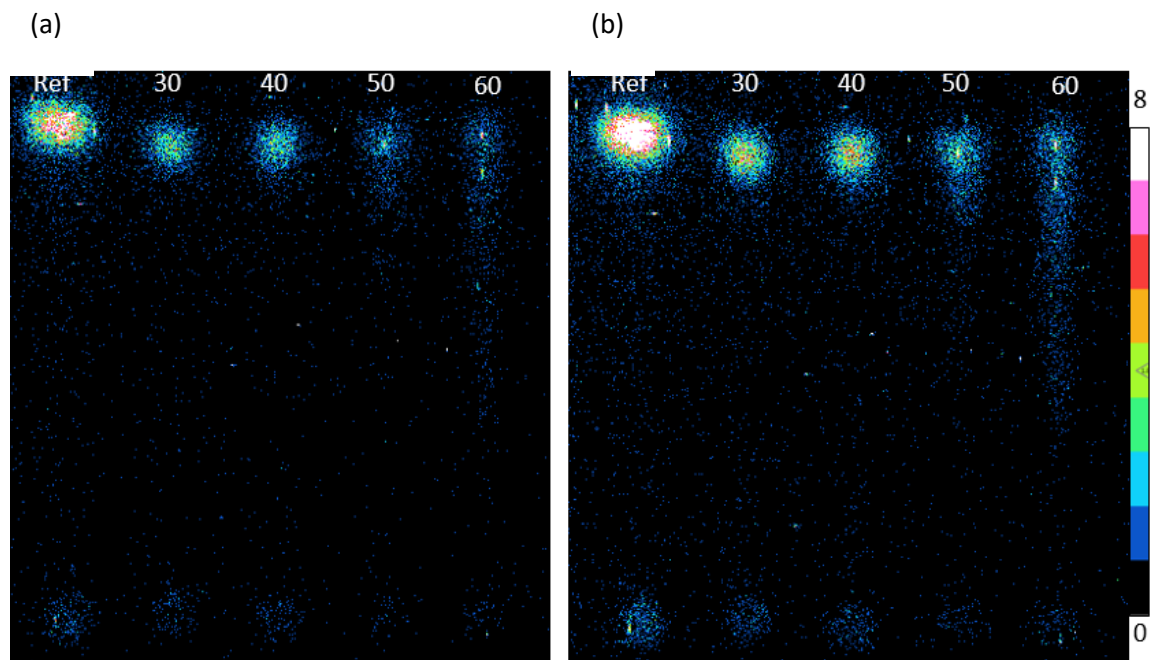
Beaver image of blood plasma obtained from a rat injected with ^{18}F-FAZA. The SNR of image (A) acquire for 1 hour is acceptable with discernible spots for native tracer and radio-metabolites. (B) The same TLC image that is acquired for four hours immediately after (A) was acquired. The bright spot is the reference 'ref' native tracer followed by blood samples drawn at 30, 40, 50 and 60 minute post injection.

4.7   References

1.   Pawelke B. Metabolite analysis in positron emission tomography studies: Examples from food sciences. *Amino Acids*. 2005;29(4 SPEC. ISS.):377-388. doi:10.1007/s00726-005-0202-0

2.   Wang RF, Loc'h C, Mazière B. Determination of unchanged [18F]dopamine in human and nonhuman primate plasma during positron emission tomography studies: A new solid-phase extraction method comparable to radio-thin-layer chromatography analysis. *J Chromatogr B Biomed Appl*. 1997;693(2):265-270. doi:10.1016/S0378-4347(97)00086-8

3.   Ma Y, Kiesewetter DO, Lang L, et al. Determination of [18F]FCWAY, [18F]FP-TZTP, and their metabolites in plasma using rapid and efficient liquid-liquid and solid phase extractions. *Nucl Med Biol*. 2003;30(3):233-240. doi:10.1016/S0969-8051(02)00452-3

4.   Robards K, Haddad PR, Jackson PE. *Principles and Practice of Modern Chromatographic Methods*. Academic Press; 1994.

5.   Takei M, Kida T, Suzuki K. Sensitive measurement of positron emitters eluted from HPLC. *Appl Radiat Isot*. 2001;55(2):229-234. doi:10.1016/S0969-8043(00)00392-4

6.   Snyder F, Cress E. Application of thin-layer chromatographic zonal 14C-Profile scans to the analysis of urinary constituents derived from lipds. *Clin Chem*. 1968;14(6):529-534.

7.   Marx AM, Kronberg H, Neuhoff V. Determination of the specific radioactivity of amino acids by a combination of thin-layer chromatography and quantitative autoradiography. *J Chromatogr*. 1987;393(19):407-417. doi:10.1017/CBO9781107415324.004

8.   Sardini P, Angileri A, Descostes M, et al. Quantitative autoradiography of alpha particle emission in geo-materials using the Beaver™ system. *Nucl Instruments Methods Phys Res Sect A Accel Spectrometers, Detect Assoc Equip*. 2016;833:15-22. doi:10.1016/j.nima.2016.07.003

9.   Ai4r. BeaQuant. http://www.ai4r.com/real-time-autoradiography/product/. Published 2017. Accessed January 31, 2020.

10.   Titov M. Perspectives of Micro-Pattern Gaseous Detector Technologies for Future Physics Projects. 2013:1-14. http://arxiv.org/abs/1308.3047.

11.   Donnard J, Arlicot N, Berny R, et al. Advancements of labelled radio-pharmaceutics imaging with the PIM-MPGD. *J Instrum*. 2009;4(11):1-9. doi:10.1088/1748-0221/4/11/P11022

12.   Wilson AA, Garcia A, Parkes J, et al. Radiosynthesis and initial evaluation of

[18F]-FEPPA for PET imaging of peripheral benzodiazepine receptors. *Nucl Med Biol*. 2008;35(3):305-314. doi:10.1016/j.nucmedbio.2007.12.009

13. Hayashi K, Furutsuka K, Takei M, et al. High-yield automated synthesis of [18F]fluoroazomycin arabinoside ([18F]FAZA) for hypoxia-specific tumor imaging. *Appl Radiat Isot*. 2011;69(7):1007-1013. doi:10.1016/j.apradiso.2011.02.025

14. Yang DM, Palma D, Louie A, et al. Assessment of tumour response after stereotactic ablative radiation therapy for lung cancer: A prospective quantitative hybrid 18 F-fluorodeoxyglucose-positron emission tomography and CT perfusion study. *J Med Imaging Radiat Oncol*. 2019;63(1):94-101. doi:10.1111/1754-9485.12807

15. Feng D, Huang S-C, Wang X. Models for computer simulation studies of input functions for tracer kinetic modeling with positron emission tomography. *Int J Biomed Comput*. 1993;32(2):95-110. doi:https://doi.org/10.1016/0020-7101(93)90049-C

16. Ben Bouallègue F, Vauchot F, Mariano-Goulart D. Comparative assessment of linear least-squares, nonlinear least-squares, and Patlak graphical method for regional and local quantitative tracer kinetic modeling in cerebral dynamic 18 F-FDG PET. *Med Phys*. 2019;46(3):1260-1271. doi:10.1002/mp.13366

17. Debus C, Afshar-Oromieh A, Floca R, et al. Feasibility and robustness of dynamic 18F-FET PET based tracer kinetic models applied to patients with recurrent high-grade glioma prior to carbon ion irradiation. *Sci Rep*. 2018;8(1):1-17. doi:10.1038/s41598-018-33034-5

18. Jans HS, Yang XH, Brocks DR, Kumar P, Wuest M, Wiebe LI. Positron emission tomography (PET) and pharmacokinetics: Classical blood sampling versus image-derived analysis of [18 F]FAZA and [18 F]FDG in a murine tumor bearing model. *J Pharm Pharm Sci*. 2018;21(1S):32s-47s. doi:10.18433/jpps29788

19. Vignal N, Cisternino S, Rizzo-Padoin N, et al. [18F]FEPPA a TSPO radioligand:

Optimized radiosynthesis and evaluation as a PET radiotracer for brain inflammation in a peripheral LPS-injected mouse model. *Molecules*. 2018;23(6). doi:10.3390/molecules23061375

20.   Rusjan PM, Wilson AA, Bloomfield PM, et al. Quantitation of translocator protein binding in human brain with the novel radioligand 18 F-FEPPA and positron emission tomography. *J Cereb Blood Flow Metab*. 2011;31(8):1807-1816. doi:10.1038/jcbfm.2011.55

21.   Mizrahi R, Rusjan PM, Vitcu I, et al. Whole Body Biodistribution and Radiation Dosimetry in Humans of a New PET Ligand, [18F]-FEPPA, to Image Translocator Protein (18 kDa). *Mol Imaging Biol*. 2013;15(3):353-359. doi:10.1007/s11307-012-0589-4

22.   Verwer EE, van Velden FHP, Bahce I, et al. Pharmacokinetic analysis of [18F]FAZA in non-small cell lung cancer patients. *Eur J Nucl Med Mol Imaging*. 2013;40(10):1523-1531. doi:10.1007/s00259-013-2462-3

23.   Savi A, Incerti E, Fallanca F, et al. First evaluation of PET-based human bioDistribution and dosimetry of 18F-FAZA, a tracer for imaging tumor hypoxia. *J Nucl Med*. 2017;58(8):1224-1229. doi:10.2967/jnumed.113.122671

24.   Hinz R, Bhagwagar Z, Cowen PJ, Cunningham VJ, Grasby PM. Validation of a tracer kinetic model for the quantification of 5-HT 2A receptors in human brain with [11C]MDL 100,907. *J Cereb Blood Flow Metab*. 2007;27(1):161-172. doi:10.1038/sj.jcbfm.9600323

25.   Henriksen G, Spilker M, Sprenger T, et al. Gender dependent rate of metabolism of the opiod receptor-PET ligand [18F]fluoroethydiprenorphine. *Nuklearmedizin*. 2006;45(5):197-200.

26.   Nunn A, Linder K, Strauss HW. Nitroimidazoles and imaging hypoxia. *Eur J Nucl Med*. 1995;22(3):265-280. doi:10.1007/BF01081524

27.   Anholt R, Pedersen P, De Souza E, Snyder S. The peripheral-type benzodiazepine receptor: localization to the mitochondrial outer membrane. *J Biol Chem*.

1986;261(2):576-583. doi:10.1097/00004850-199001000-00012

28. Veiga S, Carrero P, Perna O, Azcotta I, Garcia-Segura L. Translocator protein (18kDa) is involved in the regulation of reactive gliosis. *Glia*. 2007;55:1425-1436. http://www.unscn.org/en/home/.

29. Silicycle. Ideal injection volume vs column dimension. https://www.silicycle.com/ca/faq/hplc/ideal-injection-volume-vs-column-dimension. Published 2019. Accessed May 5, 2020.

30. Wilson ID. Thin-layer chromatography: A neglected technique. *Ther Drug Monit*. 1996;18(4):484-492. doi:10.1097/00007691-199608000-00030

Chapter 5

5   Conclusion

Understanding tumor physiology is important for targeted therapy. Some patients respond to certain therapy while others do not. One potential cause is the variations in tumor pathophysiology of each individual patient. With kinetic analysis of PET targeted tracer uptake over time, information on molecular pathways involved in tumor development and proliferation in individual patient can be obtained. Therefore, accurate kinetics modelling of targeted tracer distribution is important not only in the early diagnosis but also in the monitoring treatment response of cancer. The primary goal of this thesis is to develop a generic model for kinetic analysis of dynamic PET data acquired with targeted tracers which improves upon the standard two tissue compartment (S2TC) model.

In the following sections §1.1 − §1.3, summary of the thesis research work will be provided. Following the summary, potential future directions of research suggested by the completed research projects in this thesis will be discussed

5.1   Chapter 2 - Estimation of kinetic parameters for dynamic PET imaging: A simulation study

By assuming blood vessels as a compartment, the standard S2TC model models the delivery of tracer to the tissue following administration as instantaneously mixing uniformly with tracer already in the vessels as well as instantaneously wash-out of the vessels to the tissue. The developed flow modified two tissue compartment (F2TC) model overcome this non-physiological assumption by modelling blood vessels as a pipe with finite transit time from the arterial to venous end. During each tracer transit of blood vessels, the bidirectional permeation of tracer through the blood tissue barrier can introduce concentration gradient in the vessel, as a result the buildup of tracer in tissue is slower than instantaneous wash-out as assumed in the S2TC model. This delay would lead to error in estimating the rate constants governing the bidirectional permeation of the blood-tissue barrier as well as the rate constant of binding to and dissociation from the target.

The accuracy of kinetic parameters estimated by F2TC and the S2TC model were compared with computer simulation where the tracer uptake curve in the tissue was simulated using different sets of model parameters to mimic PET dynamic data including frame averaging, noise and limited data acquisition time. For the estimation of kinetic parameters based on the S2TC model, we also compared the performance of custom software and a commercially available software, PMOD. There was significantly less accuracy in the estimated model parameters for both S2TC model software than F2TC model, with PMOD performing the worst. As expected, the error was larger for higher noise level for all models/software. Concerning the length of acquisition time required for accurate parameter estimation, the F2TC model results show that 45 minute was comparable to 60 minute in the accuracy of estimated kinetic parameters and hence is sufficient for parameter estimation from dynamic PET. The acquisition time is dependent on the parameter set used and hence on the tracer. Due to the introduction of mean transit time in the blood vessels in the F2TC model, we investigated the effect of MTT from 5s to 20s. For the F2TC model, difference between the two MTT was not significant. However, with both S2TC software, increasing MTT introduced larger error. In addition, distribution volume estimated by F2TC model and S2TC model with the custom software was more accurate than Logan analysis or the PMOD software.

5.2   Chapter 3 - Pharmacokinetic analysis of dynamic [^{18}F]FAZA PET imaging in pancreatic cancer patient

Severe hypoxia in pancreatic ductal adenocarcinoma is a potential cause for its treatment resistance and hence low survival rate. The mechanism for hypoxia may differ individually, for instance, the rate of oxygen delivery via perfusion relative to rate of tissue (cells and stroma) aerobic respiration but can be measured with hypoxia tracer, [^{18}F]FAZA. It is currently believed that the tracer becomes trapped in the hypoxic cells after it is reduced by nitroreductase, which is active in reduced tissue oxygen content, to intermediate product. However, with our F2TC model also validated by the more generalizable graphical analysis, it was established that the tracer is reversibly bound which could be due to efflux of the reduced products by the multi-drug resistance protein -1 (MRP-1) after the intermediates were conjugated with glutathione. These efflux pumps has been shown to

be active in pancreatic tumor cells[1–3] . The same conclusion was observed with a study done by Masaki et al[4–6]. This proposition if proven true means that kinetic analysis using the developed F2TC model of dynamic PET data acquired with the tracer ($[^{18}F]$FAZA) can not only be used to monitor hypoxia through measuring nitroreductase activity but also MRP-1 activity through glutathionylation of the reduced products that contributes to treatment resistance.

Furthermore, kinetic parameters – dissociation rate constant (k_4) and distribution volume (DV) estimated by F2TC model can differentiate pancreatic tumor from normal pancreatic tissue with high sensitivity of 95% and negative predictive value of 89%. Specificity was lower at 57% due to the inability to correctly classify normal tissue as true negative. This failure could be due to ischemia in normal tissue caused by the dense desmoplasia in the neighboring tumor. With the S2TC model, only DV can classify the two tissue types with lower sensitivity of 90% and specificity of 43%.

5.3 Chapter 4 - Plasma radio-metabolite analysis of PET tracers for dynamic PET imaging: TLC and autoradiography

To accurately estimate kinetic parameters from dynamic PET, the native or unmodified tracer in blood plasma has to be measured. Correction for radio-metabolites in blood plasma remains a challenge, particularly, for each individual patient. Several techniques of separating radio-metabolites in the blood plasma have been described previously[8–10]. HPLC is the most widely used technique due to its superior analyte resolution. However, it is a serial analyzer which is not ideal for scaling up to deal with a large number of samples as will be required for plasma metabolite analysis for individual patients. To implement automatic analysis of a large number of plasma samples, an alternate technique is developed with the use of thin layer chromatography (TLC) which is more economical than HPLC along with a very sensitive Beaver autoradiography imaging system (ai4r France). The use of TLC in separating radio-metabolites from the native tracer is not novel in itself but the use of a beta particle detector based on the principle of micro pattern gaseous (Ne + 10% CO2) detector (MPGD) to detect the low radioactivity from the plasma radio-

metabolites makes the developed method novel. The MPGD detector has very high spatial resolution (~50μm) and high sensitivity[11].

The mobile phase for each tracer needs to be optimized due to their differences in polarity. In chapter 4, the mobile phase was optimized for two tracers, [18F]FAZA and [18F]FEPPA, using different fraction of ethyl acetate, methanol and hexane. TLC technique requires minute (2μL) amount of blood plasma, therefore this technique of radio-metabolite measurement could be employed for individual small animal dynamic PET studies. The MPGD detector was sensitive enough to detect radioactivity as low as 17Bq. The acquired images had good signal-to noise (SNR) with discernible peaks for the native tracer and radio-metabolites. Large variations in the plasma radio-metabolite fraction post injection of the native tracer were observed both within and between subjects. On average, [18F]FEPPA was metabolized as early as 5 minute post injection while significant catabolism of [18F]FAZA was observed only after 40 min post injection. The large intra- and inter-subject variations in metabolite fraction observed means that the current practice of using a population (even cross-species) average metabolite fraction to correct plasma activity may lead to erroneous kinetic analysis results for individual patients. Currently, 8 samples were measured in one imaging session but with larger detector size (available commercially) the number of samples that can be measured at once can be increased to more than 12. This makes translation into individualized plasma radio-metabolite fraction measurement a possibility.

5.4   Future work

This thesis has generated several hypotheses which could be future directions of research as discussed in the following:

5.4.1   Binding mechanism of nitroimidazole based tracers

Hypoxia imaging tracers, like [18F]FAZA, belong to the family of nitroimidazoles which allegedly are irreversible tracers because they become trapped in hypoxic cells after reduction of their nitro group[12]. Our results suggest that the reduced products are further processed by glutathionylation and the conjugated products are then effluxed out of

hypoxic cells via the MRP-1 pumps. This hypothesis was established by Masaki et al[4] for [^{18}F]FMISO, the first generation nitroimidazole-based hypoxia imaging tracer; and needs to be confirmed for the second generation [^{18}F]FAZA with further investigation. It would be of great interest to investigate if this hypothesis is generally applicable to all nitroimidazole-based tracers and to other solid tumors besides pancreatic tumor. Being the newer generation of hypoxia imaging tracer, [^{18}F]FAZA is more widely than [^{18}F]FMISO in tumor imaging, the establishment of its binding mechanism will assist in the personalization of cancer treatment protocol − boosting radiation dose to high hypoxic region and possibly treating pancreatic cancer with MRP-1 blockers (see next section).

5.4.2 Personalized treatment of pancreatic cancer

Another hypothesis generated from the study is that [^{18}F]FAZA can be used to monitor the activity of MRP-1. Specifically hypoxic tumors with upregulated expression and activity of MRP-1 could be identified by the measured dissociation rate constant (k_4) and be treated with MRP-1 inhibitor. MRP-1 inhibition has been investigated in the past for neuroblastoma and colorectal cancer[13–15]. It has been observed that anti-MRP1 inhibitors, reversan[15] and difloxacin[14], are effective in controlling tumor growth as well as sensitizing neuroblastoma to conventional chemotherapy. For colorectal cancer, nude mice implanted with 5-FU resistant tumor cell line transfected with MRP-1 knockdown, regained chemosensitivity to 5-FU and had their tumor growth inhibited compared with mice implanted with just 5-FU resistant tumor cell line[13]. For pancreatic cancer, a hydrophobic MRP-Pg chemosensitizer, Reversin R121 along with chemodrugs like 5-FU, cisplatin and gemcitabine significantly reduced the MRP-1 expression led to reduced peritoneal, hepatic and pulmonary metastasis[16]. A future study investigating the dose of MRP-1 inhibitors based on the estimated dissociation rate constant (k_4) and distribution volume (DV) from the F2TC model may prove personalization of treatment protocol is possible using dynamic PET with hypoxia imaging tracers.

5.4.3   Validation of radio-metabolite correction

Since polarity of each tracer and their metabolites differs, the mobile phase for other tracers will require optimization. The fraction of native ^{18}F-FAZA need to be verified with HPLC

analysis. Though the [^{18}F]FAZA dose injected into pigs was lower than what was currently been used for radio-metabolite studies, dose closer to patient dose need to be investigated for clinical translation. We observed that metabolism of [^{18}F]FAZA is slower than [^{18}F]FEPPA, with significant metabolite fraction only appearing at 40 minute post tracer injection. It would be important to investigate the cause behind this delayed catabolism of the native tracer. If the dominant source of catabolites is the tissue, the method of plasma radio-metabolite correction will differ from the case when the source is catabolism in the blood plasma.

5.5   References

1.   Chen M, Xue X, Wang F, et al. Expression and promoter methylation analysis of ATP-binding cassette genes in pancreatic cancer. *Oncol Rep*. 2012;27(1):265-269. doi:10.3892/or.2011.1475

2.   König J, Hartel M, Nies AT, et al. Expression and localization of human multidrug resistance protein (ABCC) family members in pancreatic carcinoma. *Int J Cancer*. 2005;115(3):359-367. doi:10.1002/ijc.20831

3.   O'Driscoll L, Walsh N, Larkin A, Ballot J, Ooi WS. MDR1 / P-glycoprotein and MRP-1 Drug Efflux Pumps in Pancreatic Carcinoma. *Anticancer Res*. 2007;27:2115-2120.

4.   Masaki Y, Shimizu Y, Yoshioka T, et al. FMISO accumulation in tumor is dependent on glutathione conjugation capacity in addition to hypoxic state. *Ann Nucl Med*. 2017;31(8):596-604. doi:10.1007/s12149-017-1189-9

5.   Masaki Y, Shimizu Y, Yoshioka T, et al. Imaging mass spectrometry revealed the accumulation characteristics of the 2-nitroimidazole-based agent "pimonidazole" in hypoxia. *PLoS One*. 2016;11(8):1-11. doi:10.1371/journal.pone.0161639

6.   Masaki Y, Shimizu Y, Yoshioka T, et al. The accumulation mechanism of the hypoxia imaging probe "fMISO" by imaging mass spectrometry: Possible involvement of low-molecula metabolites. *Sci Rep*. 2015;5(July):1-9. doi:10.1038/srep16802

7.   National Cancer Institute (NCI). Cancer Stat Facts: Pancreatic Cancer. NCI website.

https://seer.cancer.gov/statfacts/html/pancreas.html. Published 2019. Accessed January 24, 2020.

8.   Wang RF, Loc'h C, Mazière B. Determination of unchanged [18F]dopamine in human and nonhuman primate plasma during positron emission tomography studies: A new solid-phase extraction method comparable to radio-thin-layer chromatography analysis. *J Chromatogr B Biomed Appl*. 1997;693(2):265-270. doi:10.1016/S0378-4347(97)00086-8

9.   Ma Y, Kiesewetter DO, Lang L, et al. Determination of [18F]FCWAY, [18F]FP-TZTP, and their metabolites in plasma using rapid and efficient liquid-liquid and solid phase extractions. *Nucl Med Biol*. 2003;30(3):233-240. doi:10.1016/S0969-8051(02)00452-3

10.   Snyder F, Cress E. Application of thin-layer chromatographic zonal 14C-Profile scans to the analysis of urinary constituents derived from lipds. *Clin Chem*. 1968;14(6):529-534.

11.   Ai4r. BeaQuant. http://www.ai4r.com/real-time-autoradiography/product/. Published 2017. Accessed January 31, 2020.

12.   Krohn KA, Link JM, Mason RP. Molecular imaging of hypoxia. *J Nucl Med*. 2008;49:129S-148S. doi:10.2967/jnumed.110.075663

13.   Cao D, Qin S, Mu Y, Zhong M. The role of MRP1 in the multidrug resistance of colorectal cancer. *Oncol Lett*. 2017;13(4):2471-2476. doi:10.3892/ol.2017.5741

14.   Norris MD, Madafiglio J, Gilbert J, Marshall GM, Haber M. Reversal of multidrug resistance-associated protein-mediated drug resistance in cultured human neuroblastoma cells by the quinolone antibiotic difloxacin. *Med Pediatr Oncol*. 2001;3(1):177-180. doi:10.1002/1096-911X(20010101)36:1<177::AID-MPO1042>3.0.CO;2-Q

15.   Burkhart CA, Watt F, Murray J, et al. Small-molecule multidrug resistance-associated protein 1 inhibitor reversan increases the therapeutic index of chemotherapyin mouse models of neuroblastoma. *Cancer Res*. 2009;69(16):6573-6580. doi:10.1158/0008-5472.CAN-09-1075

16.   Hoffmann K, Bekeredjian R, Schmidt J, Büchler MW, Märten A. Effects of the high-affinity peptide reversin 121 on multidrug resistance proteins in experimental pancreatic cancer.

Chapter 6

6   CURRICULUM VITEA

Fiona Li, M.Sc.
The University of Western Ontario
Department of Medical Biophysics
London, Ontario, Canada

EDUCATIONS

Ph.D. Medical Biophysics   September 2014 – June 2020
The University of Western Ontario| London, Ontario
Department of Medical Biophysics

Dissertation: Kinetic Analysis of Dynamic PET with Targeted Probes for Molecular, Functional
and Physiological Characterization of Diseases
Supervisors: Dr. Ting-Yim Lee and Dr. James Koropatnick

M.Sc. Clinical Medical Biophysics   September 2016 – August 2018
The University of Western Ontario | London, Ontario
Department of Medical Biophysics

B.Sc. Medical Physics (Co-operative Program)   September 2009 – April 2014
Ryerson University | Toronto, Ontario
Department of Physics

WORK EXPERIENCES

Student Mentorships   May 2017 – August 2017
The University of Western Ontario   May 2018 – August 2018
Undergraduate Research Assistants

Teaching Assistant   January 2017 – April 2017
Department of Medical Biophysics
The University of Western Ontario
Course title: Practical Medical Imaging/ MEDBIO 9520B

Quality Assurance Apprenticeship   May 2017 – August 2017
London Regional Cancer Program | London | Canada

Undergraduate Research Assistant

NSERC Undergraduate Research Assistant   May 2014 – August 2014
Ryerson University | Toronto |Canada

TRIUMF Proton Eye Therapy Facility | Vancouver | Canada   September 2012 – December 2012

Harold E. John Studentship
Southlake Regional Cancer Centre | Newmarket | Canada

July 2012 – August 2012

Health Physicists
Ontario Power Generation | Bowmanville | Canada

February 2013 – August 2013

SCHOLARSHIPS

Ontario Graduate Scholarship
Department of Medical Biophysics
The University of Western Ontario | London |Canada
Value: $ 15,000 / year

2018 - 2019

Cancer Research and Technology Transfer (CaRTT) Strategic Training
PhD Fellowship
The University of Western Ontario | London |Canada
Value: $18,000 / year

2017 – 2018

Ontario Graduate Scholarship
Department of Medical Biophysics
The University of Western Ontario | London | Canada

2015 – 2016

AWARDS

Certificate of Merit | Oral Presentation
London Imaging Discovery Day | London | Canada

2019

First Prize | Poster Presentation
Oncology Research and Education Day | London | Canada

2019

Honorable Mention | Oral Presentation
Imaging Network of Ontario | Toronto | Canada

2017

Molecular Imaging Travel Award | The University of Western Ontario
Value: $400

2015

Dean's Honor List | Ryerson University

2009 – 2014

Student Scholar | Ryerson university

2009 – 2014

PEER REVIEWED PUBLICATIONS

Alexandria Hauser-Kawaguchi, Mark Milne, Fiona Li, Ting-Yim Lee and Leonard G Luyt. *The development of a near infrared inulin optical probe for measuring glomerular filtration rate.* International Journal of Biological Macromolecules 123 (2019): 255-260.

MANUSCRIPTS (submitted)

1. **Fiona Li**, Justin Hicks, Lihai Yu, Lise Desjardin, Laura Morrison, Jennifer Hadway and Ting-Yim Lee. *Plasma radio-metabolite analysis of PET tracers for dynamic PET imaging: TLC and autoradiography.* European Journal of Nuclear Medicine and Molecular Imaging Research.
2. **Fiona Li**, Edward Taylor, Ivan Yeung, David Jaffray, Ur Metser, Neesha Dhani, David W. Hedley and Ting-Yim Lee. *Pharmacokinetic analysis of dynamic [^{18}F]FAZA PET imaging in pancreatic cancer patient.* European Journal of Nuclear Medicine and Molecular Medicine Research.
3. **Fiona Li**, Dae-Myoung Yang and Ting-Yim Lee. *Estimation of kinetic parameters for dynamic PET.* Physics in Medicine and Biology.
4. Dae-Myoung, **Fiona Li**, Glenn Bauman, Joseph Chin, Stephen Pautler, Madeleine Moussa, Irina Rachinsky, John Valliant and Ting-Yim Lee. *Kinetic analysis of dominant intraprostatic lesion of prostate cancer using quantitative dynamic [18F]DCFPyL: Comparison to [18F]fluorocholine-PET.* European Journal of Nuclear Medicine and Molecular Imaging Research.
5. Clay Lindsay, Nick Zacchia, Ewart Blackmore, Cheryl Duzenli, Eric Himbeault, **Fiona Li**, Andrew Jirasek, Crystal Penner, Michael Trinczek, Cornelia Hoehr. *Monte Carlo Simulation of Primary and Secondary Dose for the TRIUMF Proton Therapy Facility.* Radiation Measurements.

BOOK CHAPTER

Ting-Yim Lee, Dae-Myoung Yang, **Fiona Li** and Raanan Marants. (2020) *CT Perfusion techniques and applications in stroke and cancer.* Computed Tomography. Springer, Cham: pp 347-365

CONFERENCE PUBLICATIONS

1. **Fiona Li,** Sung J. Cho, Lihai Yu, Robert H.E. Hudson, Leonard G. Luyt, Michael S. Kovacs, James Koropatnick, Ting-Yim Lee. *Evaluation of 6-([18F] fluoroacetamido)-1-hexanoic-anilide (18F-FAHA) as imaging probe in tumor xenograft mice model.* Proc. SPIE 9788, Medical Imaging 2016: Biomedical Applications in Molecular, Structural, and Functional Imaging, 978814 (March 29, 2016); doi:10.1117/12.2216905.
2. Cornelia Hoehr, Michael Trinczek, **Fiona Li**, Eric Himbeault, Nick Zacchia, Paul Schaffer, Ewart Blackmore. *FLUKA simulation of the TRIUMF Proton Therapy Facility.* International Journal of Particle Therapy, Summer 2014. 1(1):220 (Abstract)
3. Cornelia Hoehr, Michael Trinczek, **Fiona Li**, Katherine Dinelle, Stephan Blinder, Ewart Blackmore, William Kwa, Richard Lee, Vesna Sossi, Thomas J. Ruth, Paul Schaffer, Katherine Paton. *PET scanning of ocular melanoma after proton therapy.* IEEE Nuclear Science Symposium and Medical Imaging Conference (NSS/MIC), 2012; M22-3: 3850-3853

INVITED TALKS

1. *Kinetic analysis of dynamic PET study using the Johnson-Wilson-Lee Model for the visualization of dominant intraprostatic tumor with ^{18}F-DCFPyL and ^{18}F-FCH.* 7th Annual Alberta Imaging Symposium. Edmonton, Alberta, Canada. May 8, 2017
2. *Evaluation of histone deacetylation activity in tumors.* Medical Physics Retreat, London Ontario, Canada: November 8, 2016

3. *Targeting epigenetics in tumour through imaging*. Leaders in Innovation Dinner, Robarts Research Institute, London, Ontario, November 18, 2015

ORAL PRESENTATIONS

1. **F. Li**, E. Taylor, I. Yeung, D. Jaffray, D.W. Hedley, and T.-Y. Lee. *Study of hypoxia in pancreatic cancer patients using dynamic ^{18}F-FAZA PET.* Radiological Society of North America, Chicago, IL, USA: December 1-6, 2019
2. I. Yeung, B. Driscoll, C. Uribe, M. Budzevich, M. Grkovski, C. R. Schmidtlein, T.-Y. Lee, **F. Li**, S. Nehmeh, J. Sunderland, and D.A. Jaffray. *A multi-site phantom study to quantify variation of hypoxia fraction measurement with PET.* Radiological Society of North America, Chicago, IL, USA: December 1-6, 2019
3. **F. Li**, E. Taylor, I. Yeung, D. Jaffray, D.W. Hedley, and T.-Y. Lee. *Kinetic analysis of ^{18}F-FAZA uptake versus time in pancreatic tumors.* American Association of Physicists in Medicine Annual Meeting, San Antonio, TX, USA: July 14-18, 2019
4. **F. Li**, E. Taylor, I. Yeung, D. Jaffray, D.W. Hedley, and T.-Y. Lee. *PET imaging of hypoxia in pancreatic tumors using 18F-FAZA.* London Imaging Discover, London, Ontario: June 12 2019
5. **F. Li**, E. Taylor, I. Yeung, D. Jaffray, D.W. Hedley, and T.-Y. Lee. *Molecular imaging of hypoxia: Kinetic analysis of dynamic PET data from pancreatic cancer.* 17th Annual Imaging Network Ontario Symposium. London, ON: March 28-29, 2019
6. **F. Li**, A. Hauser – Kawaguchi, L.G. Luyt, C. McIntyre, J. Koropatnick, and T.-Y. Lee. *Preliminary study for personalization of renally excreted cancer drugs using pulse dye densitometry.* 15th Annual Imaging Network Ontario Symposium, London, ON: March 15-16, 2017
7. **F. Li,** S.J. Cho, L. Yu, R.H.E. Hudson, L.G. Luyt, M.S. Kovacs, C.L. Pin, J, Koropatnick and T,-Y, Lee. *Non-invasive measurement of histone deacetylase activity corrected for metabolites in epigenetic tumors.* London Health Research Day, London, Ontario: March 29, 2016
8. **F. Li,** S.J. Cho, L. Yu, R.H.E. Hudson, L.G. Luyt, M.S. Kovacs, C.L. Pin, J. Koropatnick and T.-Y. Lee. *Quantitative Evaluation of Epigenetic Modifications in Tumor with ^{18}F-FAHA PET Imaging.* SPIE Medical Imaging Conference, San Diego, California: February 27 – March 3, 2016
9. **F. Li**, S.J. Cho, L. Yu, R.H.E. Hudson, L.G. Luyt, M.S. Kovacs, J. Koropatnick and T.-Y. Lee. *Evaluation of [18F]-FAHA as Imaging Probe for HDAC Activity in Human Tumor Xenografts.* Oncology Education and Research Day, Western University: June 26th, 2015. London, Ontario
10. **F. Li** and T.-Y. Lee. *Improving quantitative functional imaging with dynamic contrast enhanced studies using a linearized Johnson-Wilson model approach.* IUPESM 2015 – World Congress on Medical Physics & Biomedical Engineering. Toronto, Canada: June 7th, 2015
11. C. Hoehr, M. Trinczek, **F. Li**, K. Dinelle, S. Blinder, E. Blackmore, W. Kwa, R. Lee, V. Sossi, T.R. Ruth, P. Schaffer, K. Paton. *PET scanning of ocular melanoma after proton therapy.* IEEE Nuclear Science Symposium and Medical Imaging Conference (NSS/MIC), 2012-10-27

POSTER PRESENTATIONS

1. Q. Qi, M.S. Fox, **F. Li**, T.J. Scholl, R. Bartha, L. Hoffman, T.-Y. Lee, and J.D. Thiessen. *Comparison of tumor pH environment and glycolysis measurements in a C6 rat model of glioma.* World Molecular Imaging Congress, Montreal, QC: September 4-7, 2019

2. **F. Li**, E. Taylor, I. Yeung, D. Jaffray, D.W. Hedley, and T.-Y. Lee. *Imaging of hypoxia in pancreatic cancer patients.* Oncology Research and Education Day, London, Ontario: June 14, 2019

3. **F. Li**, A. Hauser-Kawaguchi, C. McIntyre, M. Diop, K. St. Lawrence, L.G. Luyt, J. Koropatnick, and T.-Y. Lee. *Personalization of cancer drugs cleared by kidneys using optical transcutaneous pulse dye densitometry.* 2018 CARO-COMP-CAMRT Joint Scientific Meeting, Montreal, QC: September 12-15, 2018

4. D.-M. Yang, **F. Li**, G. Bauman, J. Valliant, W. He, and T.-Y. Lee. *Visualization of dominant intraprostatic nodules using quantitative dynamic PSMA and choline- PET/CT.* 13th London Imaging Discovery Day 2018, London, ON: June 14, 2018

5. **F. Li**, and T.-Y. Lee. *Estimation of molecular kinetic parameters from dynamic PET images.* 13th Annual London Imaging Discovery Day, London, ON: June 14, 2018

6. **F. Li**, D. Yang, and T.-Y. Lee. *Blood flow effect on estimated binding and disassociation rate constant of targeted probes from dynamic PET imaging studies.* 15th Annual Oncology Research and Education Day, London, ON: June 8, 2018

7. **F. Li**, A. Hauser-Kawaguchi, C. McIntyre, M. Diop, K. St. Lawrence, L.G. Luyt, J. Koropatnick, and T-Y. Lee. *Measurements of kidney function for optimizing dosage of cancer drugs cleared by kidneys.* Robarts Research Retreat, London, ON: June 1, 2018

8. **F. Li**, A. Hauser-Kawaguchi, C. McIntyre, M. Diop, K. St. Lawrence, L.G. Luyt, J. Koropatnick, and T.-Y. Lee. *Personalization of cancer drugs dosage based on kidney function: A preliminary study.* London Health Research Day, London, ON: May 10, 2018

9. **F. Li**, D. Yang, and T.-Y. Lee. *Effect of blood flow on molecular and physiological parameters from dynamic PET prostate cancer.* 2nd Cellular and Molecular Imaging Symposium, London, ON: May 1, 2018

10. **F. Li**, A. Hauser-Kawaguchi, C. McIntyre, M. Diop, K. St. Lawrence, L.G. Luyt, J. Koropatnick, and T.-Y. Lee. *Non-invasive quantification of glomerular filtration rate for personalization of renal cleared cancer drugs.* 16th Annual Imaging Network Ontario Symposium, Toronto, ON: March 28-29, 2018

11. D.-M. Yang, **F. Li**, G. Bauman, J. Valliant, W. He, and T.-Y. Lee. *Quantitative ^{18}F-labelled PSMA and ^{18}F-choline PET/CT: Visualizing dominant intraprostatic modules.* CIHR Team Grant & OICR Smarter Imaging Program (SIP) – Prostate Workshop, London, ON: November 17, 2017

12. **F. Li**, S.J. Cho, L. Yu, R.H.E. Hudson, L.G. Luyt, M.S. Kovacs, J. Koropatnick, and T.-Y. Lee. *Quantitative in-vivo PET imaging of epigenetic tumors using ^{18}F-FAHA with metabolite correction in mice model.* World Molecular Imaging Congress 2017, Philadelphia, PA, USA: September 13-16, 2017

13. D.-M. Yang, **F. Li**, G. Bauman, J. Valliant, W. He and T.-Y. Lee. *Dynamic ^{18}F-DCFPyL PET study of prostate cancer: comparison with ^{18}F-FCH.* World Molecular Imaging Congress 2017, Philadelphia, PA, USA: September 13-16, 2017

14. **F. Li**, A. Hauser-Kawaguchi, C. McIntyre, M. Diop, K. St. Lawrence, L.G. Luyt, J. Koropatnick, and T.-Y. Lee. *Personalized dosing of renally excreted drugs using non-invasive pulse dye densitometry.* Robarts Research Retreat, London, ON: June 20, 2017

15. D.-M. Yang, **F. Li**, G. Bauman, J. Valliant, W. He and T.-Y. Lee. *Comparison of ^{18}F-DCFPyL and ^{18}F-FCH for dynamic PET imaging in patients with prostate cancer.* London Health Research Day, London, ON: March 28, 2017

16. **F. Li**, A. Hauser-Kawaguchi, C. McIntyre, M. Diop, K. St. Lawrence, L.G. Luyt, J. Koropatnick, and T.-Y. Lee. *Personalization of renally excreted cancer drugs by evaluating kidney function.* London Health Research Day, London, ON: March 28, 2017

17. D.-M. Yang, **F. Li**, G. Bauman, J. Valliant, W. He and T.-Y. Lee. *Quantitative comparison of ^{18}F-DCFPyL dynamic PET imaging of prostate cancer with ^{18}F-FCH.* Ontario Institute for Cancer Research (OICR) Scientific Meeting, Toronto, ON: March 23-24, 2017

18. **F. Li**, A. Hauser – Kawaguchi, L.G. Luyt, C. McIntyre, J. Koropatnick, and T.-Y. Lee. *Estimation of GFR for personalization of renally excreted cancer drugs.* Ontario Institute for Cancer Research (OICR) Scientific Meeting, Toronto, ON: March 23-24, 2017

19. D.-M. Yang, **F. Li**, G. Bauman, J. Valliant, W. He and T.-Y. Lee. *Comparison of dynamic ^{18}F-DCFPyL and ^{18}F-FCH positron emission tomography imaging in patients with prostate cancer.* 15th Annual Imaging Network Ontario Symposium, London, ON: March 15-16, 2017

20. D.-M Yang, **F. Li**, G. Bauman, J. Valliant, W. He and T.-Y. Lee. *Preliminary experience with dynamic ^{18}F-DCFPyL PET study of prostate cancer: comparison with ^{18}F-FCH.* CIHR Team Grant & OICR Smarter Imaging Program (SIP)- Prostate Workshop, London, ON: November 25, 2016

21. **F. Li**, S.J. Cho, L. Yu, R.H.E. Hudson, L.G. Luyt, M.S. Kovacs, C.L. Pin, J. Koropatnick, and T.-Y. Lee. *Quantification of HDAC activity corrected for metabolites in epigenetic tumors – preliminary study.* 11th Annual London Imaging Discovery Day, London, ON: June 21, 2016

22. **F. Li,** S.J. Cho, L. Yu, R.H.E. Hudson, L.G. Luyt, M.S. Kovacs, C.L. Pin, J. Koropatnick and T.-Y. Lee. *HDAC quantification with metabolite correction in epigenetic tumors*. Oncology Education and Research Day Department of Oncology, University of Western Ontario: June 17th, 2016. London, Ontario.

23. **F. Li**, S.J. Cho, L. Yu, R.H.E. Hudson, L.G. Luyt, M.S. Kovacs, J. Koropatnick, and T.-Y. Lee. *Tracer kinetics of histone deacetylase and its metabolites in epigenetic tumors.* Imaging Network of Ontario, Toronto, ON: March 30-31, 2016

24. **F. Li,** S.J. Cho, L. Yu, A. Blais, E. Stewart, J. Hadway, L. Morrison, R.H.E. Hudson, L.G. Luyt, M.S. Kovacs, C.L. Pin, J. Koropatnick and T.-Y. Lee. *Imaging Epigenetic Changes in Cancer – Preliminary Experience with F-18 FAHA for Tumor Histone Deacetylase Activity.* Radiological Society of North America 101st Scientific Assembly and Annual Meeting, Chicago, Illinois: November 29 – December 4, 2015

25. **F. Li**, and T.-Y. Lee. *Improving the compartment model parameter estimation using linearized approach.* London Health Research Day, London, ON: April 1st, 2015

26. **F. Li**, and T.-Y. Lee. *Linearized Johnson-Wilson approach for modelling dynamic contrast enhanced studies.* Imaging Network of Ontario 13th Imaging Symposium, London, ON: March 30-31, 2015

27. C. Hoehr, M. Trinczek, **F. Li**, E. Himbeault, N. Zacchia, P. Schaffer, E. Blackmore. *FLUKA simulation of the TRIUMF proton therapy facility.* Proceedings of the 52nd Annual Meeting for the Particle Therapy Cooperative Group (PTCOG)